# Electronic and Spin Correlations in Asymmetric Quantum Point Contacts

by

Hao Zhang

Department of Physics
Duke University

Date: _____

Approved:

_____
Albert M. Chang, Supervisor

_____
Harold Baranger

_____
Gleb Finkelstein

_____
Henry Greenside

_____
Stephen W. Teitsworth

Dissertation submitted in partial fulfillment of the requirements for the degree of
Doctor of Philosophy in the Department of Physics
in the Graduate School of Duke University
2014

# Abstract

## Electronic and Spin Correlations in Asymmetric Quantum Point Contacts

by

Hao Zhang

Department of Physics
Duke University

Date: _____

Approved:

_____
Albert M. Chang, Supervisor

_____
Harold Baranger

_____
Gleb Finkelstein

_____
Henry Greenside

_____
Stephen W. Teitsworth

An abstract of a dissertation submitted in partial fulfillment of the requirements for the degree of Doctor of Philosophy in the Department of Physics in the Graduate School of Duke University
2014

Copyright © 2014 by Hao Zhang
All rights reserved except the rights granted by the
Creative Commons Attribution-Noncommercial Licence

# Abstract

A quantum point contact (QPC) is a quasi-one dimensional electron system, for which the conductance is quantized in unit of $2e^2/h$. This conductance quantization can be explained in a simple single particle picture, where the electron density of states cancels the electron velocity to a constant. However, two significant features in QPCs were discovered in the past two decades, which have drawn much attention: the 0.7 effect in the linear conductance and zero-bias-anomaly (ZBA) in the differential conductance. Neither of them can be explained by single particle pictures.

In this thesis, I will present several electron correlation effects discovered in asymmetric QPCs, as shown below:

The linear conductance of our asymmetric QPCs shows conductance resonances. The number of these resonances increases as the QPC channel length increases. The quantized conductance plateau is also modulated by tuning the gate voltage of the QPCs. These two features, observed in the linear conductance, are ascribed to the formation of quasi-bound states in the QPCs, which is further ascribed to the electron-correlation-induced barriers.

The differential conductance for long channel QPCs shows the zero-bias-anomaly for every other linear conductance resonance valley, suggesting a near even-odd behavior. This even-odd law can be interpreted within the electron-correlation-induced barrier picture, where the quasi-localized non-zero spin in the quasi-bound state (Kondo-like) couples to the Fermi sea in the lead. For a specific case, triple-peak

structure is observed in the differential conductance curves, while the electron filling number is still even, suggesting a spin triplet formation at zero magnetic field.

Small differential conductance oscillations as a function of bias voltage were discovered and systematically studied in an asymmetric QPC sample. These oscillations are significantly suppressed in a low in-plane magnetic field, which is completely unexpected. The oscillations are washed out when the temperature is increased to 0.8K. Numerical simulation, based on the thermal smearing of the Fermi distribution, was performed to simulate the oscillation behavior at high temperatures, using the low temperature data as an input. This simulation agrees with the oscillations off zero-bias region, but does not agree with the temperature evolution of the structure near zero-bias. Based on the above oscillation characteristics, all simple single particle pictures were carefully considered, and then ruled out. After exhausting all these pictures, we think these small oscillations are related to novel electronic and spin correlations.

To my parents Zhenghai Zhang, Kuiye Zhang, and my wife Yuxin Wang

# Contents

**Abstract** **iv**

**List of Figures** **ix**

**Acknowledgements** **xii**

**1 Introduction to Quantum Point Contacts** **1**

1.1 GaAs/AlGaAs Two Dimensional Electron Gas(2DEG) . . . . . 3

1.2 Quantum Point Contacts: a Single-Particle Picture . . . . . 6

1.3 Quantum Point Contacts: the Many-Body Physics . . . . . 10

1.3.1 '0.7' Effect in QPCs . . . . . 10

1.3.2 the Zero-bias-anomaly in QPCs . . . . . 12

1.3.3 '0.7' Effect and ZBA: What is the physics behind them? . . . 15

**2 Sample Fabrication and Experimental Measurement Set-up** **17**

2.1 Sample Fabrication: the State of Art . . . . . 17

2.2 Measurement Technique . . . . . 21

**3 Electron Correlation Effects in Asymmetric QPCs: Correlation-induced-barriers** **25**

3.1 Wigner Crystallization in QPCs . . . . . 26

3.2 Linear Conductance of Symmetric QPCs versus Asymmetric QPCs . 28

3.2.1 High Temperature Data . . . . . 30

3.2.2 Low Temperature Data : 300mK in He3 Fridge . . . . . 35

3.2.3 Discussion: the Intrinsic Nature of the Resonances and the Modulation of Plateaus for Asymmetric QPCs . . . . . 41

3.2.4 Discussion: Electron Correlation Induced Barriers and the Formation of Quasi-bound States in Asymmetric QPCs . . . . . 44

3.3 the Differential Conductance of Asymmetric QPCs . . . . . 53

3.3.1 Even-Odd Effect of the Zero Bias Anomaly . . . . . 56

3.3.2 Even-Odd Effect Discussion: Kondo-like Physics . . . . . 58

3.3.3 the Triple-peak Structure: Possible Spin-1 Kondo Effects . . . 63

**4 Electron Correlation Effects in Asymmetric QPCs: Novel Differential Conductance Oscillations 69**

4.1 Linear Conductance . . . . . 70

4.2 Differential Conductance . . . . . 73

4.2.1 Temperature Dependence . . . . . 77

4.2.2 Magnetic Field Dependence: Low Field . . . . . 82

4.2.3 Magnetic Field Dependence: High Field . . . . . 85

4.2.4 Discussion: Are They Within the Single Particle Picture? . . . 87

**5 Conclusion 91**

**A Quantum Point Contacts on GaAs/AlGaAs Cleaved-Edge-Overgrowth Surface (001) 94**

A.1 Introduction . . . . . 94

A.2 Device Fabrication on the Cleaved-edge Surface . . . . . 96

A.2.1 Nano-device Fabrication Steps on the CEO Surface . . . . . 97

A.3 Observation of the Quantized Conductance Plateau in CEO . . . . . 102

**Bibliography 104**

**Biography 113**

# List of Figures


1.1 Nano-structure Fabrication in GaAs/AlGaAs 2DEG . . . . . 4

1.2 Quantized Conductance of a Typical QPC . . . . . 6

1.3 Energy Level and Dispersion Relation in QPC . . . . . 8

1.4 0.7 effect . . . . . 11

1.5 Zero Bias Anomaly in QPCs . . . . . 13

2.1 Sample Fabrication Steps . . . . . 18

2.2 Measurement Set-up . . . . . 22

3.1 Wigner Crystallization and Zigzag Phase Transition . . . . . 27

3.2 Geometry of Symmetric QPC versus Asymmetric QPC . . . . . 29

3.3 Linear Conductance of a Symmetric QPC at 4.2K . . . . . 30

3.4 Linear Conductance of an Asymmetric QPC at 4.2K . . . . . 32

3.5 Linear Conductance of a Symmetric QPC at 3K . . . . . 34

3.6 Linear Conductance of an Asymmetric QPC at 3K . . . . . 35

3.7 Linear Conductance of a Symmetric QPC (100nm channel length) at 300mK . . . . . 36

3.8 Linear Conductance of a Symmetric QPC (500nm channel length) at 300mK . . . . . 36

3.9 Linear Conductance of an Asymmetric QPC (100nm channel length) at 300mK . . . . . 37

3.10 Linear Conductance of an Asymmetric QPC (300nm channel length) at 300mK . . . . . 38

3.11 Linear Conductance of an Asymmetric QPC (500nm channel length) at 300mK . . . . . 38

3.12 Linear Conductance of an Asymmetric QPC (1000nm channel length) at 300mK . . . . . 39

3.13 Statistics of the number of resonances for asymmetric QPCs . . . . . 41

3.14 Transmission Probability for a 1D potential barrier . . . . . 46

3.15 Theoretical calculations for the localized states in QPCs . . . . . 49

3.16 Differential Conductance for a 300nm Channel Length Asymmetric QPC . . . . . 54

3.17 Differential Conductance for an Asymmetric QPC: Even and Odd Effect for ZBA . . . . . 57

3.18 Kondo Effect in Quantum Dots . . . . . 59

3.19 Differential Conductance for an Asymmetric QPC: Triple-peak Structure 63

3.20 Differential Conductance for an Asymmetric QPC: another set of data for the even-odd behavior and triple peak structure . . . . . 66

4.1 Linear conductance for the Asymmetric QPC . . . . . 70

4.2 Magnetic Field Dependence of Linear Conductance for the Asymmetric QPC . . . . . 72

4.3 Differential Conductance for the Asymmetric QPC in Dilution Fridge 74

4.4 Smooth and Background Subtraction of Differential Conductance . . 75

4.5 Differential Conductance for the Asymmetric QPC in He3 Fridge . . . 76

4.6 Differential Conductance for the Asymmetric QPC : High Temperature data . . . . . 77

4.7 Differential Conductance for the Asymmetric QPC : Temperature Dependence and Simulation . . . . . 78

4.8 Differential Conductance for the Asymmetric QPC : Statistics for the Oscillation Size . . . . . 81

4.9 Differential Conductance for the Asymmetric QPC : Low Magnetic Field Dependence . . . . . 82

4.10 Differential Conductance for the Asymmetric QPC : Low Magnetic Field Dependence (statistics) . . . . . 84

4.11 Differential Conductance for the Asymmetric QPC : High Magnetic Field Dependence . . . . . 85

4.12 Differential Conductance for the Asymmetric QPC : Magnetic Field Dependence at High Temperature . . . . . 86

A.1 Schematic of CEO Crystal and QPC Device on CEO Surface . . . . . 96

A.2 Optical Image of a Quantum Nano-structure Device on the CEO Surface . . . . . 101

A.3 Quantized Conductance of a QPC on CEO Surface . . . . . 102

# Acknowledgements

For most I would like to thank my adviser Professor Albert Chang for his extraordinary guidance. Before joining his group, I came and got trained from the traditional Chinese education system. I was good at doing math, reading textbooks and taking exams. I thought this was doing science: following instructions and working hard. I didn't realize what real research was until I started to work with Albert. Over the past 4 years, I had a lot of discussions with him not only about our research (e.g. physics, technique, data...), but also about how to do research. He helps me to think and work scientifically, to approach problems based on facts and statistics, not based on my own illusion. He didn't guide me step by step in great details. He always gives me a lot of freedom to explore by myself first. When I got stuck and frustrated, he was always there to talk to me. This way of training not only helps me to solve problems, but also deepens my understanding of real science and research. This is truly a unique experience which I believe I will benefit a lot in my upcoming academia career. By working with Albert, not only have I learned physics knowledge and experimental techniques, but also the methodology of doing science, for which I believe is even more important.

I would also like to thank my committee members Professor Gleb Finkelstein, Professor Harold Baranger, Professor Stephen Teitsworth and Professor Henry Greenside for taking time to oversee this work. They really gave me a lot of good advice. I would like to thank Gleb and Harold for teaching us Statistical Mechanics and Ad-

vanced Solid State Physics. I would like to thank Dr. Dong Liu, Dr. Huaixiu Zheng and Dr. Phillip Wu for useful discussions and guidance of my career.

Finally I would like to thank my family members: my parents Zhenghai Zhang and Kuiye Zhang, my wife Yuxin Wang and my brother Chao Zhang. This would not have been possible without their unlimited support and love.

# 1

# Introduction to Quantum Point Contacts

The development of solid state electronics has caused a modern technological revolution with which probably only the industrial revolution can compare. The fast development in this semiconductor industry allows people to be able to design and fabricate sub-20nm sized transistors nowadays. To understand the electron transport property in semiconductors of this size, classical physics is not enough, and quantum mechanics needs to be included. Semiconductor nano-structures provide an ideal way to study how electrons behave quantum mechanically under such conditions. Comparing with silicon which is the dominant semiconductor material in industry, GaAs/AlGaAs two dimensional electron gas (2DEG), in a sense, is a better system to work with, for studying the fundamental properties of electron nano-structure for the following reasons. First, the electron mean free path (mobility) is much longer (higher) in the 2DEG of GaAs/AlGaAs crystal than in the 2DEG of silicon-based Metal-Oxide-Semiconductor Field Effect Transistor (MOSFET). This advantage is due to a technique developed for GaAs/AlGaAs, called the modulation doping, which spatially separates donors away from the 2DEG region. Thus the scattering rate due to the ionized donors is exponentially suppressed in the GaAs 2DEG, resulting in a

longer mean free path than the silicon case. Second, by controlling the donor number during the layer by layer growth of GaAs/AlGaAs crystal (the molecular beam epitaxy growth(MBE)), the electron density in the 2DEG can be modulated. Low electron densities($\sim 10^{11}/cm^2$) can be achieved. Such low electron density gives a low Fermi energy and long Fermi wavelength ($\sim 40nm$) which can be comparable to the nano-structure size. Thus the wave property of electrons will be more prominent. Besides this quantum mechanical effect of electrons, low electron density tend to give a relatively strong electron-electron Coulomb interaction. This is due to the fact that electron kinetic energy ($\propto \frac{1}{r_s^2}$) decreases faster than the Coulomb energy ($\propto \frac{1}{r_s}$), where $r_s$ is the effective radius of electrons. This strong electron correlation, incorporated with the quantum mechanics nature of electrons, has shown various interesting many-body quantum effects, which also bring new concepts and physics, e.g. Kondo effect[1], Fractional Quantum Hall effect[2] and the possible quantum Wigner crystallization. This is why the semiconductor nano-structure (especially GaAs/AlGaAs based) is of research interest for fundamental physics.

The nano-structures, created in GaAs/AlGaAs 2DEG, are usually fabricated by patterning sub-micron metal gates on the top of a crystal, using the state of art technique similar with the technique used in silicon industry. These fabricated nano-structures are usually studied at low temperature (e.g. below 100mK), where the quantum effects, like phase coherence, are strong. The physics of nano-structures at low temperature can be studied by performing electron transport measurement. For example, the conductance (the inverse of resistance) of these nano-structure will change by tuning the physical parameters, like magnetic field, electric field (bias voltage) and electron density (which is further tuned by the gate voltage). Based on how the electron transport is affected by these physical parameters, we can extract (or map) out the rich physics occurring in the nano-structures, such as Coulomb

effects (like Coulomb blockade), quantum interference, Kondo effect and possible new state of matter (like quantum Wigner crystal).

In this thesis, we will focus on the electron transport study of a simple nano-structure: quantum point contacts(QPCs), fabricated in GaAs/AlGaAs 2DEG. As will be shown later, even for such a simple nano-structure, very exciting quantum and many-body electron behaviors can be revealed. The motivation of this research is to investigate a new strong electron-correlated quantum state: the possible formation of the quantum Wigner crystal in QPCs, predicted by theory[3, 4, 5, 6, 7, 8, 9]. This new quantum state of matter is predicted to show interesting behavior, like ferromagnetic coupling in this quasi-one dimensional (with a finite length) electron system[6], while for a strict one dimensional electron system, it has been proved long time ago, by Lieb and Mattis, that the ground state must be anti-ferromagnetic, if the 1D electrons are subjected to a symmetric potential[10].

In the following sections of this chapter, I will provide an introduction to the GaAs/AlGaAs-based quantum point contacts (QPCs) system, and also the related physics.

## 1.1 GaAs/AlGaAs Two Dimensional Electron Gas(2DEG)

The two dimensional electron gas (2DEG), formed at the interface of GaAs/AlGaAs hetero-structure[11], is the starting point to fabricate nano-devices (including QPCs). Fig.1.1 shows the schematic of the GaAs/AlGaAs crystal structure, and how a typical nano-structure is fabricated. In panel (a), we depict the main part of the GaAs/AlGaAs crystal, with the top GaAs cap part and the bottom GaAs buffer substrate omitted. This hetero-structure is grown atomic layer by atomic layer using the technology called molecular beam epitaxy (MBE). The red dots (or the dashed line) represent Si donors, introduced during the growth. The donors will 'donate' electrons to the AlGaAs conduction band. Panel (b) shows the initial conduction

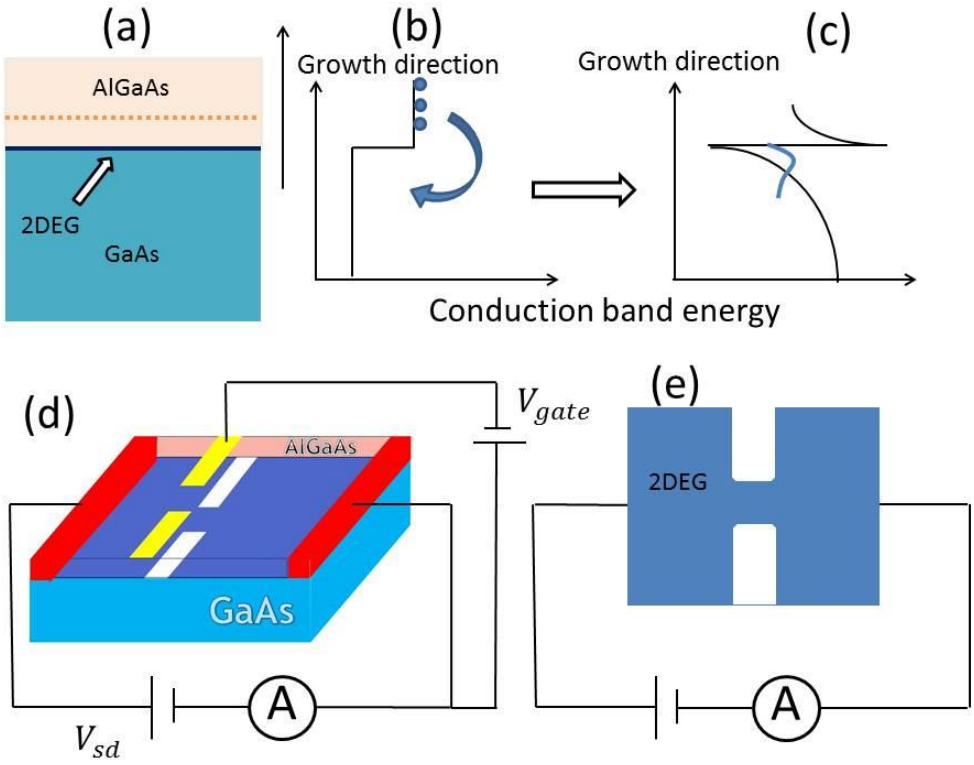


FIGURE 1.1: GaAs/AlGaAs 2DEG and the fabrication of nano-structures based on this 2DEG. (a)-(c): the forming of 2DEG in GaAs/AlGaAs hetero-structure. (d)-(e): a typical experimental set-up for electron transport measurement: patterning of gates (yellow), current contacts (red), and wire bonding

band structure, without distortion yet, of both the GaAs and AlGaAs crystalline regions along the direction of growth, with x axis representing the conduction band bottom energy. As can be seen, GaAs has a lower energy for the conductance band edge than AlGaAs. The electrons in the AlGaAs, donated from the Si donor, will flow to the GaAs conduction band to minimize the system's energy. The fixed ionized Si donors, after donating electrons, carry positive charges which will attract the electrons in GaAs and distort the band structure. Thus the modified band structure of this GaAs/AlGaAs hetero-structure will be a triangular-like shape as shown in panel (c). The electrons will be trapped and confined in this potential well at the interface in the growth direction. This confinement discretizes (quantizes) the energy

levels of the electrons along that direction. At low temperature, all the electrons will populate the lowest energy level. Thus the electron motion in the growth direction will be frozen. The electrons are only 'free' in the other two remaining spatial dimensions, which is the plane perpendicular to the growth direction. This electron system, with one reduced spatial dimension, is called a two dimensional electron gas (2DEG).

Fig.1.1(d) shows how a nano-structure can be obtained by patterning metal gates(yellow region in the figure) on the top of the GaAs crystal . Applying negative gate voltage on the two gates can repel and further deplete (exhaust) the electrons in the 2DEG underneath the gates. This depleted region, which has no electrons there, is represented as the white region in panel (d) and (e), while the blue region represents the electron gas. The conductance (1/Resistance) can be measured by hooking up a 'battery' to the two current contact leads(red bars in panel (d)), which are electrically connected with the 2DEG. These current contact leads are pure indium, which was initially put on the crystal surface, and was then heated up to diffuse down to make an electrical connection with the buried 2DEG. This annealing process is usually performed before the patterning of gates. Panel (e) shows an expanded version of the main circuit where the measured conductance is mainly the conductance of the narrow constriction, defined by the two white depleted bars. This is due to the fact that the left and right 2DEG parts have negligible resistance compared with the resistance of the constriction. The gate size is typically on the order of submicron, which is usually much shorter than the electron mean-free-path ($\sim 10\mu m$ or longer). Thus when electrons pass through this short constriction (point contact), almost no scattering will be experienced by those electrons. This type of transport is called ballistic transport. The point contact structure in panel (d) and (e) is called quantum point contact (QPC) which, as will be discussed below, shows quantized conductance. This conductance quantization is due to the ballistic transport in the

point contact channel.

## 1.2 Quantum Point Contacts: a Single-Particle Picture

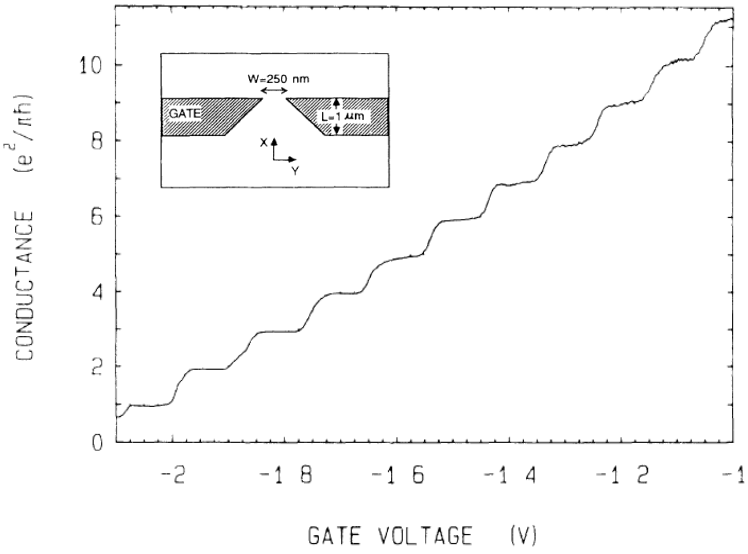


FIGURE 1.2: Quantized conductance of a typical QPC as a function of gate voltage. Figure taken from Ref[12]. Inset: the schematic gate geometry of this QPC.

The conductance measurement of this narrow short channel, or QPC, as a function of gate voltage, which controls the channel width, was first performed by van Wees *et al*[12] and Wharam *et al*[13]. Fig.1.2, taken from Ref[12], shows the conductance of a QPC as a function of gate voltage. The inset shows the schematic of the gate geometry, denoted by the shadow region. When the gate voltage becomes more negative, larger regions in the 2DEG are depleted (imagine that the white regions in Fig.1.1(e) get enlarged). Thus the constriction becomes narrower, resulting in a smaller conductance. Further decreasing the gate voltage to more negative will finally close the narrow constriction, where the 2DEG gets pinched off and the conductance becomes 0. This explains the decrease of conductance with decreasing the gate voltage. However, besides this decreasing relation which is expected, the conductance curve in Fig.1.2 shows step-like structure, where the step values are integer

multiples of the quantized conductance unit: $2e^2/h$. Here, e is electron charge, and h is the Plank constant. This conductance quantization has given rise to the name of quantum point contact (QPC) for this short narrow point contact channel.

The quantized conductance of QPCs was well understood, immediately after it was discovered, based on a single-particle picture where the electron-electron interaction is ignored. Fig.1.3 shows how this single-particle picture explains the conductance quantization. Panel (a) shows the 2DEG (blue) with the QPC gate depleted regions(white). The confinement in the y direction inside the QPC(as denoted in panel (a)) leads to a discrete momentum ($k_y$) and energy spectrum. For illustration purposes, we will assume a square well potential profile in the y-direction. But in general, it could be other forms for confinement. This confinement reduces the constriction region by one spatial dimension, resulting in a quasi-one dimensional electron system. The name quasi-1D, instead of 1D, rises from the finite QPC channel width, which results in several sub-1D levels. Each quantized $k_y$ or $E_y$ gives rise to a sub-band with a different sub-band bottom energy $E_y$. Panel (c) shows the dispersion relationship(energy vs $k_x$) for each sub-band: $E(k_x) = \frac{(\hbar k_x)^2}{2m} + E_i$, where $E_i$ is the ith sub-band bottom energy. Panel (c) shows three sub-bands, populated with electrons (blue dots) up to the quasi-chemical potential. Panel (b) and (d) represent the Fermi statistics of the left and right electron reservoir(leads) with different quasi-chemical potentials: $\mu_{Left}$ and $\mu_{Right}$. This difference is introduced by the bias voltage applied across the QPC. At $T = 0K$, the electrons in the left(right) reservoir will fill all the states with energy below $\mu_{Left}$ ($\mu_{Right}$). In panel (c) all the electrons with negative $k_x$ are propagating to the left. Thus they come from the right reservoir and have a quasi-chemical potential $\mu_{Right}$. The positive $k_x$ electrons, on the contrary, have quasi-chemical potential $\mu_{Left}$ as shown in panel (c).

Based on Fig.1.3, applying a small bias voltage ($V_{bias}$) across the QPC sets a

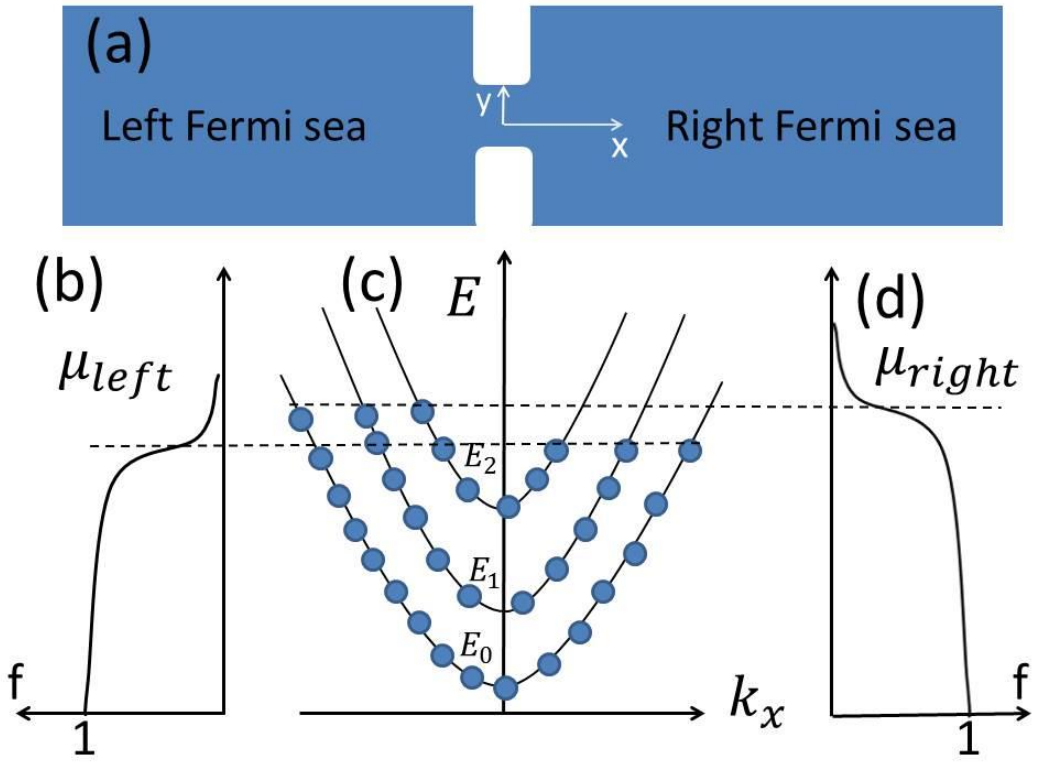


FIGURE 1.3: (a) 2DEG (blue) and the depleted region(white). (b) and (d): The Fermi function of electron for the left and right 2DEG reservoirs. (c): Dispersion relations (E vs k) for each sub-band formed inside the QPC channel.

difference between $\mu_{Left}$ and $\mu_{Right}$: $\mu_{Right} - \mu_{Left} = e \cdot V_{bias}$, leading to extra electrons populated on the negative $k_x$ side. These extra electrons will contribute a net current which is measured by the equipment. To calculate this current in terms of $V_{bias}$, consider a simple situation by assuming $T = 0K$, where the Fermi function is a sharp step curve. Then the current due to one populated sub-band is $I = e \cdot n(E) \cdot v(E) \cdot dE$. $n(E) = 2 \cdot n(k) \cdot \frac{dk}{dE} = 2 \cdot \frac{1}{2\pi} \cdot \frac{m}{\hbar^2 k} = \frac{2m}{h\hbar k}$ is the electron density of state, while $v(E) = \frac{\hbar k}{m}$ is the electron velocity and $dE = \mu_{Right} - \mu_{Left} = e \cdot V_{bias}$. Plugging in n(E), v(E), and dE into the current (I) formula, we obtain $I = V_{bias} \cdot 2e^2/h$. Thus the conductance for each populated sub-band is $G = I/V = 2e^2/h$ which is a constant and does not depend on where the chemical potential is, as long as the sub-band is populated. The coefficient 2 in the quantized conductance value is from the spin degeneracy. This

constant conductance for each populated sub-band comes from the fact that n(E) and v(E) are anti-proportional to each other. In Fig.1.3(c), there are three populated sub-bands, thus the conductance is $3 \cdot 2e^2/h$. Tuning the gate more negative will make the channel narrower, and $E_i$ higher. When the third sub-band gets squeezed out by the more negative gate voltage, only two sub-bands are populated, and the conductance drops by one step to $2 \cdot 2e^2/h$. In terms of the measured conductance versus gate voltage, it will show step-like structure. One needs to point out that in deriving the conductance of the individual sub-band, one hidden assumption is that the electrons entering the QPC channel can always pass through. This requires the electron transport to be ballistic, which means no scattering in the QPC channel. If the transport is not ballistic, e.g. diffusive, then the quantized plateau will be seriously degraded or disappear[14].

At finite low temperature, due to the thermal smearing of the Fermi function, the step-like curve will be smoothed around the edges. When the temperature is too high, e.g. $k_BT \sim \Delta E$, where $\Delta E = E_2 - E_1$ is the sub-band level spacing, the quantized plateau will be smoothed out. To better characterize and study the transport property, we have performed two types of conductance measurement. The first one is when $V_{bias}$ is small, by small we mean $e \cdot V_{bias}$ is smaller than the thermal broadening of the Fermi function ($\sim 3.5k_BT$). This restricts the $V_{bias}$ to be below $10\mu V$ at $T \sim 30mK$. The conductance measured under this small bias (a more appropriate way to describe this situation is to say that the bias is set to be zero, with a small excitation $V_{ac}$) is called the linear conductance. The conductance data in Fig.1.2 is the linear conductance as a function of gate voltage. The second type of measurement, called differential conductance is measured at a finite bias. A small change (or excitation) in the bias ($dV = V_{ac}$) will cause a small change in the current ($dI$). Then the differential conductance, $dI/dV$, can be measured at any finite bias ($V_{bias}$). The reason we want to measure $dI/dV$, instead of $I/V$, is because that

$dI/dV$ vs $V_{bias}$, in an approximate sense, can be thought of a mapping of electron density of states vs electron energy.

## 1.3 Quantum Point Contacts: the Many-Body Physics

The quantized plateau can be nicely explained by a simple single particle picture involving no electron correlations. However, over the past two decades, two major phenomena have been observed in QPCs and caught tremendous interest since they can not be explained by single-particle picture, thus requiring electron interaction to be included in the picture. Although numerous experimental and theoretical efforts have been spent on these two phenomena, the physics behind them is still under heavy debate[15]. Here I will briefly introduce these two important phenomena in quantum point contacts: the '0.7' structure in the linear conductance and the zero-bias-anomaly in the differential conductance.

### *1.3.1 '0.7' Effect in QPCs*

The first electron correlation effect discovered in QPCs is the so-called '0.7' effect, which is an inflection (or often a weak plateau), observed in the linear conductance curve near $0.7 \cdot 2e^2/h$[16]. Fig.1.4, taken from ref[16], shows the basic characteristics of this '0.7' structure. Panel (a) shows the linear conductance as a function of gate voltage of the QPC. As can be seen, besides the $2e^2/h$ plateau which is expected from the single particle picture, a bump near $0.7 \cdot 2e^2/h$ is observed. This '0.7' structure was actually observed in the very first paper on the quantized conductance of QPCs[12]. But only after 8 years later, people started to realize that this '0.7' effect is not an impurity effect and it was then studied systematically in ref[16]. One argument against the impurity origin for the '0.7' structure is that it can be reproduced by thermal cycling and can be observed in a number of different QPC devices, while structures in GaAs/AlGaAs caused by impurity usually can not be

reproduced by thermal cycling. The intrinsic nature of '0.7' effect is a big surprise and is not expected in the single particle picture.

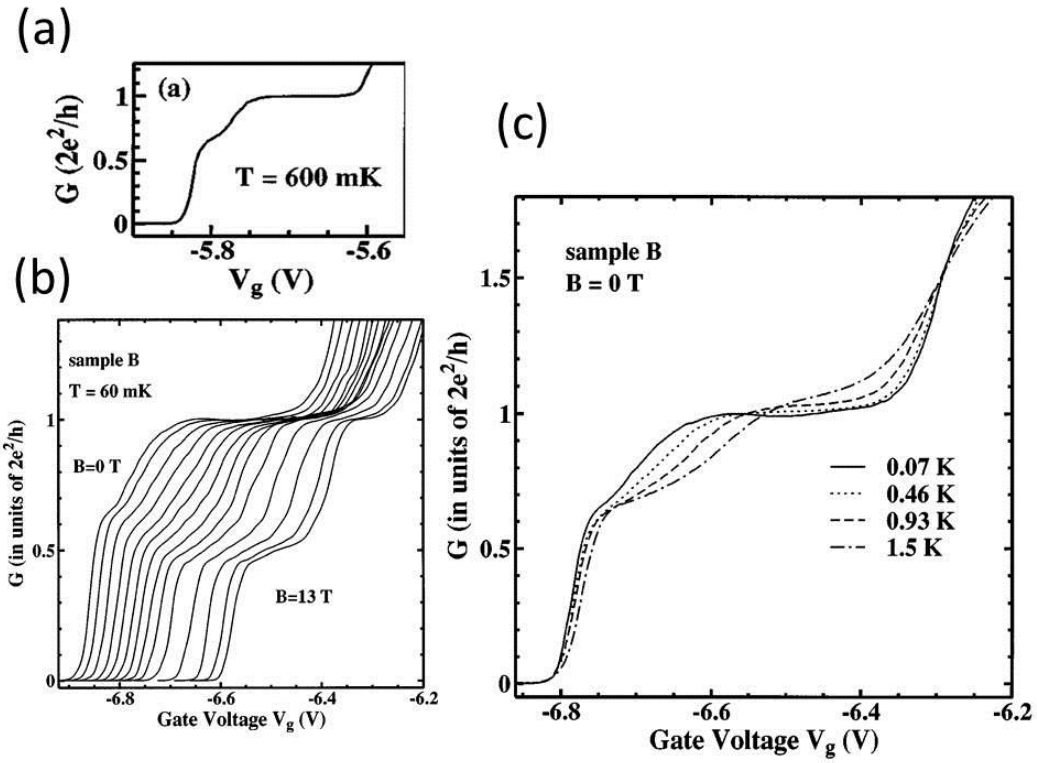


FIGURE 1.4: The '0.7' structure for linear conductance of QPC in the single channel limit. (a) the '0.7' structure. (b) In-plane magnetic field dependence of this '0.7' effect. (c) Temperature dependance of '0.7' effect. The figure is taken from ref[16].

Fig.1.4(b) shows the development of this '0.7' structure over an in-plane magnetic field. As can be seen, when the in-plane magnetic field increases from 0T to 13T, the '0.7' kink smoothly develops into the $0.5 \cdot 2e^2/h$ plateau. The in-plane magnetic field is used instead of out-of-plane field, is because that out-of-plane field will deflect the electron trajectory and introduce the quantum Hall effect[17] into this system when the cyclotron orbit is comparable with the QPC channel width. To avoid the rise of other effects other than spin, an in-plane magnetic field is used, which mainly 'talks to' the electron spin through Zeeman coupling. The number 2 in the quantized conductance $2e^2/h$ comes from spin degeneracy of the sub-bands. When

a high in-plane magnetic field is applied to the QPC, the sub-band spin-degeneracy will be lifted, and the sub-band splits into two spin-polarized sub-bands due to the Zeeman coupling: $E_Z = -\vec{\mu} \cdot \vec{B} = -\frac{g\mu_B B}{2}$. The conductance for each populated non-degenerate sub-band is $e^2/h$ instead of $2e^2/h$, which is observed in Fig.1.4(b). When increasing the in-plane magnetic field from 0T to 13T, the smooth evolution from '0.7' bump to '0.5' plateau suggest that this '0.7' structure is related to spin correlation.

Fig.1.4(c) shows the temperature dependence of this '0.7' structure which is quite different from the typical temperature dependence of a usual quantum phenomena. Usually for a quantum phenomena, such as quantum interference, decreasing the temperature increases the phase coherent length, and the phenomena will be strengthened. But for the '0.7' structure, as shown in panel (c), when the temperature is increased from 70mK to 1.5K, the '0.7' structure get strengthened. Actually the '0.7' structure reaches its maximum strength at $\sim 1.5K$ and gets less obvious at both lower temperature and higher temperature. At high temperature, the '0.7' structure is still observable while the quantized plateau may already be washed out. The '0.7' structure finally gets washed out at $\sim 10K$. This unusual temperature dependance suggest that '0.7' effect may not be the ground state property of the QPC, and a theory model based on the coupling between electron and phonon was proposed to interpret this[18].

### *1.3.2 the Zero-bias-anomaly in QPCs*

Besides the '0.7' effect in linear conductance, a zero-bias-peak(or anomaly) discovered in the differential conductance was another significant electron correlation effect in QPCs[19]. Fig.1.5, taken from ref[19], shows the characteristics for this Zero-bias-anomaly(ZBA). Panel (a) shows the gate geometry of the QPC (image from scanning electron microscope). The QPC lithographic channel length, defined by the gates, is

$\sim 500nm$. Panel (b) shows the linear conductance as a function of the gate voltage measured at different temperatures. As can be seen, at 4.1K, the quantized plateaus are gone due to the thermal smearing, but the '0.7' structure still survives.

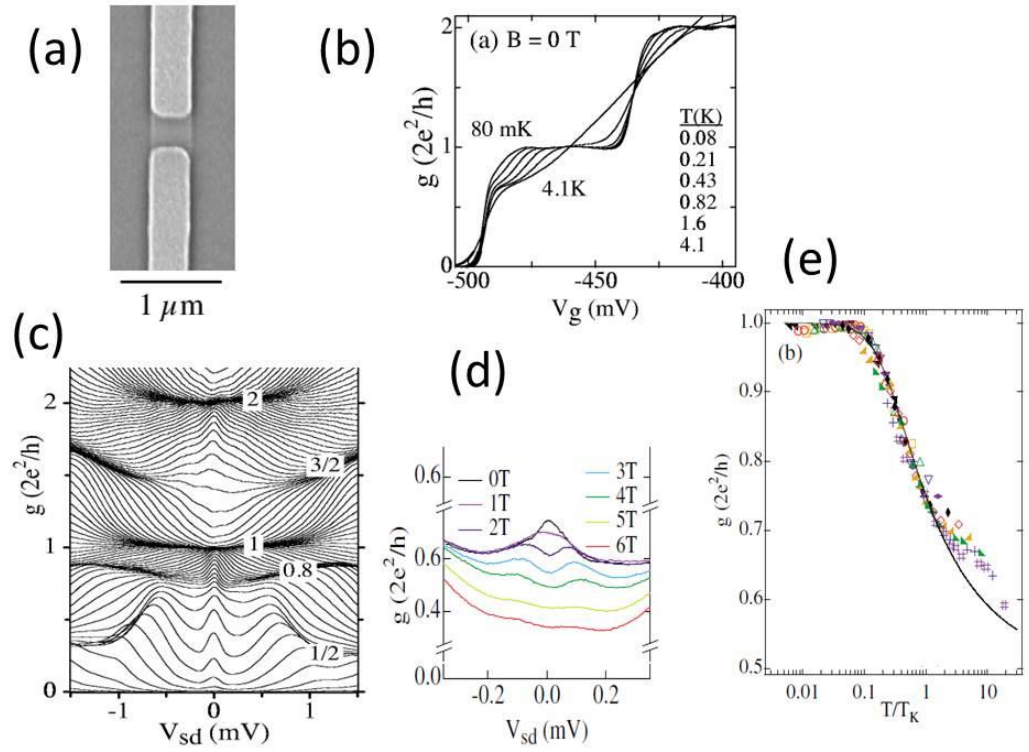


FIGURE 1.5: The '0.7' structure and zero-bias-anomaly. (a): SEM image of the QPC gate geometry, where the two bright bars are the two metal split gates. (b) Temperature dependence of the '0.7' structure in the linear conductance of the QPC. (c)Differential conductance as a function source-drain-biased voltage $V_{sd}$. Different curves represent different fixed gate voltages. (d) In-plane magnetic field dependence of one typical differential conductance curve. T=80mK in (c)(d). (e) The universal scaling of the conductance of the ZBA as a function of temperature. The figure is taken from ref[19].

Fig.1.5(c) shows the differential conductance as a function of source-drain-bias ($V_{sd}$). The gate voltage was held fixed for each differential conductance curve. Going from the bottom curve to the top curve, the fixed gate voltage is tuned from more negative to less negative, resulting in an increase of the conductance. The dense (dark part) curves regions, at $g = 2e^2/h, 2 \cdot 2e^2/h$, indicates that the conductance

barely changes by changing the gate voltage within those regions, signifying a plateau in terms of the conductance versus gate voltage. Basically, if the vertical center-cut (at $V_{sd} = 0$) of this differential conductance is extracted and is re-plotted it as a function of gate voltage, it should reveal the data in Fig.1.5(a). The numbers, 1 and 2 in panel (c), label the first and second linear quantized plateau. As can be seen, a conductance peak near zero bias, below the first quantized plateau, develops. This zero-bias peak will be refered to as a zero-bias-anomaly (ZBA) in the rest of this thesis.

When an in-plane magnetic field is applied, this ZBA starts to split at around B=2T, as shown in (d). The splitting of ZBA under a magnetic field is reminiscent of the Kondo effect in quantum dots[1, 20, 21]. A quantum dot is a puddle of localized electrons. When the electron number inside this quantum dot (puddle) is odd, the net spin is non-zero, giving rise to a localized magnetic moment. The free electrons in the Fermi sea outside the quantum dot will try to screen this localized magnetic moment, forming a spin singlet between the localized spin and the non-localized Fermi sea. This screening will give rise to a peak in the density of state at the Fermi energy. In terms of experiment, $dI/dV$ will show a zero-bias-peak for the odd filling number quantum dots. This many-body electron and spin correlation phenomenon in quantum dots is called the Kondo effect. This zero-bias-peak of $dI/dV$ in Kondo effect, will split into two peaks, if an in-plane magnetic field is applied. Thus the ZBA and its splitting in Fig.1.5(c)(d), look very similar to the well known Kondo effect.

In Kondo effect, besides this magnetic field dependence characteristics, the linear conductance as a function of temperature can be scaled into a universal function $f(T/T_K)$ with just one fitting parameter $T_K$, where $T_K$ is the Kondo temperature which defines the coupling strength between the quantum dot and the Fermi sea. Fig.1.5(e) shows this universal scaling of the ZBA by using a modified universal

function, $g = 2e^2/h[1/2f(T/T_K) + 1/2]$, where $f(T/T_K)$ is the universal function for the Kondo conductance. Different symbols represent the zero bias(linear) conductance at different gate voltages. As can be seen, the linear conductance for different gate voltages can be fit into this universal line, which again reminds us of the Kondo effect.

### *1.3.3 '0.7' Effect and ZBA: What is the physics behind them?*

The magnetic field and temperature dependence of the ZBA studied by ref[19] shows similarity with Kondo effects. But the story is more complicated than that. For example, the universal scaling of the conductance as a function of temperature, reported by Cronenwett *et al*[19], is not universally observed in QPCs. The properties of this ZBA has been studied in detail recently[22, 23, 24, 25, 26, 27, 28]. Chen *et al* proposed the idea of non-Kondo ZBA in quantum wires where the ZBA does not split even when the magnetic field is increased up to 10 T. Sfigakis *et al* show evidence that the energy scales of the '0.7' structure and ZBA are different, which suggests that the ZBA and '0.7' structure are two different electron correlation effects that coexist in QPCs.

Besides the experimental studies, many theory proposals have been offered for the '0.7' structure and the ZBA. For example, the smooth development of the '0.7' structure to '0.5' plateau by applying an in-plane magnetic field suggests spontaneous spin polarization in the QPC channel[16]. The Kondo-like proposal was also offered based on the experimental characteristics of ZBA[19, 29, 30, 31]. Besides these two models, there are also spin-gap models[32, 33, 34, 35], sub-band pinning models[33, 36], electron-phonon interaction[18], singlet-triplet effects[37, 38], charge density waves[39] and Wigner crystallization[6, 7].

Although the physics behind these two phenomena is still under heavy debate, one consensus is that they can not be explained by single particle picture, and are

the manifestation of many-body effects. This is why they have caught significant interests. For detailed discussion on these two phenomena, I refered to Micolich's review article[15].

In this thesis, I will present experimental evidence for potentially new types of electron correlation effects discovered in QPCs, for which the gate patterns are geometrically different from other groups'. The QPCs with asymmetric gates show different behavior compared with the traditional symmetric-gate QPCs. These asymmetric QPCs was first studied by the former PhD student, Dr. Phillip M. Wu in our group. The research is motivated by the theoretical proposals of Wigner crystallization [6, 7, 40, 41, 42, 8, 9], which were originally proposed to explain the '0.7' effect. Before digging into the Wigner crystal picture, I will first discuss the sample fabrication and experimental set-up in Chapter 2. In Chapter 3, besides a brief review for the theory of Wigner crystal, I will mainly discuss the experimental evidence of electron correlation effects discovered in asymmetric QPCs: the formation of electron-correlation-induced potential barriers in the QPC channels. Then in the analysis part, I will discuss the possible connections between our experimental signatures and the Wigner crystal characteristics, e.g. localized electron states and ferro-magnetic coupling. For this aspect of our findings, I refer to our two published papers[43, 44].

In Chapter 4, I will show the discovery of novel differential conductance oscillations as a function of bias voltage, which is another major result of this thesis. The systematic characterization of these oscillations suggests very interesting electron and spin correlation effects which is not fully understood by theory. By speculation, it would be interesting to try to relate these oscillations to the high spin states of Wigner crystals.

In the end, I will conclude this thesis in Chapter 5.

# 2

# Sample Fabrication and Experimental Measurement Set-up

The QPC samples were fabricated on the GaAs/AlGaAs crystal, grown by Melloch in Purdue University. The fabrication was done by patterning sub-micron sized metallic gates, using the standard state-of-art technique: electron beam lithography. Then all the electrical gates and current leads were connected to the pins of a sample holder, which is then placed into the He3 fridge and dilution refrigerator with base temperature of 300mK and 30mK, respectively. Low noise conductance measurement was then performed at the low temperatures.

## 2.1 Sample Fabrication: the State of Art

Fig.2.1 shows the schematics of the main fabrication steps. A GaAs/AlGaAs crystal wafer was first cleaved, along its lattice direction, to roughly a $2mm \times 2mm$ size chip. The cleaved chip was cleaned in acetone first and then isopropanol solution, in an ultrasonic environment(Paragon Electronics Bransonic B3510). The chemical solution and ultrasonic vibration help to dissolve and remove most of the dirt on the

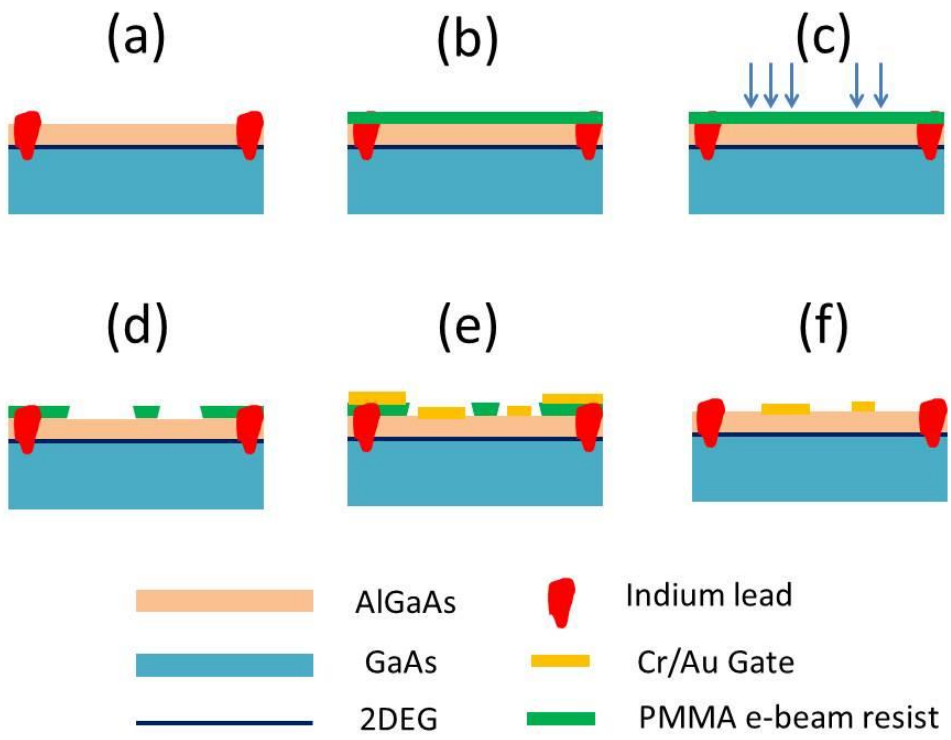


FIGURE 2.1: Sample fabrication: the state-of-art electron beam lithography. (a) Annealing indium leads(red) to make contacts with the 2DEG(dark blue). (b) Spinning electron beam photo-resist: PMMA(green). (c) Exposure of electron beam(blue arrows) on the chip. (d) Development in MIBK and then later IPA to dissolve the exposed PMMA part. (e) Evaporation. Evaporate Cr/Au metal gates (yellow) on the top of the chip (f) Liftoff. Dissolve the unexposed PMMA in acetone to remove the evaporated metal above it, leaving the metal in the exposed part.

surface of the chip. After the cleaning process, the chip was immediately blown dry with dry $N_2$ gas to prevent any solution residual left. Two pure Indium contacts were dropped on the surface of the chip. Then the chip was moved into a home-made annealing station. During the annealing, the chip was heated up to around $400^oC$ for $\sim$ 4 minutes, which is achieved by passing a large current through the nichrome wire near the chip. A $N_2$ ambient atmosphere environment is required to prevent any oxidization of the indium at this high temperature. Due to the heating, the indium on the surface of the chip will diffuse downward into the crystal, and

finally make electrical contacts with the 2DEG buried underneath the chip surface. The GaAs/AlGaAs chip after annealing is shown in Fig.2.1(a), where the indium leads(red) have made contacts with the 2DEG (dark blue).

After the annealing, a thin layer of polymer polymethyl methacrylate(PMMA) was added on the top of the chip, using a spincoater (Specialty Coating Systems P6700). A drop of PMMA solution was first dropped on the GaAs crystal surface. The chip was then immediately spinned up to 5500 revolutions per minute for $\sim 1$ minute. The 'centrifugal force' due to the high speed spinning will drive the PMMA away from the center. Finally after the spinning, a uniform thin PMMA layer was formed on the surface (green in Fig.2.1 (b)). Then the chip was baked dry for $\sim 30$ minutes to get rid of the solvent in the PMMA layer. The thin PMMA layer is roughly 160 nm thick, estimated based on the constructive interference of thin film for visible light under reflection.

After baking, it was ready to perform electron beam writing on the chip. The chip was moved into a scanning electron microscope (Leo 440 SEM) where the electron beam, after accelerated by a high electric field, can be focused by the current controlled magnetic coil lenses. The focused beam is roughly 10 nm in diameter, and its position can also be controlled by the magnetic lenses. Thus the controlled electron beam can be set to scan over a particular designed pattern. This so-called electron beam writing can achieve gate patterning with a resolution of sub-30nm, which is mainly limited by the size of the PMMA molecule and the proximity effect from the scattering of electrons. The high energy (30keV) elctron beam can cut the cross-links between PMMA molecules during exposure, where electron beam charge doses (the total amount of charge transferred to the PMMA by the beam) is roughly $100\mu C/cm^2$. This e-beam writing process is shown in Fig.2.1(c), where the e-beam(blue arrows) acts as a cutter to cut the PMMA.

The development was then performed after the e-beam writing, to get rid of the

exposed part of PMMA. The chip was moved out from the SEM and immersed in the developer solution: first methyl isobutyl ketone (MIBK) for 30 s and then isopropanol (IPA) for 5 s. The developer can dissolve the exposed PMMA with the cross-links cut by e-beam, while the unexposed PMMA will remain. The chip was then blown dry with $N_2$ gas. The chip after development is shown in Fig.2.1(d), where the exposed PMMA part was gone. There may be an extremely thin layer of PMMA remained in the exposed part. To get rid of this residue completely, radio frequency $O_2$ plasma etching can be performed for $1 \sim 2$ minutes. The ionized oxygen plasma will bombard the thin PMMA layer to 'eat up' the polymer residue.

Then the chip was moved into a vacuum chamber for metal evaporation. A large current was passed though a chrome rod, which will heated it up to a very high temperature, resulting in a high evaporation rate of Cr. These evaporated Cr will be deposited on the surface of the chip. By controlling the evaporation rate and time, 2nm thick chrome(Cr) was first deposited and later 12nm thick gold (Au) layer was added by replacing the chrome rod with gold in an evaporation boat. After evaporation, the chip is shown in Fig.2.1(e) where the yellow region represents the metal gates. The chip was then immersed in acetone solution to dissolve the PMMA layer. The metal on top of the PMMA will be lift off due to the dissolution of PMMA underneath but the metal in the rest part will remain and acted as the gate of QPCs for the remain experiment. To lift-off successfully, it is important for the PMMA file to have an undercut in the exposed region. This will cause the deposited metal to be discontinuous at the edges of the written pattern. This process is shown in Fig.2.1(f). Chrome was evaporated first due to the fact that Cr is very sticky to the GaAs/AlGaAs crystal surface. Thus the gate will stay tight and not fall off. Also Cr has a high resistivity to prevent it to be burned out when a spike of voltage was introduced during the wire bonding and measurement.

Finally all the annealed current leads and gates can be connected with golden

wires to the sample holder (14 pin DIP socket, Newark 614-AG1). Then the fabrication process for one typical sample was finished. The next step was to perform electrical test to see if all the gates and current leads work, e.g. if there was any current leak, short or open circuit. To do this, the sample and sample holder were moved onto one end of a sample stick which was later plugged into the low temperature Dewar to cool the sample down to low temperatures. The other end of the sample holder, outside of the Dewar, was connected with equipments to perform measurement for the sample in the Dewar.

## 2.2 Measurement Technique

Fig.2.2 shows the schematic of the basic electrical circuit diagram to measure the conductance of the sample. The dashed line box enclosing the sample indicates the part that was cooled down in the low temperature fridge. To be efficient, after the fabrication of each sample, the following steps were gone through first before the real systematic measurement. First, any measurement at room temperature needs to be avoid to protect the gates from any electrical breakdown: higher temperature makes the gate easier to be breakdown. Second, place the sample stick into liquid nitrogen (boiling point 77K) to test some very basic characteristics. For example, one can check to see whether there is any short between gates, or whether the indium leads make good contacts with the 2DEG. Negative gate voltages can be applied on the gates, but not too negative (e.g. do not go below -1V). A $10M\Omega$ resistor was connected in series with the gates to limit the leakage current and protect the gate. If all the above work, then liquid helium can be ordered to further test the sample at 4.2K (the boiling point liquid helium is 4.2K at pressure 1 atm). At this temperature, some basic measurement can be performed. For example, the quantized plateau can be observed, though the plateau structure will be very weak due to the thermal smearing. After analyzing the preliminary data obtained from this 4.2K test

measurement, we can plan on cooling down the He3 fridge and also get a rough idea on what should be measured.

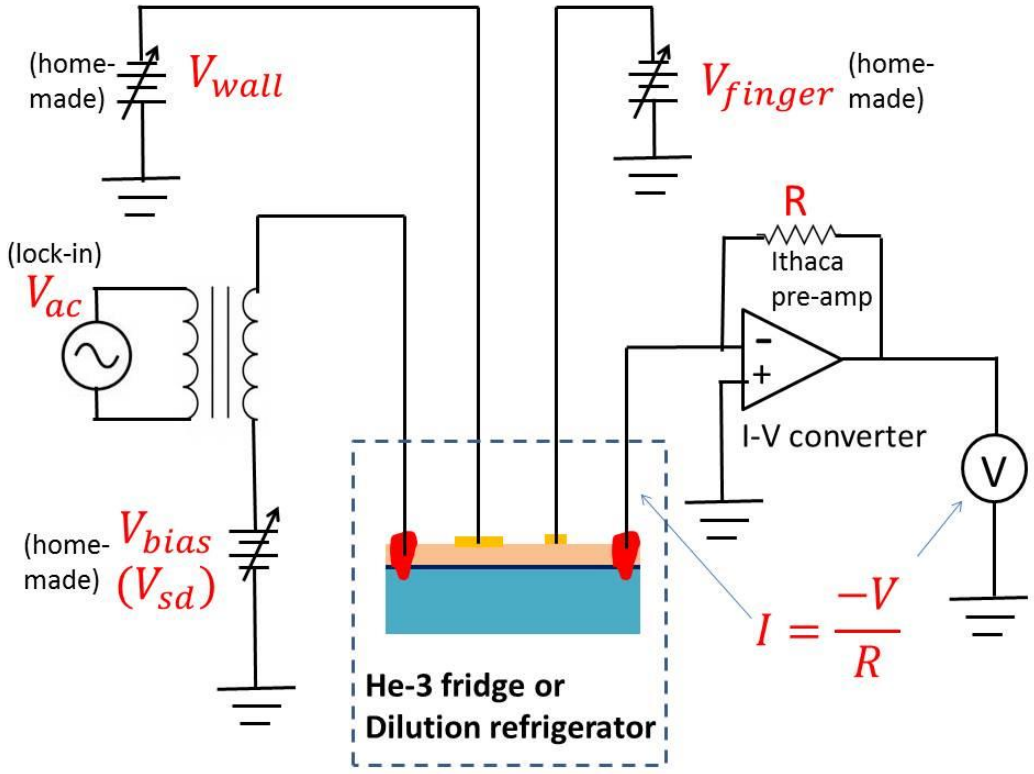


FIGURE 2.2: Measurement Circuit Set-up: red labels the measured electrical signals: voltage and current.

In the He3 fridge, the liquid helium-4 was first pumped, in a so-called 1K pot chamber, to reduce the vapor pressure, which reduces the temperature of helium-4 from 4.2K to $\sim 1K$. Making use of this 1K pot, helium-3 can be cooled to be liquified. Then the liquid helium-3 was pumped to further reduce the temperature from $\sim 1K$ to $\sim 300mK$. The cool down was finished when this 300mK base temperature was reached. Systematic measurement can be performed at this temperature. In addition, a sizable magnetic field can be applied by a superconducting NbSn/NbTi solenoid, which is immersed in helium-4 bath. The maximum current ($\sim 70A$), allowed in the solenoid, gives rise to a maximum magnetic field up to 6T in this

He3 fridge. After the systematic measurement and carefully analyzing the data, if lower temperature is needed, the same sample can be cooled down in the dilution refrigerator giving a base temperature below 30mK, and a magnetic field up to 13T can be applied. The principal of dilution refrigerator is based on the He3 fridge, but with an additional He3/He4 mixed chamber. By pumping this mixing chamber, the temperature can be cooled down to be below 30mK, where the principle is similar to the evaporative cooling of a cup of tea. For the technique and physics details about cryostat, I refer to these excellent books[45, 46, 47].

In Fig.2.2, the three DC voltage suppliers ($V_{sd}$, $V_{wall}$ and $V_{finger}$) are homemade which were controlled by the labview program in computer. $V_{ac}$ comes from the PAR124 lock-in amplifier, which is then superimposed, as an excitation, on $V_{sd}$ by coupling $V_{ac}$ through a transformer as shown in the figure. Following the circuit in the figure from the bottom left, a bias voltage ($V_{sd}$), with a small excitation $V_{ac}$, was applied on the left indium (red) current lead. This voltage will drive a current through the 2DEG and also the nano-device (QPC) defined by the negative voltage ($V_{wall}$ and $V_{finger}$) applied on the two metal gates (yellow). The current then reached the right indium (red) current lead, which connects the negative input of an operational amplifier (op-amp). Based on the characteristics of the op-amp, the right indium current lead was virtually grounded. Thus the total voltage applied across the sample is $V_{sd} + V_{ac}$. To get the conductance, the current through the sample under this voltage was measured using the current-voltage converter labeled in the figure. The principle of this I-V converter is based on the negative feedback op-amp circuit with a resistor connecting the output of the op-amp to the input. The resistor converts the current from the sample to a voltage through $V = -IR$. The I-V converter was either home-made or Ithaco 1211 pre-amp. After converting the DC and AC current into DC and AC voltage, the AC voltage was measured from the lock-in amplifier which can 'pick up' the AC signal which has the same

frequency with $V_{ac}$. All the electronic signals are measured by HP multimeters and then recorded in the computer.

Finally we got the following physical quantities, which were measured in the experiment: gate voltages ($V_{wall}$, $V_{finger}$), $V_{sd}$, $V_{ac}$ and $I_{ac}$, where $I_{ac}$ was obtained from the I-V converter. $I_{ac}$ divided by $V_{ac}$ gives the differential conductance $dI/dV$ for a fixed $V_{sd}$, $V_{wall}$ and $V_{finger}$. The excitation $V_{ac}$, in principal, needs to be infinitely small (otherwise, $dI/dV$ will not be the 'differential' conductance but the 'finite difference' of conductance). In terms of experiment, $V_{ac}$ needs to be less than the thermal broadening of the Fermi function ($3.5k_BT \sim 9\mu eV$,at T=30mK). If the $V_{bias}$ is set to be 0, then this $dI/dV$ (at $V_{sd} = 0$)is the linear conductance. The scanning range of $V_{bias}$ need to be on the order of the energy level spacing between the neighboring sub-bands, shown in Fig.1.3(c). Thus $V_{bias}$ was varied between $\sim -2mV$ and $\sim 2mV$. Basically, all our data consists of the conductance as a function of $V_{sd}$, $V_{wall}$, $V_{finger}$, magnetic field applied by the superconducting magnetic, and temperature. As I will show in the next two chapters, novel quantum many-body physics can be extracted from this 'multi-variable' conductance function data.

# 3

# Electron Correlation Effects in Asymmetric QPCs: Correlation-induced-barriers

In this chapter, I will first introduce the research about the Wigner crystallization in QPCs. This novel strong electron correlation state is also the motivation of our research. Then, I will present the experimental evidence for electron correlation effects, in both the linear and differential conductance of our QPCs. The linear conductance shows resonances and the modulation of quantized plateaus, which are ascribed to the electron-correlation induced barriers. In theory, the Quantum Monte Carlo numerical calculation performed by Guclu *et al*[8] and Mehta *et al*[9], and Spin Density Functional Theory performed by Welander *et al*[48] and Yakimenko *et al*[49] , predict that in QPCs with sharp potential profile, Wigner crystallization states can be formed with electron-correlation barriers coexist in the QPC channel. The modulation (suppression) of the quantized plateau might be related with the zigzag quantum phase transition in the Wigner crystal states, as was proposed by Hew *et al*[50, 51, 52] and Smith *et al*[53, 54], both from Pepper's group. Besides the linear conductance, I will present the near even-odd law based on the appearance of the zero-bias-anomaly (ZBA) in the differential conductance. This near-even-odd

rule may also be interpreted in this electron-correlation-barrier picture, which helps to localize the electrons, in a manner similar to a quantum dot. In the end of this chapter, I will present a triple-peak structure in $dI/dV$, which suggests the formation of a spin triplet state. Speculate further, in the future, it would be interesting to try relate this ferro-magnetic type of interaction to the theory of possible ferro-magnetic correlations in Wigner crystal[6, 40, 41, 55].

## 3.1 Wigner Crystallization in QPCs

It was first predicted by Wigner that in the low density limit where the electron Coulomb potential energy dominates over the electron kinetic energy, electrons will form an ordered crystal lattice to minimize the system energy[3]. This classical Wigner crystal has been observed on the surface of liquid helium[56], where the electron density is too low so that the electron system is non-degenerate. When the electron system is degenerate, in which the quantum nature of electrons gets involved, the theory predicts that the 1D electron lattice will be destroyed by quantum fluctuation[57, 58, 7]. Thus a perfect 1D (infinite long) electron system can not have the long-range order. However, the short-range order can be remained in a quasi-1D channel, such as in a QPC. Matveev and Klironomos *et al* have addressed this issue by considering electrons confined in a 1D confining potential, mimicking the QPC gates. Their calculation shows that as the electron density is lowered, the Coulomb interactions lead to a short-range crystalline order of electrons[7, 40, 41, 42]. Fig.3.1(a) shows the schematic of Matveev's calculation result, where the electrons (white dots) get localized into a lattice between the two QPC gates (shaded). More interestingly, their calculation shows that if the electron density is increased, the 1D Wigner crystal state goes through a phase transition into a zigzag crystal states. This zigzag phase transition is shown in Fig.3.1(b), where $\nu$ is a parameter proportional to the electron density. As can be seen, when $\nu$ increases from the left to

the right, the Wigner crystal experience a phase transition from a straight 1D into a zigzag quasi-1D. Although it have been proved, by Lieb and Mattis that a strictly 1D electron system, subjected to a symmetric potential, can not have a ferromagnetic ground state[10], the theory for the zigzag state in QPCs allows the formation of possible ferromagnetic states, in a particular density and coupling parameter regime. This ferromagnetic coupling is due to the more complicated multi-electron exchange interaction[40, 41].

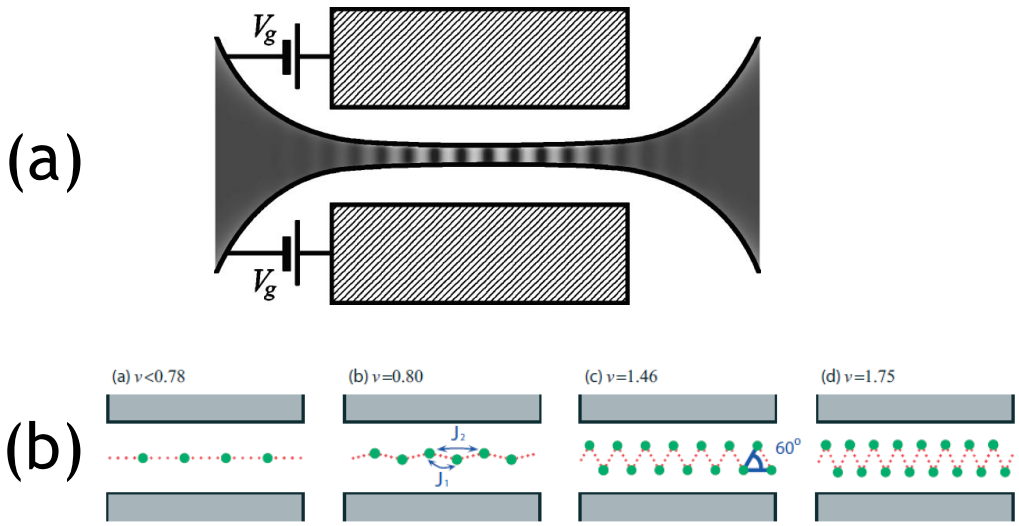


FIGURE 3.1: Wigner crystallization and zigzag phase transition (a) Sketch of electron density in a quantum wire formed by confining two-dimensional electrons with gates (shaded). This figure is taken from Ref[7]. (b) Wigner crystal of electrons in a quantum wire defined by gates (shaded). As the electron density related parameter $\nu$ is tuned from left to right, the Wigner crystal goes through a zigzag phase transition. This figure is taken from Ref[40]

In the meantime, the Wigner crystal ordering, and the zigzag phase transition induced by an increase of electron density, were also predicted in numerical calculations performed by Guclu *et al*[8], Welander *et al*[48] and Mehta *et al*[9]. These numerical calculations, which are based on Quantum Monte Carlo method and Spin Density Functional theory, respectively, will be discussed later in this chapter for the

possible connections related to our experimental data.

Besides the theory, Hew *et al* and Smith *et al* have systematically studied the electron transport of weak confined QPCs, where the QPC confine potential, created by the split gates, is weak and smooth[50, 51, 52, 53, 54]. Their measurement shows the half plateau ($0.5e^2/h$) and also the suppression of the first quantized plateau. They ascribe this sudden conductance jump, which jumps from 0 directly to $2e^2/h$, to the formation of the double row Wigner crystal. The half plateau and the suppression of first plateau are only observed in the weak confinement regime, while in the the strong confinement regime, the conductance behaves normal and is within the single-particle picture. As I will show later, the suppression (or modulation) of quantized plateaus are also generally observed in our asymmetric QPCs. But our asymmetric QPCs have a strong confinement (probably even stronger than the strongest case in Hew *et al* and Smith *et at*'s system by comparing the crystal and gate parameters). Thus whether the modulation of plateaus in our system is related with Hew *et al* and Smith *et al*'s, remains an unresolved question.

## 3.2 Linear Conductance of Symmetric QPCs versus Asymmetric QPCs

Below I will present the electron transport data in our QPCs. Part of the data shown in this chapter is published in Ref[43] and Ref[44].

Fig.3.2 shows the difference of the gate geometry between a symmetric QPC and an asymmetric QPC. Panel (a) is taken from Dr. Phillip Wu's thesis[59]. Panel (a) and (b) are the SEM images of a symmetric and an asymmetric QPC, respectively. The metal gates, in panel (a)(b), are the regions which look brighter. As can be seen, the symmetric QPC has two symmetric split gates while for the asymmetric QPC, one split gate (the bottom one) is replace with a longer gate. To differentiate these two gates of the asymmetric QPC, as labeled in panel (b), the short gate, which also defines the lithographic channel length, is named finger gate. The other

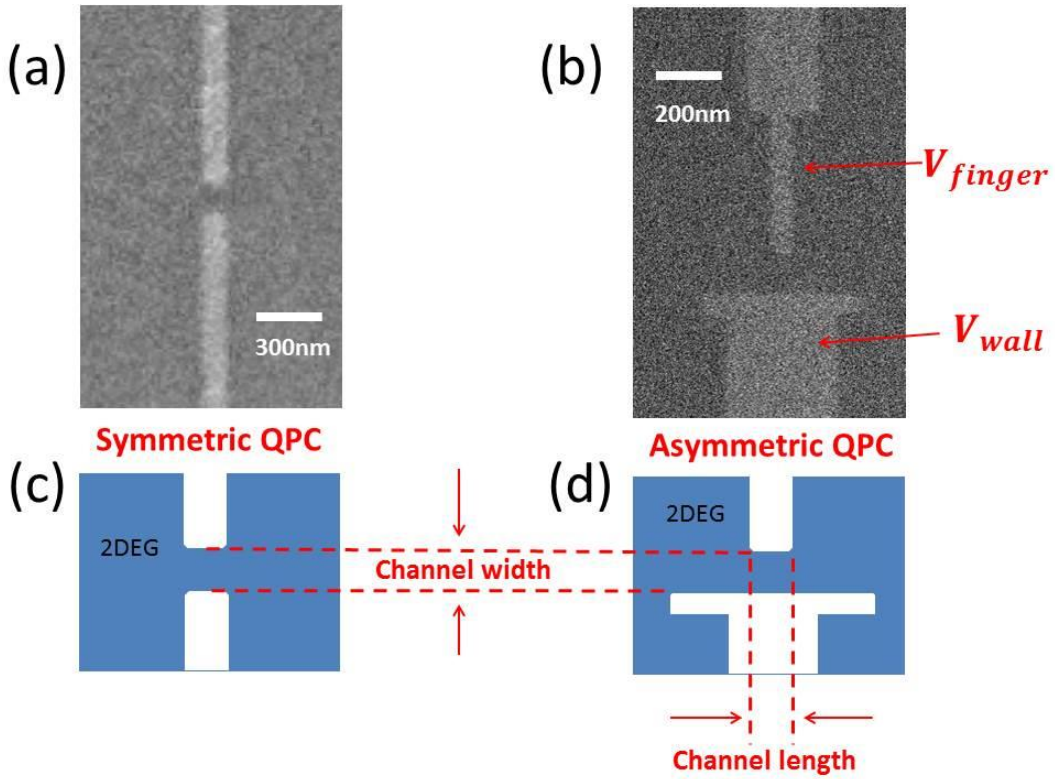


FIGURE 3.2: Geometry of a Symmetric QPC versus an Asymmetric QPC: (a) the Scanning Electron Microscopic (SEM) image of a symmetric QPC (taken from Phillip Wu's thesis[59]. (b) SEM image of an asymmetric QPC. (c) The schematic of the 2DEG and QPC, corresponding to (a) when negative gate voltage is applied. (d) The schematic of the 2DEG and QPC, corresponding to (b), with negative gate voltage applied. The finger voltage, wall voltage, lithographic channel width and channel length are denoted in the red text.

gate is labeled as wall gate. The gate voltages are $V_{finger}$ and $V_{wall}$, respectively. Panel (c) and panel (d) are the schematics for panel(a) and panel (b), respectively. The blue region represents the two-dimensional electron gas (2DEG) and the white regions represent the depleted gate regions. Two important parameter of the gate geometry are labeled in panel (c) and panel (d): the channel width (the gap size between the two split gates) and the channel length (the length of the finger gate for the asymmetric QPC). These two parameters are the lithographic sizes, which are not exactly the effective channel width and length of the quasi-1D electron system.

In particular, the effective width is reduced from the lithographic width due to the depletion of electrons directly below and in the vicinity of the gates. The QPC conductance behaviors will be studied at high temperature first, and then at lower temperatures.

### *3.2.1 High Temperature Data*

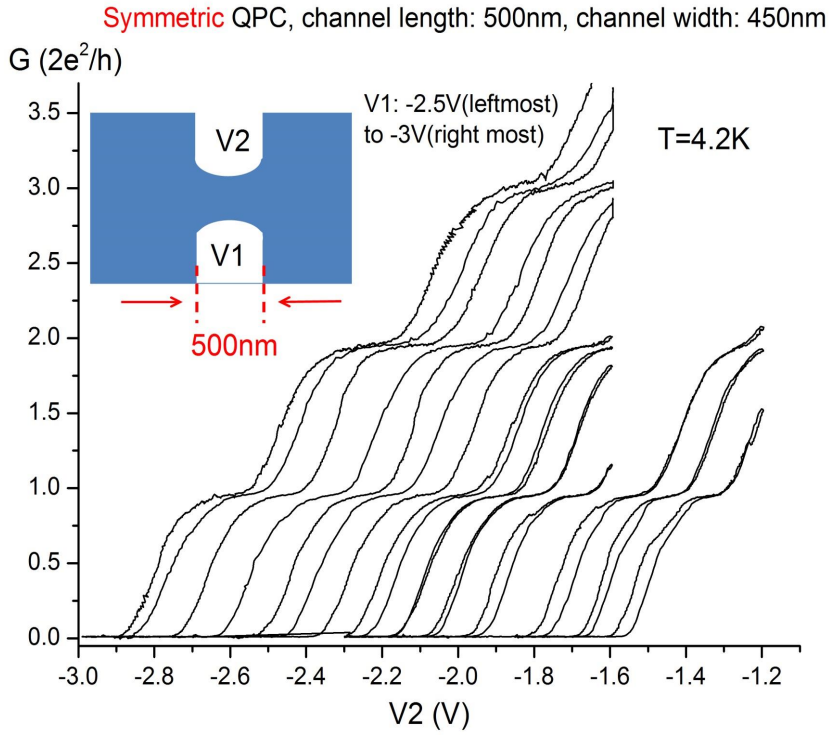


FIGURE 3.3: Linear conductance of a symmetric QPC measured at T=4.2K. The channel length is 500nm, and the channel width is 450nm (450nm at center, opening up parabolically to 680nm at the ends). For each curve, one gate voltage (V1) is held fixed, while the other gate voltage (V2) is scanned. The leftmost curve corresponds with a fixed $V1$ at -2.5V while the rightmost one corresponds with fixed $V1$ at -3V. The inset shows the schematic of this symmetric QPC. Figure from Ref[44]

Fig.3.3 shows the linear conductance of a symmetric QPC measured at 4.2K. Our measurement set-up is different from the traditional conductance measurement, in which the two split gates are hooked up together and the same gate voltage is

applied to the two gates. Thus the conductance as a function of gate voltage is typically a single step-like curve, as shown in Fig.1.2 and Fig.1.5. Here for our case, the QPC gates were gated asymmetrically: different gate voltages were applied to the two gates. During the measurement, one gate voltage(V1) was held fixed, while the other gate voltage(V2) was scanned to obtain a step-like conductance curve. Then V1 was changed to another fixed value, and V2 is again scanned to obtain another conductance curve. This process was repeated for several fixed V1 values. Finally a bunch of conductance curves, laterally shifted due to the different fixed V1s, can be obtained. The reason to do so is due to the fact that this asymmetric gating helps to access a larger phase space of the potential profile, which is created by the gate voltages. As will be shown later, the electron transport behavior is very sensitive to the potential profile. Thus the asymmetric gating, in principal, can give richer behavior and makes it easier to track and study the evolution of novel structures. Fig.3.3 shows the well established quantized plateau at a relatively high temperature with T=4.2K. Throughout this thesis, every linear conductance curve was measured by scanning the gate voltage forward (from left to right) and backward (from right to left) at different scanning speeds. And the linear conductance curves measured by forward and backward scanning are consistent.

To compare with the symmetric QPC, Fig.3.4 shows the linear conductance of an asymmetric QPC at the same temperature. All the linear conductance measurement in this thesis is measured using an asymmetric gating which has a similar set-up with Fig.3.3. In this Fig.3.4, the wall gate voltage ($V_{wall}$) was held fixed for each conductance trace, while the finger gate voltage ($V_{finger}$) was swept. As can be seen by comparing Fig.3.4 with Fig.3.3, besides the well established quantized plateau which they both have, the asymmetric QPC conductance shows two extra features for which the symmetric QPC does not show. The first feature is the small conductance resonances below the first quantized plateau ($2e^2/h$). And the second feature

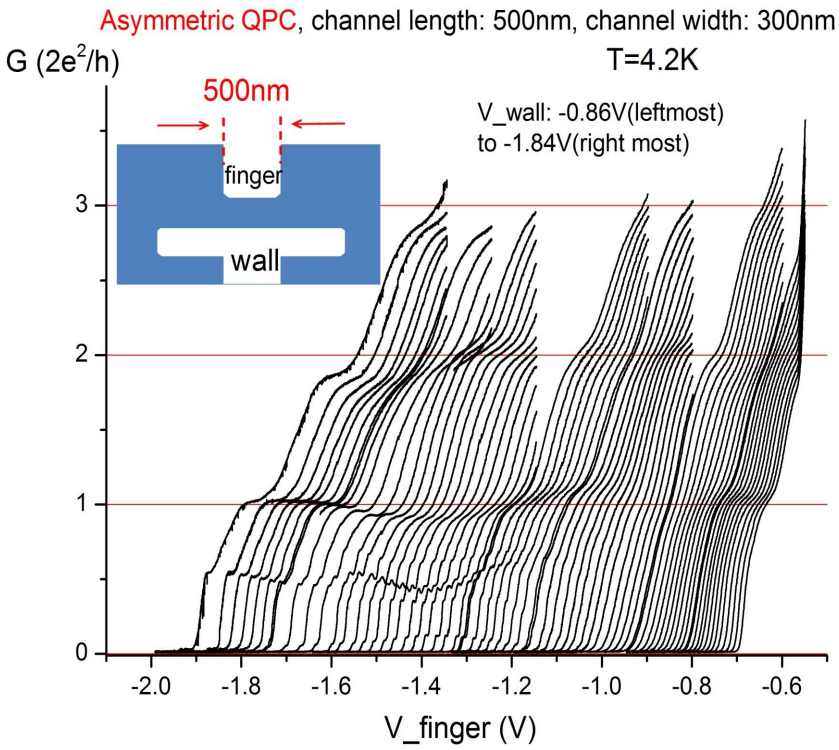


FIGURE 3.4: Linear conductance of an asymmetric QPC at T=4.2K. The channel length is 500nm, and the width is 300nm. For each curve, $V_{wall}$ was held fixed while $V_{finger}$ was scanned. $V_{wall}$ is -0.86V for the leftmost curve, and -1.84v for the rightmost one. The inset shows the geometry of this symmetric QPC. The horizontal red lines help to position the multiples of $2e^2/h$. Figure from Ref[44]

is the modulation of the quantized plateau as the conductance traces move from the leftmost to the rightmost, which is tuned by $V_{wall}$. The red horizontal lines in the figure position the multiples of $2e^2/h$, which helps to better track the plateau modulation. In the right part of Fig.3.4, where $V_{finger}$ is around -1V, the first quantized conductance plateau is suppressed while the second plateau still survives.

This jumping of conductance, from 0 directly to $2 \times 2e^2/h$, was first reported by Pepper group: Hew *et al*[50, 51, 52] and Smith *et al*[53, 54], where they claimed a formation of a double row Wigner crystal. In an intuitive picture, one can think of each row as a conducting channel (sub-band) which contributes the conductance of

$2e^2/h$. Thus jumping to $2 \times 2e^2/h$ may be interpreted as the forming of a double row crystal. However, our QPC system is quite different from these two groups'. First, our gate geometry (potential profile) is asymmetric, while their geometry is symmetric. Second, they found the suppression of the first quantized plateau in the weak confinement regime, but not in the strong confinement regime, while our QPC system probably has even a stronger confinement than their strongest confinement case. This is because that the gate is only 85 nm above the 2DEG for our samples, instead of 300 nm for their samples. This close distance between the gates and the 2DEG makes the potential profile in our sample sharper and stronger than the Pepper group. Besides this, the channel width (700nm) in their system is also wider than our typical channel width (300 nm), resulting in a much smoother potential profile in their system. Therefore, there may not be any overlap in the confinement potential profile regime between the two systems. As the QPC properties are very sensitive to the potential profile, we can not be completely sure whether our suppression of the quantized plateau is related to their observation or not.

Besides the modulation of the quantized plateau, the conductance resonances represent another significant feature we want to address in this asymmetric QPC. Though the main resonance series are located at $0.5 \times 2e^2/h$, which is reminiscent of the half plateau discovered in the weak confinement regime by Hew *et al*[50, 51, 52] and Smith *et al*[53, 54]. Besides the big confinement potential profile difference discussed above, unlike Hew *et al* and Smith *et al*'s data[50, 51, 52, 53, 54], these 'half' plateau series observed in our system, disappear and become resonances when the temperature is cooled down to 0.3K. Thus we will treat these 'half' plateaus as resonances. As will be discussed later, these resonances are possibly related to and caused by the electron-correlation induced barriers formed in the QPC channel.

The conductance resonances and the modulation (suppression) of quantized plateaus are the two main features, in the linear conductance of our asymmetric QPCs. These

two features were studied at lower temperatures as shown below.

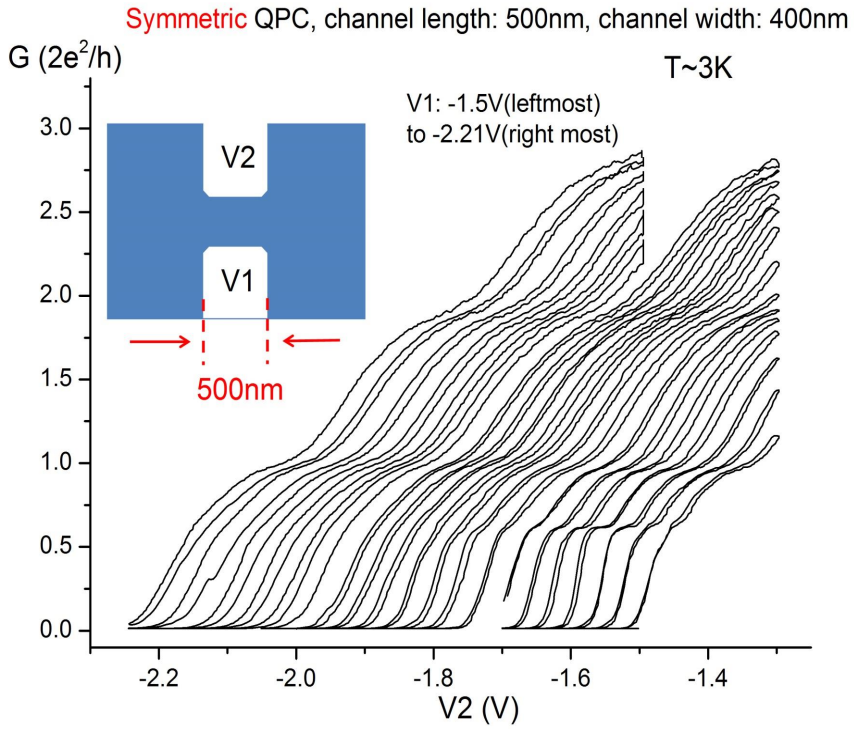


FIGURE 3.5: Linear conductance of a symmetric QPC at T=3K. The channel length is 500nm, and the width is 400nm. For each curve, $V_{wall}$ was held fixed while $V_{finger}$ was scanned. $V_{wall}$ is -1.5V for the leftmost curve, and -2.21v for the rightmost one. The inset shows the geometry of this symmetric QPC.

Fig.3.5 and Fig.3.6 shows the linear conductance data for another set of symmetric QPC and asymmetric QPC measured at T=3K. The two samples have the same lithographic channel length(500nm) and channel width (400nm). They were also fabricated together in the same electron beam exposure on the same crystal chip. Finally they were measured together in the same cool down. As can be seen, the asymmetric QPC (Fig.3.6) shows conductance resonances and the modulation of the quantized conductance plateau while the symmetric QPC (Fig.3.5) does not show any of these two features besides the '0.7' structure[16] in the the rightside. The symmetric QPCs are used as a control group, which can help to rule out the

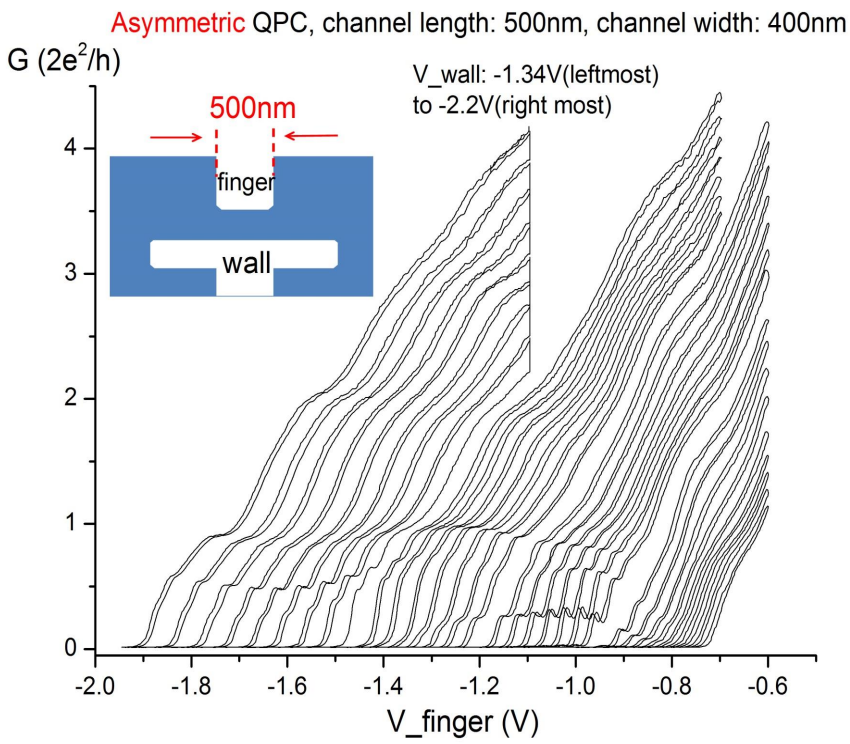


FIGURE 3.6: Linear conductance of an asymmetric QPC at T=3K. The channel length is 500nm, and the width is 400nm. For each curve, $V_{wall}$ was held fixed while $V_{finger}$ was scanned. $V_{wall}$ is -1.34V for the leftmost curve, and -2.2v for the rightmost one. The inset shows the geometry of this symmetric QPC. Fig.3.6 and Fig.3.5 were measured in the same cool down. The two samples were fabricated on the same crystal chip in the same electron beam lithography.

impurity induced features in asymmetric QPCs. Because impurity effect, if exist, should be present for both symmetric and asymmetric QPCs. This impurity effect will be discussed in detail later in the discussion section.

### *3.2.2 Low Temperature Data : 300mK in He3 Fridge*

Fig.3.7 and Fig.3.8 show the linear conductance of two symmetric QPCs with channel length 100nm and 500nm, respectively. The temperature is 300mK. Fig.3.7 is taken from Phillip Wu's thesis. As can be seen, the symmetric QPCs show quantized conductance plateaus which is expected from the single particle picture. No conduc-

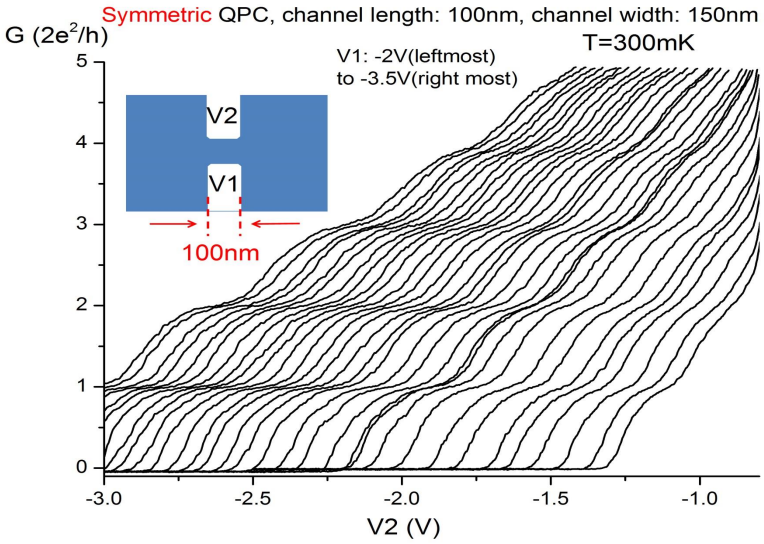


FIGURE 3.7: Linear conductance of a symmetric QPC at T=300mK. The channel length is 100nm, and the channel width is 150nm. For each curve, $V1$ was held fixed while $V2$ was scanned. $V1$ is -2V for the left most curve, and -3.5v for the right most one. The inset shows the geometry of this symmetric QPC. Figure from Ref[43].

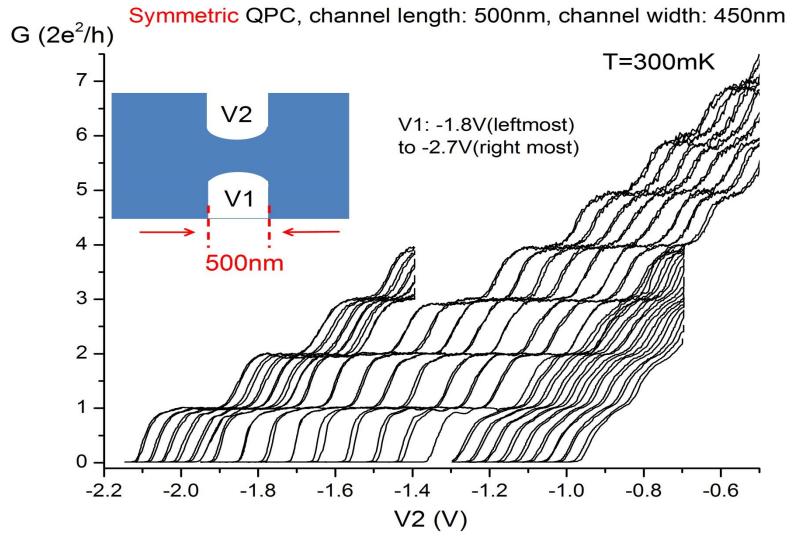


FIGURE 3.8: Linear conductance of an symmetric QPC at T=300mK. The channel length is 500nm, and the width is 450nm. For each curve, $V1$ was held fixed while $V2$ was scanned. $V1$ is -1.8V for the left most curve, and -2.7v for the rightmost one. The inset shows the geometry of this symmetric QPC. This figure and Fig.3.3 were measured from the same sample

tance resonances and modulation of quantized conductance plateaus are observed in these two symmetric QPCs at T=0.3K.

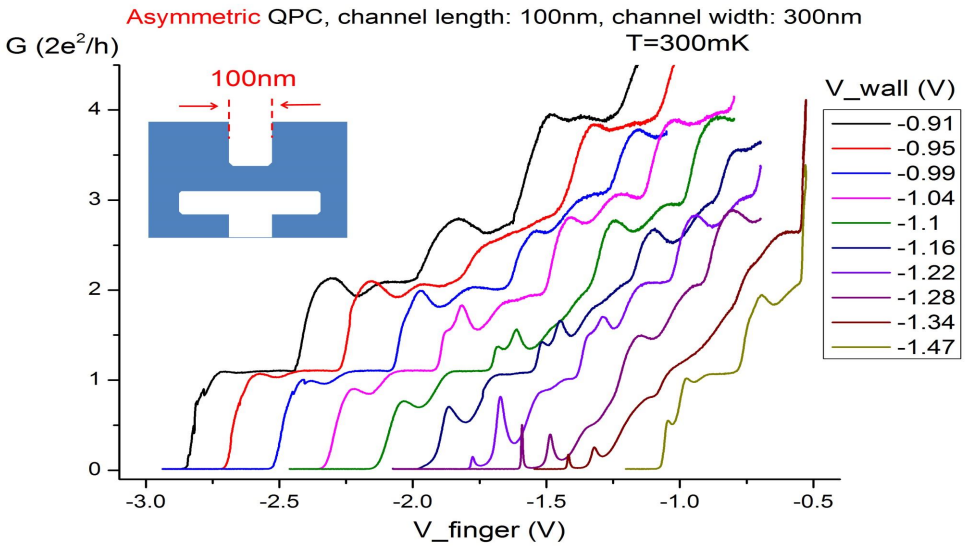


FIGURE 3.9: Linear conductance of an asymmetric QPC at T=300mK, Channel length (width): 100nm (300nm). For clarity only 10 out of 23 curves are shown here. For each colored curve, $V_{wall}$ was held fixed while $V_{finger}$ was scanned. The fixed $V_{wall}$ for each colored curve is shown in the label. The inset shows the geometry of this asymmetric QPC.

Now we switch to the linear conductance behavior of asymmetric QPCs at T=300mK. Fig.3.9 shows this case for an asymmetric QPC with a channel length 100nm. For clarity, Fig.3.9 only shows around half of the measured traces. Different traces, which have different fixed $V_{wall}$s, were assigned with different colors, as denoted in the legend. As can be seen from Fig.3.9, sharp conductance resonances are developed. When $V_{wall}$ is tuned, the positions of these resonances are also modulated. Fig.3.9 also shows flat well established quantized plateau for most of the curves. For some traces, e.g. the purple curve in the middle, the first quantized plateau is completely suppressed.

Fig.3.10, Fig.3.11 and Fig.3.12 show the linear conductance behavior for asymmetric QPCs with longer channel lengths: 300nm, 500nm and 1000nm, respectively.

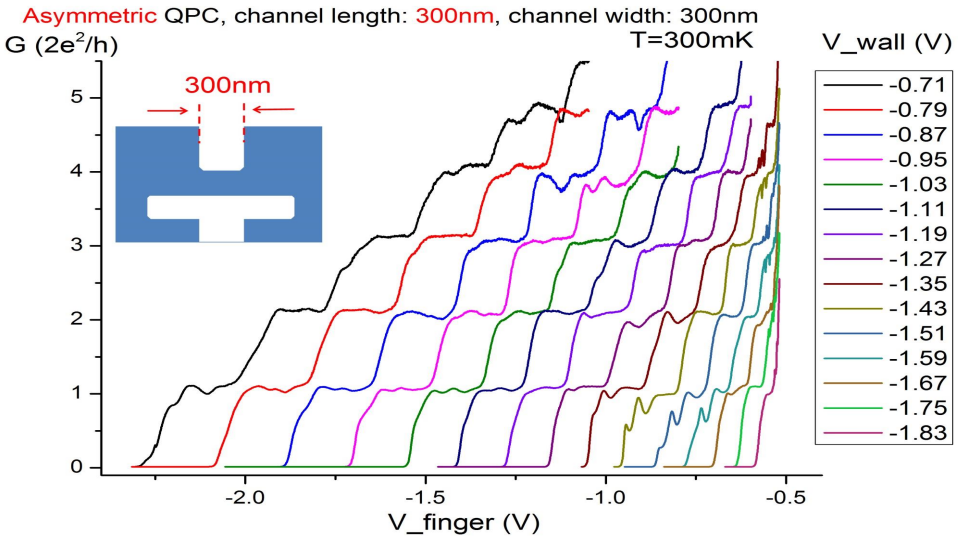


FIGURE 3.10: Linear conductance of an asymmetric QPC at T=300mK. The channel length is 300nm, and the channel width is 300nm. For clarity only 15 out of 61 curves are shown here. For each colored curve, $V_{wall}$ was held fixed while $V_{finger}$ was scanned.

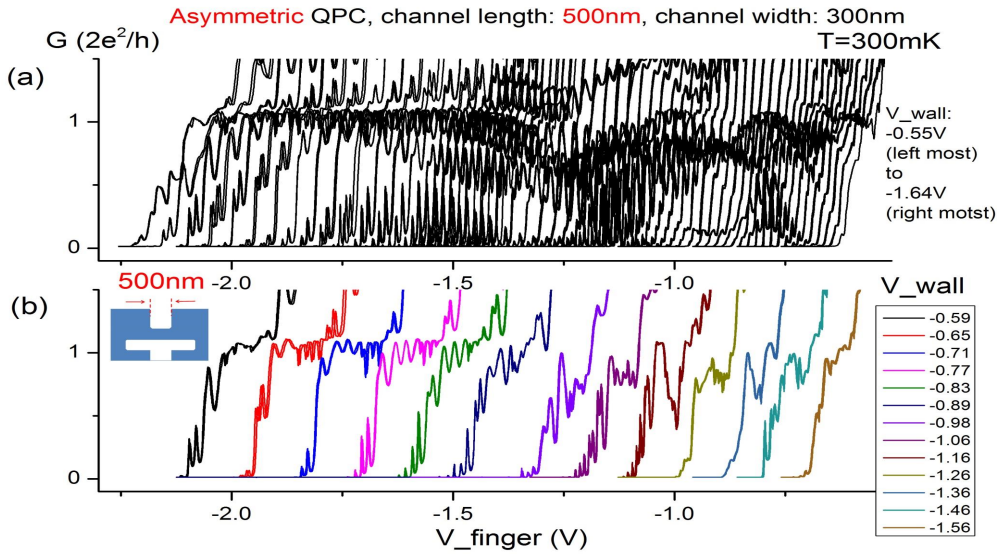


FIGURE 3.11: Linear conductance of an asymmetric QPC at T=300mK. The channel length is 500nm, and the channel width is 300nm. (a) shows all the linear conductance curves (64 curves in total). Part of the curves in (a) are shown in (b) for clarity. For each colored curve in (b), $V_{wall}$ was held fixed while $V_{finger}$ was scanned.

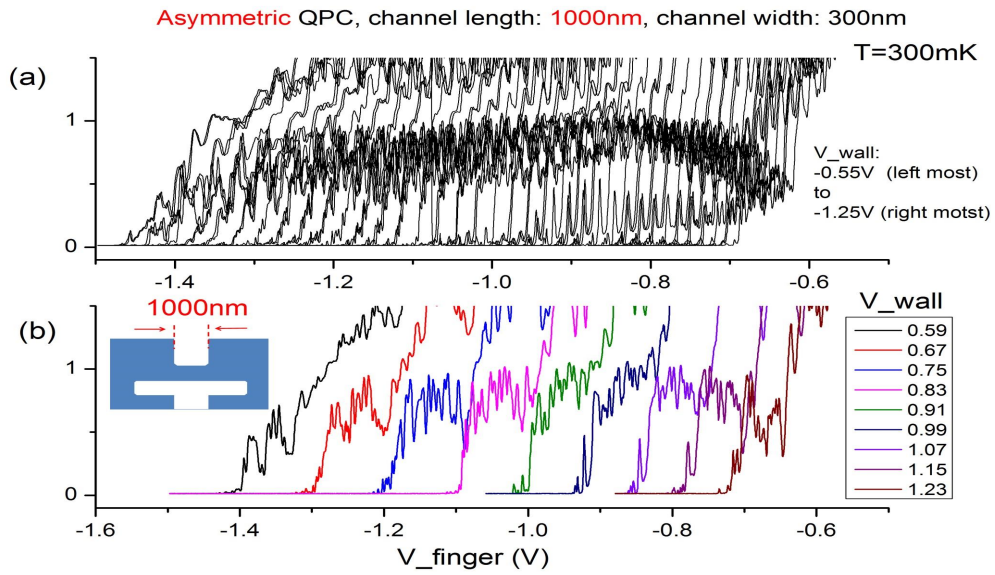


FIGURE 3.12: Linear conductance of an asymmetric QPC at T=300mK. The channel length is 1000nm, and the channel width is 300nm. (a) shows all the measured linear conductance curves (37 in total). Part of the curves in (a) are shown in (b) for clarity.

For clarity, only around one quarter of the measured curves were shown, and assigned with colors. In Fig.3.11(a) and Fig.3.12(a), all the curves were shown. Though it looks dense and messy in this way, it gives a general trend of the development of these conductance resonances, from the left to the right in the figures.

Based on the four asymmetric QPCs with the channel length varied from 100nm to 1000nm, we can see that the conductance resonances and the modulation of quantized plateau are the general features in asymmetric QPCs. Fig.3.9, Fig.3.11(a) and Fig.3.12(a) clearly show the modulation of quantized plateau (if we track the dark (dense curve) region in the latter two), while Fig.3.10 also shows the modulation (though not so obvious compared to the other three) near the rightmost side.

Besides the modulation of the quantized conductance plateau, a clear trend for the number of conductance resonances vs the channel length can be obtained for the four asymmetric QPCs. As the channel length increases from 100nm to 1000nm (from Fig.3.9 to Fig.3.12), more (or denser) conductance resonances are observed.

To gain some statistics, the number of resonances for each individual curve was counted. Taking Fig.3.11(a) as an example. There are 64 conductance traces for this asymmetric QPC. The number of resonances below the first quantized plateau ($2e^2/h$) is counted for each trace. The mean, minimum and maximum number of resonances below the first plateau, for these 64 curves, were calculated and plotted as three points (representing min max and mean) in Fig.3.13(a). We did calculate the standard deviation (or error bar) for these 64 curves. But since different curves correspond to different $V_{wall}$s and different confinement potential profiles, in principal, they are not expected to show the exactly the same number of resonances. In this sense, presenting the mean, minimum and maximum is a better statistical way than the standard deviation method.

Table 3.1: Number of curves for each QPC sample

| Sample | # 1 | # 2 | # 3 | # 4 | # 5 | # 6 | # 7 | # 8 |
|---|---|---|---|---|---|---|---|---|
| Channel length (nm) | 100 | 300 | 500 | 1000 | 100 | 300 | 500 | 700 |
| Channel width (nm) | 300 | 300 | 300 | 300 | 250 | 250 | 250 | 250 |
| Number of Curves | 23 | 61 | 64 | 37 | 37 | 50 | 54 | 47 |

Table3.1 shows the number of conductance traces for the eight asymmetric QPCs, measured systematically, with different channel length and channel width. Part of the conductance date of Sample 1-4 are already shown in Fig.3.9, Fig.3.10, Fig.3.11 and Fig.3.12. The conductance data of Sample 5-8 show similar behaviors, and is not shown here. After calculated the mean, maximum and minimum number of resonances below the first quantized plateau for each sample, the statistics are shown in Fig.3.13. Panel (a) shows the statistics for sample 1-4, as labeled in Table3.1. These four asymmetric QPCs have the same channel width (300nm) but different channel length. Panel (b) shows the statistics for sample 5-8. Panel (c) presents

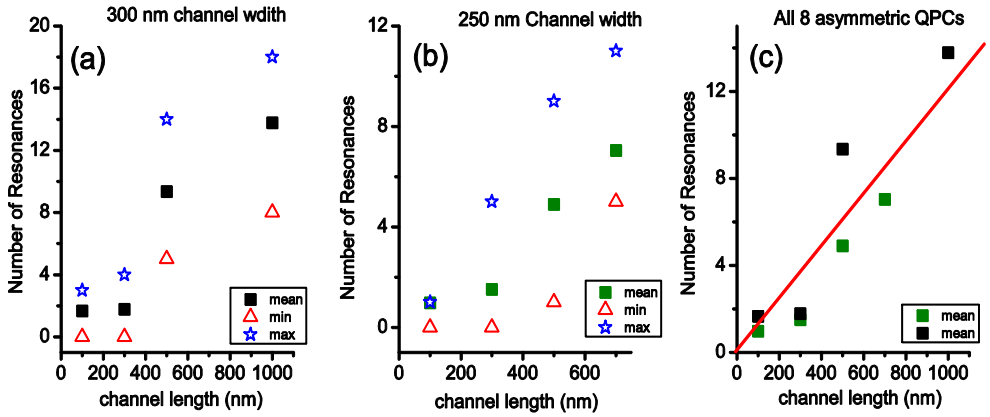


FIGURE 3.13: The statistics for the number of resonances below the first quantized plateau for all eight asymmetric QPCs. (a): mean, maximum and minimum number of resonances for sample 1-4. (b): for sample 5-8. (c): the mean number of resonances for sample 1-8.

only the mean number of resonances for all the 8 asymmetric QPCs as a function of QPC channel length. The red line is a qualitative linear fitting of the 8 data points. This statistics shows a general trend of the positive correlation between the number of resonances and the QPC channel length.

### *3.2.3 Discussion: the Intrinsic Nature of the Resonances and the Modulation of Plateaus for Asymmetric QPCs*

A natural question, regarding these conductance resonances, is to ask whether they are due to the impurity scattering inside the QPC channel. For example, an ionized Si dopant, above the QPC channel in the doping layer, can cause the scattering of electrons in the QPC channel, through Coulomb interaction. This scattering process can give rise to the conductance resonances. If this were the case, then the conductance resonances observed in our asymmetric QPCs, would not be the intrinsic property of the 1D electron system, and would be much less interesting.

McEuen *et al* have reported the conductance resonances in QPCs due to this kind of impurity scattering[60]. One characteristic of these impurity-induced resonances,

found by McEuen *et al*, is that the conductance resonances can not be reproduced by thermal cycling. This means that if the sample is warmed up and then cooled down, the conductance resonances may not show up again. This is due to the property of GaAs/AlGaAs crystal: Si donor impurities in the crystal can randomly 'decide' to ionize or not, at room temperature or even below 77K, but will be frozen at low temperature below $\sim 20K$. Thus after thermal cycling, the ionized impurity spatial distribution will be different from before. And the ionized impurities, which were located above the QPC channel and caused the scattering, may not be ionized to cause the scattering in the second cool down. Thus for different cool downs, the impurity-induced effects can not be reproduced.

Since the conductance resonances, in our asymmetric QPCs, can be qualitatively (with some lateral shift) reproduced by thermal cycling, this helps us to differentiate the conductance resonances observed in our system from the resonances due to the dirt effects in Ref[60].

Besides this approximate thermal cycling reproducibility, the electron mobility, in the GaAs/AlGaAs crystal, suggests that the transport is ballistic. In Chapter 1.2, where the quantized plateau of QPC is explained in a single-particle picture, one important hidden assumption is that the transmission probability of electrons through the QPC channel is unity. This requires the electron transport through the channel to be ballistic. Otherwise, the back-scattering, caused by impurities located above the QPC channel, will reduce the transmission probability and degrades the quantized plateau[14]. One physical quantity to measure this scattering effect is the electron mean-free-path. If the electron mean-free-path is much longer than the QPC channel, then the transport is likely ballistic, even though the gating reduces the carrier density and mobility somewhat, by a factor of $\sim 3$ in the worst case. The electron mobility of our GaAs/AlGaAs is measured to be $\mu = 9 \times 10^5 cm^2/Vs$, and the electron density in the 2DEG is $n = 3.8 \times 10^{11} cm^{-2}$. Based on the Drude

model in solid state physics[61, 62], $\mu = \frac{e\tau}{m^*}$, $l_{mfp} = v_F \cdot \tau$, $k_F^2 = 2\pi n$, where $\tau$ is the electron relaxation time, $m^* = 0.067m_e$ is the electron effective mass, $v_F$ and $k_F$ are the electron Fermi velocity and Fermi wave-vector. Based on these relations, the electron mean-free-path is calculated to be $l_{mfp} = \frac{\hbar\sqrt{2\pi}}{e}\sqrt{n}\mu = 9\mu m$ for our 2DEG. This mean-free-path is 9 times longer than our longest QPC channel and 90 times longer than our shortest QPC channel. Thus the electron transport in our QPC channel is ballistic. For the case where the mean-free-path is not long compared with the channel length, theoretical calculation shows that not only conductance resonances will show up, but also the plateau will be seriously degraded[14], which is not the case for our system: resonances and well established plateaus coexisting in the conductance curves.

A more direct way to rule out dirt effects is to fabricate symmetric QPCs together with asymmetric QPCs, and using the symmetric ones as a control group. Fig.3.3, Fig.3.5, Fig.3.7 and Fig.3.8 are the conductance curves measured for some symmetric QPCs we have fabricated. As can be seen, comparing with the asymmetric QPCs, symmetric QPCs do not show the conductance resonances and the modulation of quantized plateaus. In fact, more than 15 symmetric QPC samples and more than 30 asymmetric QPC samples(including the eight ones which were studied systematically in Table3.1) were measured at T=4.2K, 3K or 0.3K. The measurement agrees with this argument: all asymmetric QPCs tend to show conductance resonances and the modulation or suppression of plateaus, while all the symmetric QPCs show no (or much fewer) conductance resonances and a reduced (or a lack of) modulation of plateaus. Especially by comparing Fig.3.8 and Fig.3.11, where both the QPCs have a relatively long channel length: 500nm, this direct comparison establishes that impurities are not an issue. The figures show that the symmetric one shows no conductance resonances while the asymmetric one shows heavily dense resonances. Thus if the resonances in asymmetric QPCs were due to the dirt effect, then this

effect should also exist in symmetric QPCs since they are fabricated using exactly the same method and on the same crystal. The fact that few resonances are observed in the symmetric QPCs suggest that the resonances in the asymmetric QPCs can not be due to impurities and thus are intrinsic. This argument also holds if the impurities here are the lithographic imperfections instead of ionized Si dopants. For example, if two bumps were introduced on the gates, forming an 'opened' quantum dot. The Coulomb blockade will give rise to the conductance resonances. This case can also be ruled out by statistically comparing the behaviors of the symmetric QPCs and asymmetric QPCs. In particular, for a short 100nm channel QPC it is nearly impossible, statistically speaking, to create two lithographic bumps within such a short channel length.

To conclude the above discussion, the linear conductance resonances and the modulation of the quantized plateaus observed in asymmetric QPCs are the intrinsic properties of our samples. Then the next question is to ask 'what is the nature of these two features?'

### *3.2.4 Discussion: Electron Correlation Induced Barriers and the Formation of Quasi-bound States in Asymmetric QPCs*

I will start the discussion by introducing a more general conductance formula for QPCs, extending the simple calculations in Chapter 1.2 where the temperature was assumed to be 0K, and the transmission probability was assumed to be unity. Now we consider a more general case that $T \neq 0K$ and transmission probability may not be 1. Looking at Fig.1.3, where f represents the Fermi function: $f_\mu(E,T) = \frac{1}{e^{\frac{E-\mu}{kT}}+1}$. To differentiate the temperature symbol T, $T(E)$ is used to represent the transmission probability of an electron, passing through the QPC channel with energy E. Due to the time reversal symmetry, the $T(E)$ for electrons traveling from the left to the right equals the $T(E)$ for electrons traveling from the right to the left. The current

expression for each populated sub-band can be derived as follow:

$$\begin{aligned} I &= e\int_0^\infty \big[(f_{\mu_R}(E,T) - f_{\mu_L}(E,T)) \cdot n(E) \cdot v(E) \cdot T(E)\big] dE \\ &= \frac{2e}{h}\int_0^\infty \big[f_{\mu_R}(E,T) - f_{\mu_L}(E,T)\big] T(E) dE \end{aligned} \tag{3.1}$$

where n(E) is the electron density of state as a function of energy, v(E) is the electron velocity as a function of energy. n(E) and v(E) cancels to a constant $2e/h$, as discussed in Chapter 1.2. For the linear conductance, $V_{bias} = 0$ and $\mu_R - \mu_L = e \cdot V_{ac}$ is small. Thus the difference between the two Fermi functions in Equation 3.1 can be approximated to be the derivative of Fermi function with respect to the chemical potential $\mu$:

$$\begin{aligned} G &= \frac{I}{V_{ac}} \\ &= \frac{2e^2}{h}\int_0^\infty \frac{f_{\mu_R}(E,T) - f_{\mu_L}(E,T)}{\mu_R - \mu_L} T(E) dE \\ &= \frac{2e^2}{h}\int_0^\infty \frac{\partial f_\mu(E,T)}{\partial \mu} T(E) dE \end{aligned} \tag{3.2}$$

At T=0, $\frac{\partial f}{\partial \mu}$ is a delta function. Thus the linear conductance $G = \frac{2e^2}{h}T(E)$ is proportional to the transmission probability T(E). Setting T(E)=1 gives rise to the quantized plateau. For the ballistic transport with no scattering, T(E) was assumed to be 1 to explain the quantized conductance in QPCs: T(E) is proportional to conductance (G), and the relative energy E is related with the gate voltage ($V_g$), therefore T(E) vs E can be mapped into $G(V_g)$ vs $V_g$, which is measured by experiment. But the real picture is more than this simple, especially with electron correlations included.

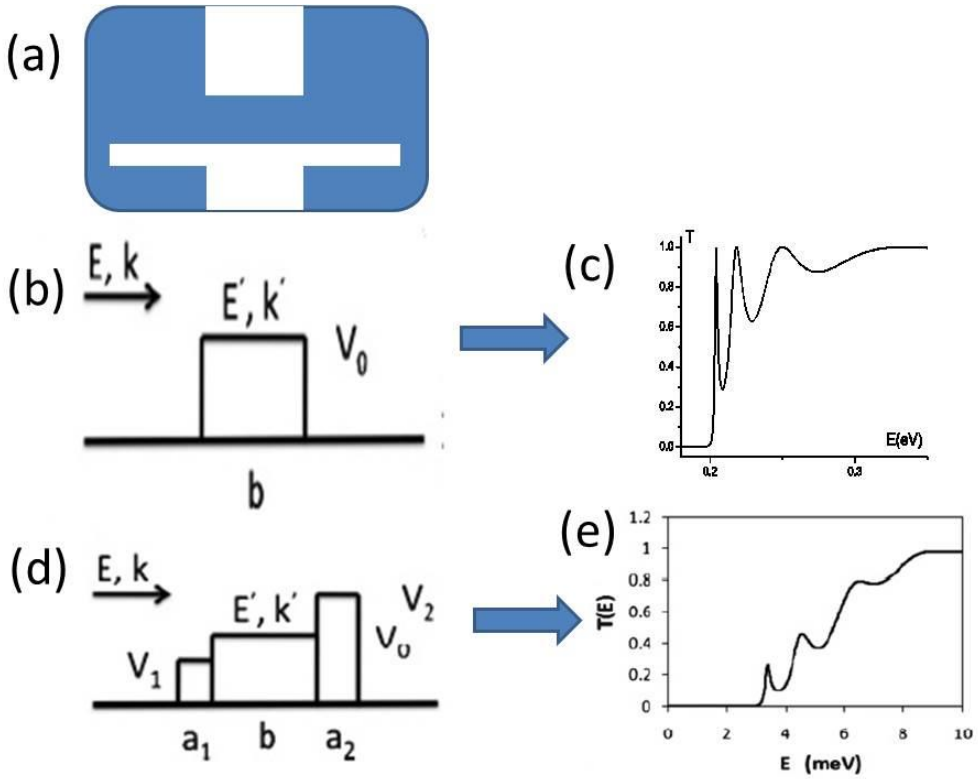


FIGURE 3.14: (a) The schematic of a typical asymmetric QPC. (b) an electron with energy E and momentum k propagates to the right, through a square shape potential barrier. (c) the transmission probability of this electron through the barrier as a function of E. (d) a potential barrier with some asymmetry (e) the transmission probability corresponds with the case in (d). (d) and (e) are taken from ref[43]

We consider a very basic 1D quantum mechanics toy model in the single-particle picture: a square potential barrier shown in Fig.3.14(b). In a very rough approximation, this square shape barrier can be used to mimic the potential profile of a QPC shown in Fig.3.14(a). Inside the QPC channel, due to the confinement of the gates, the electron energy is higher than the energy outside the channel. Therefore, effectively, the electrons will 'feel' a potential barrier when passing through the QPC channel. For a good start, the square barrier in panel (b) is used to study this effect, only because it is simple and can be solved easily and analytically. The electron transmission probability as a function of energy (E) for the case in panel (b) is:

$$T(E) = \frac{4k^2k'^2}{4k^2k'^2cos^2(k'b) + (k^2 + k'^2)^2sin^2(k'b)} \tag{3.3}$$

where $E'$ is the the energy of the barrier, $k = \sqrt{2m^*E}/\hbar$ is the electron wave-vector. $k' = \sqrt{2m^*(E - E')}/\hbar$ is the electron effective wave-vector in the channel. Fig.3.14(c) shows the T(E) vs E relation for the case in panel (b), based on Equation 3.3. As can be seen, transmission resonances show up. These resonances, sometimes also refered as quasi-bound states, are due to the quantum interference of the electron wave function in the channel, in a manner similar to the Fabry-Perot interferometer in optics or the standing wave formation in a resonator. If the 1D potential barrier is not symmetric about the center, e.g. the profile shown in Fig.3.14(d), the calculated resonance peak value can not reach 1, as shown in panel (e) (this analytical calculation was performed by Prof. Albert M. Chang and was shown in ref[43]).

It seems that the conductance resonances, observed in the asymmetric QPCs, can be qualitatively explained within this single-particle picture, by mapping the relations T(E) vs E in panel (c) and (e) into the relations $G(V_g)$ vs $V_g$. Actually just right after the discovery of the quantized conductance in QPCs[12, 13], theory immediately predicted the conductance resonances based on the single-particle calculations[63, 64, 65]. But in the past two decades, few conductance resonance has been observed in QPCs. This is because that, the QPC confinement potential profile created by the split gates, which are located far from the 2DEG, is quite smooth, due to the long range Coulomb interactions. Thus the real potential barrier profile is much more smoother than the cases in Fig.3.14(b)(d). When the potential profile is smooth, the resonances quickly disappear[66]. Therefore the single-particle picture can not give rise to the resonances observed here.

The resonance story will be quite different, if electron-electron interactions are included in the picture. As has been discussed in the beginning of this chapter,

novel (short-range) ordered localized electron states were predicted to be formed in QPCs, as a result of the competition between the quantum nature (e.g. quantum fluctuations) of electrons and the electron-electron interactions. Below I will introduce several numerical calculations reported in the literature, about this new state of matter, obtained using the Spin Density Functional Theory [49, 67] and the Quantum Monte Carlo method[8, 9]. Then I will discuss the possible connections between our experimental observations and these numerical calculations.

Yakimenko *et al* calculated the effective potential profile that an electron will 'see' when it enters the QPC channel, using the Spin Density Functional theory[49]. Part of their result is shown in Fig.3.15(a). Yakimenko *et al* started with a 1D 'smoothed square shape' gate potential profile:

$$V_{confine}(x) = V_0\big[tanh(s(x-x_1)) - tanh(s(x-x_2))\big] \tag{3.4}$$

Where x is the position in the direction aligned with the QPC channel. $x_1$ and $x_2$ defines the positions of the two ends of the QPC channel. The parameters defines the sharpness of the potential profile, created by the QPC gates. Fig3.15(a) shows the modified effective potential profile in the QPC after including the electron correlations. The QPC channel in the figure is between x=100nm and x=300nm. As can be seen, when s is small (e.g. s=0.3), corresponding to a smooth initial potential profile, the effective potential profile turns out also to be smooth. But when s is big (e.g. s=1), corresponding to a relatively sharp initial potential profile, the effective potential profile develops two sharp barriers at the ends of the QPC channel. This potential barriers are due to the electron correlations. Without the electron correlation, the initial potential barrier can not give rise to the resonances. But if the electron correlation is included, the effective potential barriers can be formed, which can further give rise to the quasi-bound states and resonances in experiment.

Still using the Spin Density Functional theory, Akis and Ferry[67] calculated the

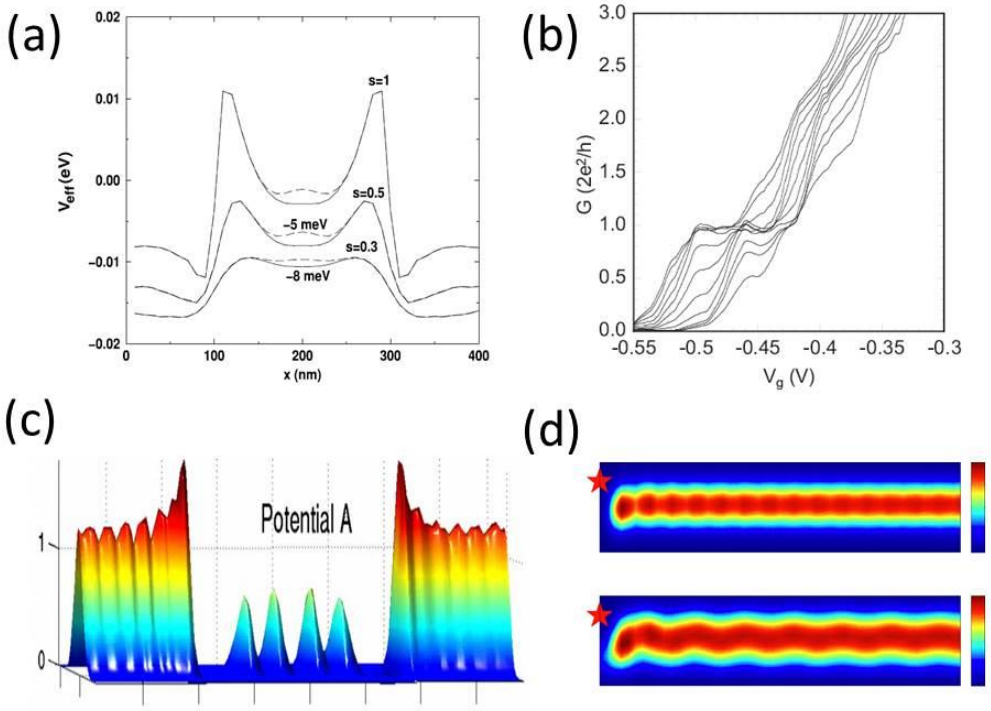


FIGURE 3.15: (a) The effective potential profile inside a QPC channel using Spin Density Functional theory simulation. Figure(a) is taken from ref[49]. (b): The simulation of the linear conductance of a QPC, using the Spin Density Functional theory. Figure(b) is taken from ref[67]. (c): The electron density in the QPC channel using the Quantum Monte Carlo simulation. Figure(c) is taken from ref[8]. (d): the electron pair density inside a QPC channel: linear Wigner crystal to zigzag Wigner crystal quantum phase transition. Figure(d) is taken from ref[9]

linear conductance as a function of gate voltage. The result is shown in Fig.3.15(b). Different curves represent different electron densities. As can be see, with the electron correlation included, small conductance bumps(or resonances) develops, so does the modulation of the quantized plateau by tuning the electron density.

Guclu *et al* calculated the electron density in the QPC channel and the effective potential profile of the QPC, using the Quantum Monte Carlo method[8]. Guclu *et al* predict that if the gate potential is sharp, the electron correlation will give rise to sharp potential barriers at the ends of the QPC channel which will further

localize the electrons inside the channel, forming an ordered electron states (Wigner crystal)[8]. Fig.3.15(c) shows the calculated electron density where a Wigner crystal state forms. By performing the Quantum Monte Carlo numerical calculation, Mehta *et al* show that the quantum Wigner crystal state will go through a quantum phase transition from a linear crystal state into a zigzag state, with an increasing electron density[9]. This Wigner crystal zigzag phase transition is shown in Fig.3.15(d): the upper one is the electron density for a linear electron Wigner crystal while the lower one is for the zigzag case.

Besides the Spin Density Functional theory and the Quantum Monte Carlo method, Song and Ahn investigated the interacting electron system in QPCs, using the exact diagnalization method. They showed that even when the gate potential profile is relatively smooth, localized electron states can still be formed in the QPC channel due to electron correlations[55]. These localized states (or quasi-bound states) can give rise to the ferro-magnetic coupling, in a manner similar to the Hund's rule. The possible formation of localized ferromagnetic electron states, predicted by Song and Ahn, will be discussed later, which might be related with some signatures in the differential conductance of our asymmetric QPCs.

Now with the above theoretical calculations in mind, we can start to interpret the two features observed in the linear conductance of our asymmetric QPCs. As I have discussed above, the linear conductance resonances can not be due to impurity. And single-particle picture can not give rise to the conductance resonances either. Thus we ascribe the conductance resonances to the electron correlation effect. Theory shows that, starting with a sharp initial potential confinement profile, electron correlation can induce potential barriers in the QPC channel[49, 67, 8, 9]. (Keep in mind that this sharp initial potential profile itself can not give rise to the conductance resonances in the single-particle picture.) This electron-correlation-induced barriers can cause electrons bouncing forth and back in the channel, and forming quasi-bound states

(or localized states), which give rises to the conductance resonances in experiment. With many-body physics picture, we can explain the QPC channel length dependance for the number of resonances shown in Fig.3.13: once the two electron correlation barriers are formed at the entrance and exit of the QPC channels, the criteria to form a quasi-bound state is similar to the criteria for a standing wave in a 1D cavity:

$$N \cdot \frac{\lambda_F}{2} = l \tag{3.5}$$

where N is an integer number, $l$ is the channel length, and $\lambda_F = \frac{2\pi}{k'}$ is the effective Fermi wavelength in the channel. When the gate voltage is tuned less negative, the channel width starts to open up, resulting in a decreasing of energy for each sub-band, or an increasing of the effective electron Fermi energy ($E'$ and $k'$) in the channel. This increase of $k'$ leads to a decrease of $\lambda_F$. Once Equation 3.5 is satisfied for an integer N, a quasi-bound (or localized state) is formed. When the channel length $l$ gets longer, more integer values N can be fit into Equation 3.5, thus more quasi-bound states can be formed, resulting in more conductance resonances observed for longer channels.

The reason that these conductance resonances are not generally observed by other groups, is probably due to the criteria of the formation of electron-correlation-induced barriers, which requires a sharp gate confining potential profile. We think the gate confining potential profile in our system is sharper than other groups based on the fact that the distance between the gates and the 2DEG is shorter than other groups'. For example, the 2DEG in our crystal is buried only 85nm below the surface, comparing to 277nm in Ref[16] and 300nm in Ref[50]. Actually, the calculation in Fig.3.15(b) is done based on a theoretical QPC model with parameters very similar to our case. For example, the 2DEG depth is 70nm in the model comparing with 85nm in our case, also the size of the gates is very similar with our QPCs. As can be seen in Fig.3.15(b), the calculation shows both the conductance resonances and

the suppression of the quantized plateau, which is consistent with our observations. Actually, in an asymmetric QPC defined by surface oxidation, which should also yield a sharp potential profile, similar reproducible resonance features were observed by Senz *et al*[68]. But they did not focus on this resonance feature in the paper.

Closer distance between the gates and the 2DEG in our system gives sharper potential profile, resulting in electron-correlation barriers. Therefore, in principle, the symmetric QPCs should also show electron-correlation barriers and conductance resonances. The reason that this is not generally observed in our symmetric QPCs, is probably because that the asymmetric gate geometry results in a sharper potential profile than the symmetric QPCs. But this speculation needs theoretical calculations to prove. On the other hand, the symmetric QPCs showing almost no conductance resonances helps us to rule out impurity effects, which is probably even more important in the current situation.

Besides the resonances, a possible explanation for the suppression of the quantized plateau might be related with the zigzag quantum phase transition. The suppression of the quantized plateau was first discovered by Pepper's group: Hew *et al*[50, 51, 52] and Smith *et al*[53, 54]. The connection between this suppression and double row Wigner crystal formation was also first proposed by them: when a double row crystal state is formed, the propagating channel suddenly becomes two, resulting in the conductance of $2 \times 2e^2/h$. In experiment, the conductance will jump directly from 0 to the second quantized plateau. How the double row Wigner crystal is related to the zigzag Wigner crystal remains an unsolved question. As I have discussed previously, our QPC system (strong confinement) has a quite different potential profile than Pepper's group (weak confinement). Therefore, whether the modulation of quantized plateau observed in our system is related with theirs, is still an open question.

## 3.3 the Differential Conductance of Asymmetric QPCs

After systematically characterizing the linear conductance behavior of 8 asymmetric QPCs, we now switch into the study of the differential conductance. It turns out that the differential conductance for short channel QPCs (100nm, and 300nm channel length) have different characteristics compared with the long channel QPCs (500nm channel length or longer). I will present the study of short channel QPCs first, and then switch into the more complicated behaviors in the long channel QPCs.

Fig.3.16(a) shows the $dI/dV$ for one typical short channel asymmetric QPC. The lithographic channel length is 300nm. Below is how the $dI/dV$ measurement was set up: during the entire measurement, the wall voltage was held fixed ($V_{wall} = -1.51V$), while $V_{finger}$ is held fixed at different voltages for different colored curves. Thus each colored trace in Fig.3.16 is measured by fixing both $V_{wall}$ and $V_{finger}$, with sweeping the bias voltage $V_{sd}$.. Assigning different curves different colors is just to better differentiate the curves. As can be seen in Fig.3.16(a), even with the colors, the curves are still too dense. Thus a subset of the curves in panel (a) were extracted and then presented in panel (b). For the rest of this thesis, all the our $dI/dV$ data will be presented in this way: a series of $dI/dV$ traces as a function of $V_{sd}$, the traces have the same fixed $V_{wall}$ but different fixed $V_{finger}$(denoted by different colors). Throughout this thesis, every $dI/dV$ trace was measured by sweeping the $V_{sd}$ forward (from negative to positive) and backward (from positive to negative) at different sweeping speeds. The forward and backward sweeping $dI/dV$ traces are consistent with each other.

Fig.3.16(c) shows the linear conductance correlated with Fig.3.16(a)(b). In panel (a) the $dI/dV$ values at zero bias (the center) is actually the linear conductance. This linear conductance was extracted from panel (a), by performing a 'center cut' of (a), and then was re-plotted as a function of $V_{finger}$, shown in Fig.3.16(c) as

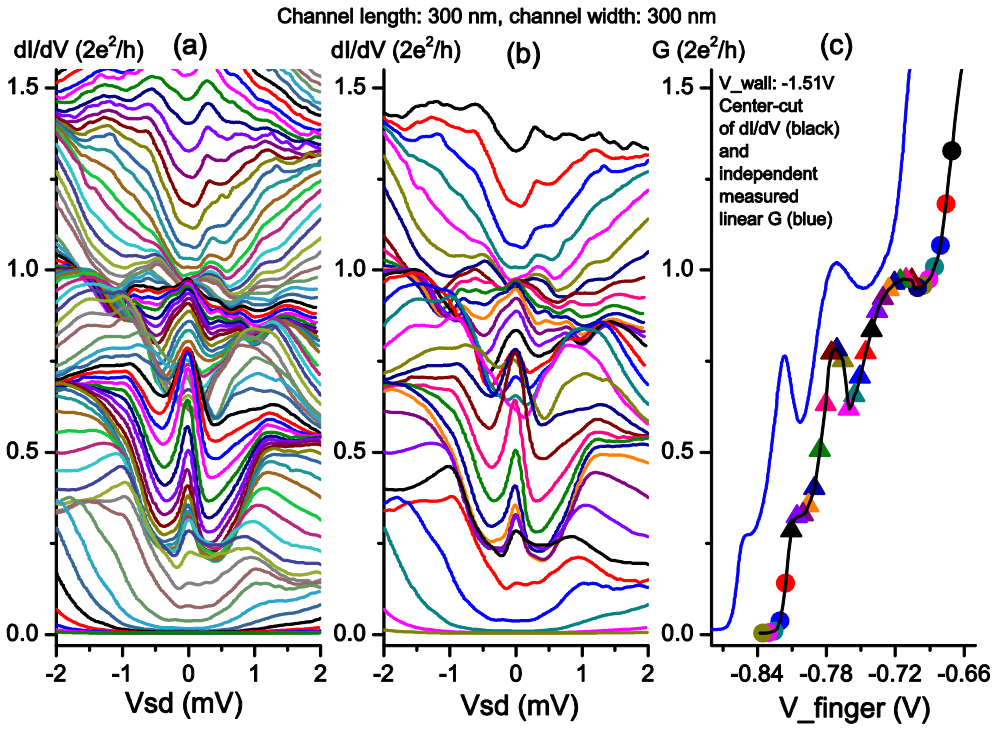


FIGURE 3.16: (a) The differential conductance as a function of $V_{bias}$, for a typical short channel length asymmetric QPC (300nm channel length, 300nm channel width). The $V_{wall}$ was held fixed at -1.51V, during the entire measurement. Different $dI/dV$ traces, measured at different fixed $V_{finger}$s, were assigned with different colors for clarity. In total, 74 $dI/dV$ traces are shown here. To see these traces more clearly, 34 $dI/dV$ traces were taken from (a) and then shown in (b). (c) linear conductance of the same sample, as a function of $V_{finger}$. The black curve is the 'center (zero bias) cut' of (a) plotted as a function of $V_{finger}$, the colored dots are the 'center cut' of (b). The blue curve is borrowed from Fig.3.10 which is the linear conductance measured independently to compare with the 'center cut', which is laterally shifted for clarity. The triangular shape dots in (c) correspond with the curves in (b) with ZBAs, while the circular shape dots correspond with the curves with no (or very weak) ZBA. T=300mK.

the curve. While the 'center cut' of (b), which has fewer data points, are shown in panel (c) as the dots. The colored dots in panel(c) correspond with the zero bias value of the curves in panel (b) with the same color, which makes it easier to correlate the structure in $dI/dV$ with the structure in linear conductance, such as the resonances. Recall that the linear conductance is also measured systematically and independently for the 8 asymmetric QPCs. Thus the linear conductance for this asymmetric QPC with the same $V_{wall}$ can be extracted from the independent linear conductance measurement (Fig.3.10). This linear trace is shown in Fig.3.16(c) as the blue curve, with a lateral shift for clarity. As can be seen, the linear conductance obtained from the 'center cut' of $dI/dV$ traces agrees with the linear conductance independently measured at the same gate voltages. This consistency shows that the system is stable for gating, since after the measurement of the blue curve, the gate voltages were tuned over a large gate parameter range, and then were tuned back to measure the $dI/dV$, from which the black curve was obtained.

As can be seen in Fig.3.16(a)(b), a differential conductance peak near zero bias is observed. This so-called zero-bias-anomaly (ZBA) in QPC system was first observed by Cronenwett *et al* [19], while its origin is still controversial[15]. In Fig.3.16(b), as the QPC channel opens up from the bottom to the top, the ZBA starts to show up (or becomes strong) for the black curves ($\sim 0.25 \times 2e^2/h$). Then this ZBA structure is observed all the way from this black curve to the curves near the first quantized plateau ($2e^2/h$). The triangular shaped dots in Fig.3.16(c) correspond the $dI/dV$ curves with a ZBA, while the circular dots correspond with those curves with no(or much weaker) ZBA. As can be seen, the ZBA is present over a wide range, corresponding with a wide range in the linear conductance. For those curves corresponding to the second resonance valley in the linear conductance, such as the pink one, the ZBA peak magnitude is much weaker

All the $dI/dV$ data shown in this chapter were measured at T=300mk. Here we

measured the $dI/dV$ curves for the eight asymmetric QPCs shown in Table 3.1 (or Fig.3.13(c)). For each QPC sample, based on its linear conductance characteristics (part of them shown in Fig.3.9 to Fig.3.12), a particular $V_{wall}$ was chosen, and was then held fixed for the $dI/dV$ measurement. One such $dI/dV$ data set is shown in Fig.3.16. In total 10 data sets were measured for the 8 asymmetric QPCs (for one QPC, three data sets, corresponding with 3 different $V_{wall}$s, were measured).

Fig.3.16 represents the typical behavior of the ZBA in the differential conductance (dI/dV) of the short channel asymmetric QPCs: the ZBA exist over a wide range below the first quantized plateau, which is consistent with other groups' work[19, 15]. As will be shown in the next section, the ZBA behavior for the differential conductance of the longer channel asymmetric QPCs is quite different, which can be correlated with the successive linear conductance resonances.

### *3.3.1 Even-Odd Effect of the Zero Bias Anomaly*

Fig.3.17 shows the typical $dI/dV$ characteristics for an asymmetric long channel QPC. The channel length for this sample is 500nm and the channel width is 250nm. For clarity, only a subset of the whole $dI/dV$ traces for this sample were presented in Fig.3.17(a). The solid lines represent the $dI/dV$ traces with ZBAs, while the dotted line represent the ones with no ZBAs. The black curve in Fig.3.17(b) is the 'center cut' of the whole $dI/dV$ traces (including those not shown), while the dots in panel (b) are the 'center cut' of the $dI/dV$ traces shown in panel (a). The triangular shape dots represent the $dI/dV$ traces with ZBAs, while the circular dots for no those without a ZBA. The blue curve is the linear conductance measured independently to show consistency with the 'center cut'.

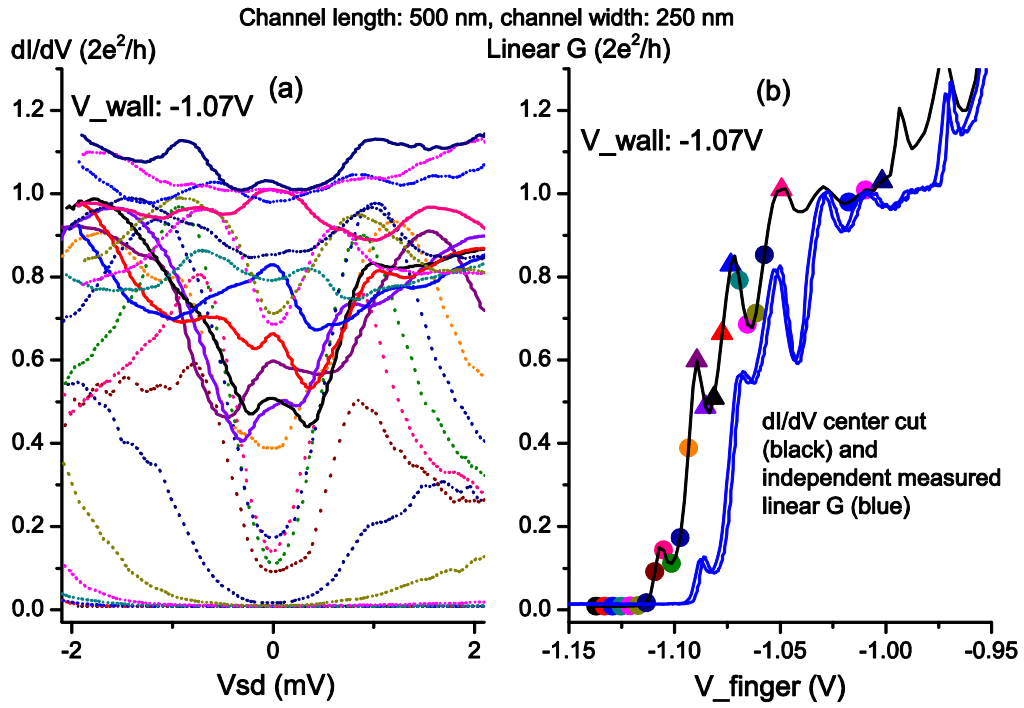


FIGURE 3.17: (a) The differential conductance as a function of $V_{bias}$, for a typical long channel length asymmetric QPC (500nm channel length, 250nm channel width). The $V_{wall}$ was held fixed at -1.07V. Different colored $dI/dV$ traces were measured at different fixed $V_{finger}$s. In total, 67 $dI/dV$ traces were measured while only 25 traces are presented here for clarity. (b): the linear conductance of the same QPC, as a function of $V_{finger}$. The black curve is the 'center (zero bias) cut' of (a) (including the $dI/dV$ traces that are not shown in (a)), but plotted as a function of $V_{finger}$, the colored dots are the 'center cut' of (a) (the traces that are shown in (a)). The blue curve is borrowed from the independence linear conductance measurement, laterally shifted for clarity. The circular dots in (b) correspond with the $dI/dV$ (dotted lines) curves without ZBAs in (a), while the triangular shape dots in (b) correspond with the $dI/dV$ (solid lines) curves with ZBAs in (a). T=300mK.

As can be seen in Fig.3.17(b), the second linear conductance valley is filled with 'triangular dots', meaning that all the $dI/dV$ traces, corresponding to this valley, show ZBAs. The two neighboring valleys of this valley are filled with 'circular dots', meaning that none of the $dI/dV$ curves, corresponding to these two valleys, shows the ZBA structure. The appearance of the ZBA in $dI/dV$ for every other linear

conductance resonances is called the even-odd effect of ZBA. This near even-odd effect is generally observed in our long asymmetric QPCs. The near even-odd effect observed in our long channel QPCs, does not strictly follow the even-odd rule. In some cases it can be even-odd-odd or even-even-odd rule, which will be explained later.

### *3.3.2 Even-Odd Effect Discussion: Kondo-like Physics*

The near even-odd effects of ZBA are reminiscent of the Kondo effect in semiconductor quantum dots[1, 20, 69, 70]. Though I have mentioned Kondo effect very briefly in Chapter 1, here I will introduce more about Kondo effect in quantum dots for better understanding of our data.

The Kondo effect was first discovered in 1930s. It was found that the resistance of some non-magnetic metal, but doped with some magnetic impurities (such as Mn atoms) , increases with a decreasing temperature, if the temperature is below a critical temperature $T_K$. This behavior was counter-intuitive, when it was first discovered, since usually decreasing temperature decreases the lattice vibrations(phonon number), which further decreases the electron scattering caused by these phonons. Therefore the resistance is expected to decrease with a decreasing temperature, which is generally observed. But metals doped with magnetic impurities show this opposite resistance vs temperature relation. Jun Kondo first addressed this issue by performing a third-order perturbation theory[71]. It turns out that the increase of the resistance is due to the extra scattering of electron by the magnetic impurities (localized spins or magnetic moments). Later on, Phillip Anderson provided a simplified theoretical model, known as the Anderson impurity model[72]. This Anderson model is based on the interaction between a localized spin magnetic moment, which mimics the doped magnetic atoms, and the electron Fermi sea, which represents the free electrons in the metal. In the late 1980s, the progress in semi-

conductor nanofabrication allowed people to be able to make artificial atoms, or quantum dots[73], which is a system that can almost be exactly described by the Anderson model. The realization of quantum dots revives this old field. Kastner's group first reported the Kondo effects observed in quantum dots[1]. The results is shown in Fig.3.18. All the figures in Fig.3.18 are taken from Ref[1, 70].

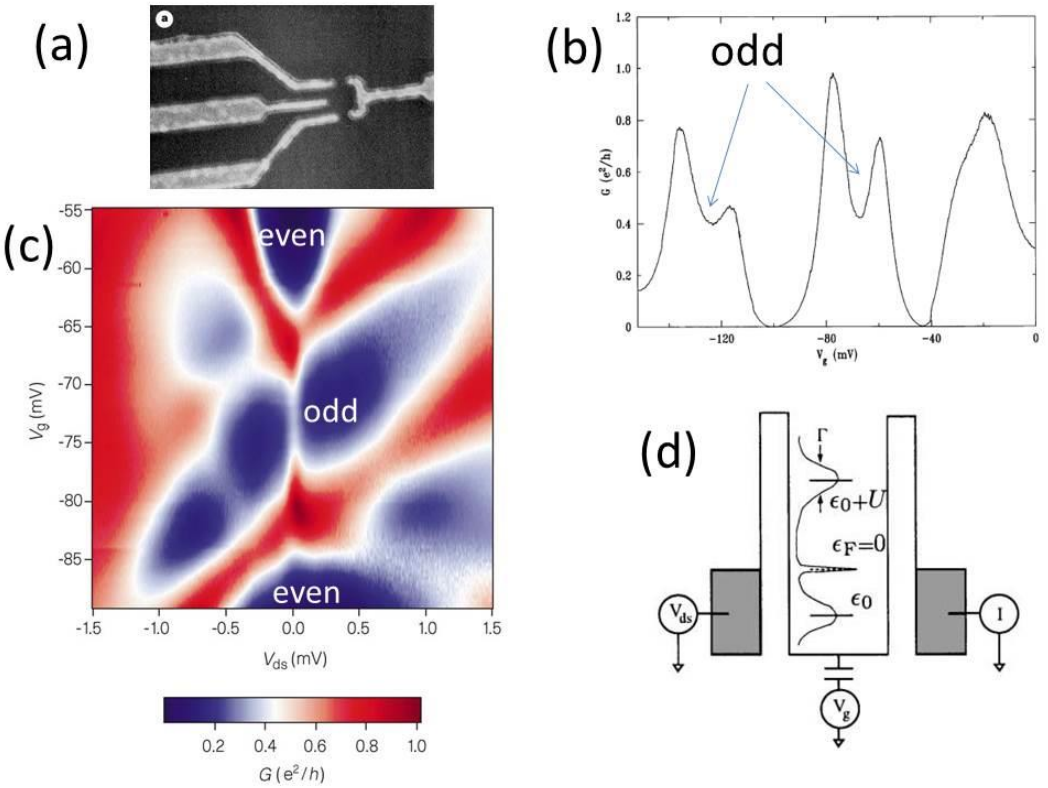


FIGURE 3.18: The Kondo effect in Quantum Dots. (a) SEM image of the gate geometry for a quantum dot. (b) Linear conductance of the quantum dot as a function of the plunger gate voltage. (c) Differential conductance of the quantum dot as a function of the plunger gate voltage (y) and source-drain bias voltage (x). (d) Electron density of states inside the quantum dot. (a)(c) are taken from ref[1], (b)(d) are taken from ref[70]

A quantum dot is an electron system, where electrons are confined in all the three spacial directions, resulting in quantized electron energy levels. Fig.3.18(a) shows the scanning electron microscope image of the gate geometry of a quantum dot, fabricated on the top of GaAs/AlGaAs crystal. Negative gate voltages were

applied to the four gates, as a result, electrons in the 2DEG, underneath the gates, were depleted by the gates, creating a quantum dot, with the dot shape defined by the gates. The right gate and the left two side gates are tuned to control the opening (coupling) of the quantum dot to the two Fermi seas, while the left middle gate, named the plunger gate, is used to tune the chemical potential inside the quantum dot. Fig.3.18(b) shows the linear conductance of this quantum dot as a function of plunger gate voltage, by connecting the two Fermi seas to the source and the drain. The small size of the quantum dot gives a small capacitance, C. Thus adding an additional electron causes a measurable energy ($\Delta E = e^2/C$). The elctron energy levels inside the dot will be separated by this charging energy and also the quantized energy level spacing due to the confinement. As a result, the linear conductance as a function of gate voltage shows peaked structures (as shown in Fig.3.18(b)), known as the Coulomb blockade. The Coulomb blockade can be understand in the following way: since the energy levels inside the dot are discrete, when the Fermi level of the Fermi seas is in between the two energy levels of the dot, there will be no state in the dot with energy aligned with the Fermi energy of the Fermi sea. Thus the electrons in the Fermi seas can not pass through the dot, and the current is blocked. If the plunger gate is tuned so that one energy level in the dot is aligned with the Fermi level of the Fermi seas, then electrons in one Fermi sea can transport into the other Fermi sea though the aligned level in the dot, where an increase in current will be observed.

The successive separation between peaks in Fig.3.18(b) shows wide-narrow-wide behavior, which is due to the even and odd filling number on the dot. I labeled the valleys which correspond with odd filling numbers in the dot. As can be seen, the odd valleys are narrower than the neighboring even valleys. Because for an odd number of electrons in the dot, adding another electron will occupy the same state with an opposite spin, for which the energy cost is only the Coulomb charging energy. As for

the even filling number valley, the cost for adding an extra electron on the dot is the charging energy plus the quantized level energy spacing, since the extra electron will occupy the next empty state in the dot. This wide-narrow-wide behavior is based on an ideal model of quantum dots with a constant Coulomb interaction, which is often violated due to the exchange and other interactions.

Fig.3.18(c) shows the $dI/dV$ as a function of the bias voltage and the plunger gate voltage. The 'center cut' of (c) at zero bias reconstruct the linear conductance in panel (b). Based on the linear conductance peaks, each valley can be assigned with a filling number either even or odd. As can be seen in panel (c), in the odd valley with a fixed plunger voltage, there is a zero bias peak (ZBP) (if you do a horizontal cut in the odd valley). This ZBP is represented by the white line in the center of the odd valley, which is one signature of the Kondo effect in quantum dots. This ZBP can be explained qualitatively as the following: based on the Anderson impurity model, when the electron filling number is odd, the net spin in the quantum dot is non zero, resulting in a localized spin (magnetic) impurity. The interaction between this localized magnetic moment with the Fermi sea will enhance the tunneling probability through the dots, resulting in a resonance in the density of state right at the chemical potential of the Fermi sea leads. In terms of experiment, a ZBP will be observed in the $dI/dV$ curve of an odd filling quantum dot. The coupling between the localized spin and the Fermi seas is anti-ferromagnetic, resulting in a formation of spin-singlet state between the localized electron and the non-localized Fermi sea, which is a many-body spin effect. For the even filling number, the net spin (magnetic moment) is zero, thus no Kondo tunneling process can happen, resulting in a $dI/dV$ curve with no ZBP.

This ZBP for odd filling number and no ZBP for even filling number behavior of quantum dot is similar with the near even-odd rule for ZBA observed in our longer channel QPCs. The first question regarding this similarity may be that how is our

QPCs, an open system, related to the Kondo effect in quantum dots, which is an almost closed system, since the Kondo effect requires a localized magnetic impurity. The answer is based on our argument on the origins of the linear conductance resonance in Chapter 3.2.4, where electron correlations in our asymmetric QPCs can give rise to potential barriers which help to confine and localize the electrons. Therefore adding an extra electron, to those electron-correlation-induced quasi-bound states in QPCs, will give rise to a linear conductance resonance. Thus when the electron filling number in these quasi-bound states is odd, a quasi-localized magnetic moment, due to the non-zero total spin, will give rise to the Kondo-like ZBA as shown in Fig.3.17. While the neighboring valleys, which have even electron filling number, have zero magnetic moment and show no Kondo-like ZBA. Thus for our asymmetric QPCs, which is an open system, with the electron-correlation-induced potential barriers included, the near even-odd rule can be qualitatively understood.

The reason we did not observe strict even-odd rule but near even-odd behavior is because that, after all, the asymmetric QPC system is not exactly a confined system like quantum dots, even with the correlation-induced barriers. For example, near the pinch off threshold, the tunneling probability from the Fermi sea into the QPC channel is so small, that the Kondo energy scale gets exponentially suppressed, rendering the ZBA unobservable. Near the first quantized plateau, which is almost an open system, it is even meaningless to define the filling number for the quasi-bound states.

This near even-odd effect is generally observed in our long channel asymmetric QPCs, but for the short channel QPCs, as shown in Fig.3.16, this picture does not hold, and the ZBA seems to exist everywhere. This suggests that the ZBA in the short channel asymmetric QPCs may be related to different physics comparing to the long channel ones.

Particularly, in one long asymmetric QPC, a triple-peak structure was observed

in $dI/dV$, with a filling number even, suggesting a formation of spin-triplet, instead of singlet.

### *3.3.3 the Triple-peak Structure: Possible Spin-1 Kondo Effects*

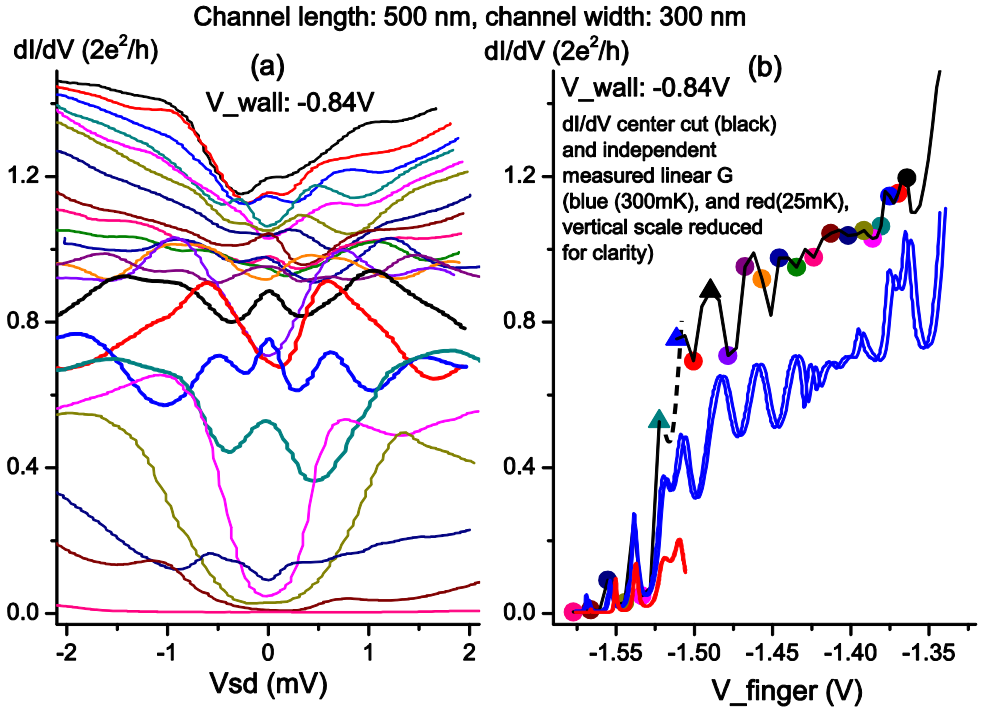


FIGURE 3.19: (a) The differential conductance as a function of $V_{bias}$, for a long channel length asymmetric QPC (500nm channel length, 300nm channel width). The $V_{wall}$ was held fixed at -0.84V, during the entire measurement. Different $dI/dV$ traces , measured at different fixed $V_{finger}$s, were assigned with different colors for clarity. In total, 44 $dI/dV$ traces were measured while only 23 traces are presented here for clarity. (b): linear conductance of the same sample, as a function of $V_{finger}$. The black curve is the 'center (zero bias) cut' of (a) (including the $dI/dV$ traces that are not shown in (a)), but plotted as a function of $V_{finger}$.The colored dots are the 'center cut' of (a). The blue curve is borrowed from the independence linear conductance measurement(Fig.3.11), while the red curve was measured in measured at 25mK with the same $V_{wall}$, in a different cool down. The vertical scales for the blue and red curve are shrinked by a factor of 1.5 and 4, respectively, for clarity. T=300mK besides the red curve.

Fig.3.19(b) shows the $dI/dV$ for this long channel asymmetric QPC with a chan-

nel length 500nm and channel width 300nm. Panel (b) shows the corresponding linear conductance. The black curve and the colored dots represent the 'center cut' in panel (a). The blue curve is the linear conductance, measured independently (extracted from Fig.3.11) with the same $V_{wall}$, while the red curve is also the linear conductance measured with the same $V_{wall}$, but in a different cool down and at a lower temperature T=25mK. The blue curves and the red curves have their vertical scale shrinked by a factor of 1.5 and 4, respectively, for clarity. Thus the conductance resonances can be better compared between the $dI/dV$ center cut and linear conductance traces measured independently. As can be seen, they show consistency between each other in terms of the resonances. The dashed curve connecting the two broken black curves in panel (b) represents a missing data point, and was drawn by comparing it with the blue and red curves.

Fig.3.19(a) shows a blue $dI/dV$ curve with a triple-peak structure, corresponding with the blue triangular dot in panel (b). This triple-peak structure is the feature we want to address here. Following the black linear curve in panel (b), the cyan triangular dot (at $\sim 0.55 \times 2e^2/h$) corresponds with the $dI/dV$ trace with a ZBA in panel (a), suggesting the valley that this cyan dot is sitting to be odd filling. Going past the peak in the linear conductance, we should enter the even filling number regime, which is the case for the red circular dot, corresponding with a $dI/dV$ trace with no ZBA as shown in panel (a). But the other dot (blue triangular shape) corresponds to an $dI/dV$ curve with three peaks near zero bias. Going further across the linear conductance peak again, a black triangular dot, corresponding to the curve with a ZBA, suggests entering into the odd filling regime again, which is what expected.

Now the question is whether the triangular blue dot belongs to the odd filling valley (cyan dot) or the even filling valley (the red dot). If it belonged to the odd valley, it should give rise to single zero bias peak like the cyan dot, which does not

agree with the triple-peak structure. One may think of the side peaks to be evolved from the big shoulders in the cyan $dI/dV$ curve. But beside the triple-peak structure, the blue curve has its own big shoulders near $V_{sd} = \pm 1.5mV$. Therefore, the only possible case for the triple-peak structure is to think of it as the filling number is even.

How can an even number of electron system, with a total spin usually equals to 0, gives rise to the triple-peak structure? It could be explained as the following: the two electron spins in the QPC channel form a triplet state instead of a singlet state. This quasi-localized triplet state (with spin=1) will give rise to a quasi-localized non-zero magnetic moment, which can couple to the 2DEG Fermi sea through a Kondo-like interaction process. Thus the partial Kondo-like screening of this triplet state, by the Fermi seas, can give rise to a zero-bias peak in $dI/dV$. The two side peaks can be interpreted as the excitation from the triplet ground state to the singlet excited state. Therefore, this triple-peak structure can be qualitatively understood in this spin-1 Kondo-like picture.

The next question is to ask why the ground state here is a triplet state instead of a singlet state. This may be due to the competition between two energy scales as discussed below. Consider two electrons, quasi-localized in the QPC channel, due to the electron correlation induced barriers. When the two electrons form a spin singlet, they can occupy the same lowest quasi-bound state. When the two electrons form a spin triplet, due to the Pauli exclusion principle, one electron can occupy the lowest quasi-bound state, while the other can only occupy the second lowest quasi-bound state or other higher energy states. Thus comparing with the spin singlet case, the triplet state will have an extra energy term which equals to the level spacing between the lowest two quasi-bound states ($\Delta E$). However, the Coulomb interaction between the two electrons in the singlet state will be larger than in the triplet state, since the two electrons in the singlet state have the same spatial wave function and more

overlap between the wave functions. This extra energy in the singlet state is due to the Coulomb interaction, and sometimes refered as the exchange energy $E_{exchange}$. Tuning the $V_{finger}$ tunes the potential profile and the quasi-bound states. $\Delta E$ and $E_{exchange}$ are also tuned indirectly. If the $E_{exchange}$ is tuned to be higher than $\Delta E$, then the triplet state will be the ground state and spin-1 Kondo-like process may happen, resulting in a triple-peak structure in $dI/dV$.

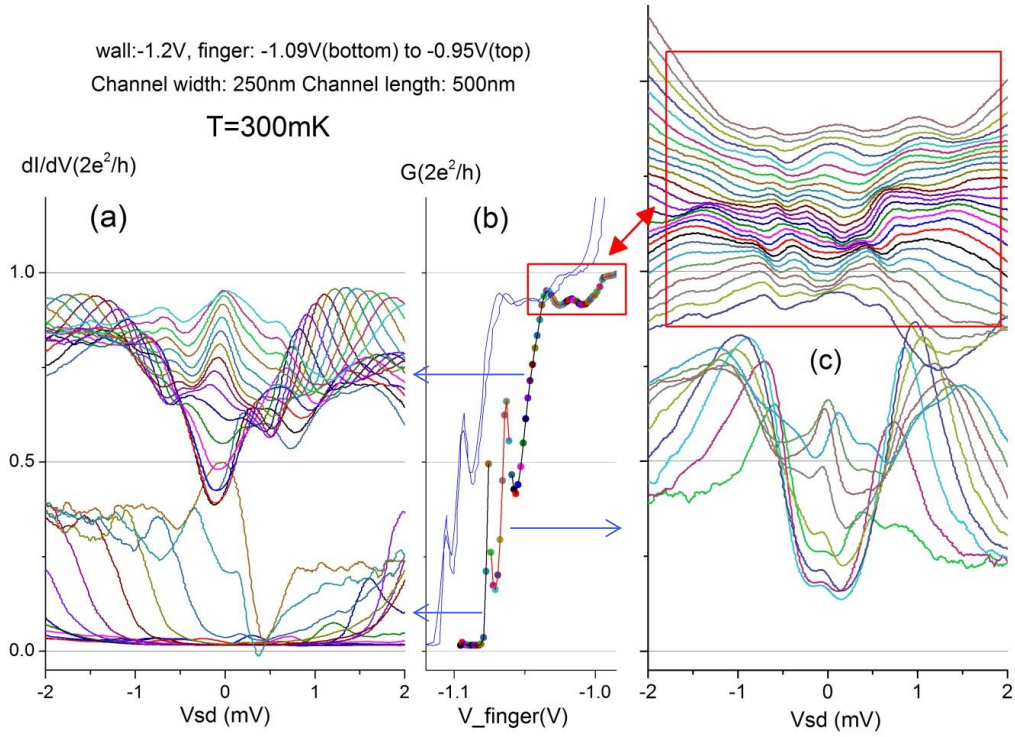


FIGURE 3.20: (a)(c): The differential conductance as a function of $V_{bias}$, for a long channel length asymmetric QPC (500nm channel length, 250nm channel width). The $V_{wall}$ was held fixed at -1.2V, during the entire measurement. Different $dI/dV$ traces , measured at different fixed $V_{finger}$s, were assigned with different colors for clarity. The traces are shown in (a) and (c) separately for clarity. (b): The blue curve is the independent measurement of the linear conductance as a function of $V_{finger}$ with the same $V_{wall}$. The colored dots are the center cut of (a) and (c) at zero bias. The dI/dV traces corresponding with the dots in the red box in (b) are shown in the red box in (c) but with vertical offset, for clarity. T=300mK

Fig.3.20 shows another set of data which supports the even-odd and triple-peak picture. The asymmetric QPC is the same with Fig.3.17, but was measured under a

different fixed $V_{wall}$ and also in a different cool down. Panel (a) and (c) are the dI/dV traces plotted separately for clarity. The center cut of panel (a) and (c) near zero bias were plotted in panel (b). As can be seen, all the dots in the first valley in panel (b) corresponds with dI/dV traces with a ZBA as shown in panel (c). Going across the linear conductance peaks, the dots on the two neighboring sides of the valley in panel (b) corresponds with dI/dV traces with no ZBA as shown in panel (a). This ZBA and no-ZBA behavior is consistent with the even-odd rule shown in Fig.3.17. In Panel (a), going from $0.4 \times 2e^2/h$ all the way up to $2e^2/h$ near zero bias, the no-ZBA traces smoothly develop into the dI/dV traces with a triple-peak structure. This no-ZBA to triple-peak transition is consistent with the triplet formation discussion in Fig.3.19. Besides the even-odd and triple peak behavior, the dI/dV traces (with vertical offset for clarity) enclosed by the red box in panel (c) show small dI/dV oscillations. These small dI/dV oscillations were systematically studied in another sample which will be discussed in detail in the next chapter.

Using the numerical diagnalization calculation technique, Song and Ahn studies the electron system in QPCs[55]. Besides the electron-correlation-induced-localized-electron-states formed in the QPC channel, their calculation also predicts possible ferro-magnetic coupling between electrons and the formation of high spin states, in a manner similar with the Hund's rule. Therefore this numerical calculation, to some extent, is consistent with our observation of triple-peak structure.

The triplet spin-1 Kondo effect has been studied systematically in semiconductor quantum dots[74, 75] and $C_{60}$ molecular quantum dots[76], but not been observed in QPCs yet.

The channel length dependence of the QPC linear conductance resonances, and the modulation of quantized plateaus, together with the near even-odd effect and triple-peak structure in differential conductance, have been published in Ref[44]. Interestingly, almost at the same time, Iqbal *et al* published in a paper in Nature[77],

showing experimental evidence for the formation of electron localized states in symmetric QPCs. They further showed the differential conductance data for the ZBA and no ZBA cases, for which they ascribed to the even and odd Kondo effect. Their result, in a sense, is consistent with our observation here. In the supplemental material of their paper, they also mentioned the possible triple-peak structure observed in their system and cited our work.

# 4

# Electron Correlation Effects in Asymmetric QPCs: Novel Differential Conductance Oscillations

In this chapter I will describe a new type of behavior observed in asymmetric QPCs: small differential conductance ($dI/dV$) oscillations as a function of source-drain bias. This novel feature shows a very unusual magnetic field dependence: the $dI/dV$ oscillations get significantly suppressed in a small in-plane magnetic field ($\sim 0.7T$). The oscillations are also washed out at a temperature $\sim 800mK$. I will focus on the systematic study of the $dI/dV$ oscillations for one asymmetric QPC (with 100nm channel length, and 250nm channel width). Thus all the data shown in this chapter is based on this sample. I will characterize these oscillations with different gate voltages, in-plane magnetic fields, temperatures and cool downs. As will be shown in the discussion, the whole characteristics of this $dI/dV$ oscillation cannot be explained by any simple single particle. In the end, I will conclude this chapter by ascribing this feature to the electron and spin correlation based on the fact that the oscillations are very sensitive to a small in-plane magnetic field.

There have been signs that these oscillations are also present in several other asymmetric QPCs. But since those QPCs have a longer channel length, and more

linear conductance resonances, it will be difficult to tell whether the features, observed in those samples, are related with this novel unknown $dI/dV$ oscillation, or with the linear conductance resonances. Thus all the data shown in this chapter is from the one short channel asymmetric QPC.

The systematic measurement of these $dI/dV$ oscillations were performed twice. First in a He3 fridge with a base temperature 300mK. Then the sample was moved into a dilution refrigerator with a base temperature less than 30mK. The two cool-downs show consistent characteristics for these $dI/dV$ oscillations. Thus the oscillations and their characteristics are thermal cycling reproducible. I will present the data, obtained from both the cool-downs, in the first few figures, to show this reproducibility. Then I will focus on the data measured in the dilution refrigerator.

I start by presenting the linear conductance of this sample, and its evolution with an in-plane magnetic field.

## 4.1 Linear Conductance

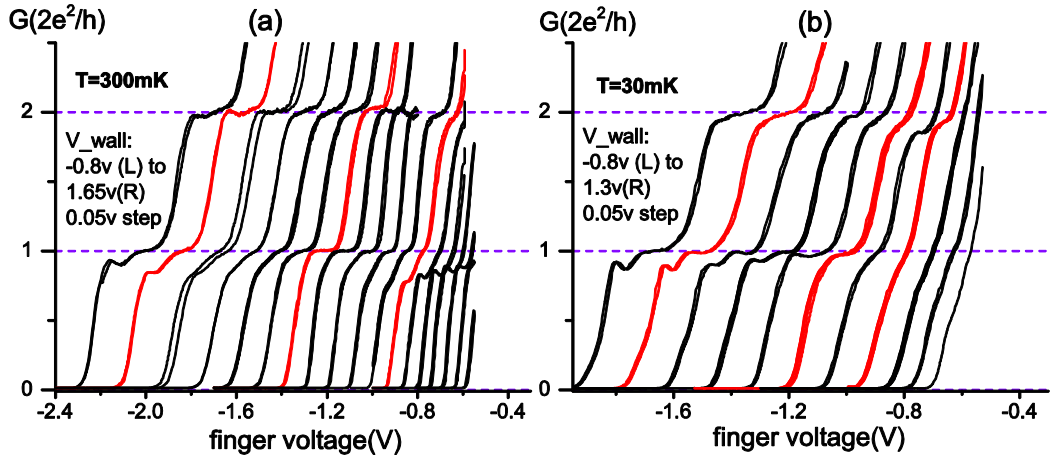


FIGURE 4.1: The linear conductance of the asymmetric QPC in (a) the He3 fridge and (b) the dilution refrigerator. Different conductance traces correspond to different fixed $V_{wall}$ as denoted in the figure. The three red curves in (a) correspond to $V_{wall}$ equals to -0.85V, -1.1V and -1.35V, from left to right, respectively. While the three red curves in (b) correspond to $V_{wall}$ equals to -0.85V, -1.05V and -1.15V, respectively.

Figure4.1(a) and (b) show the linear conductance of this asymmetric QPC measured in the two fridges respectively. Different curves correspond with different fixed $V_{wall}$ as labeled in the figure. The two features in the linear conductance discussed in Chapter 3 are also observed here: the modulation of the quantized conductance plateau and the conductance resonances. In panel (a), going from left to right, the first quantized conductance plateau becomes weaker at $V_{wall} = -0.9V$, then strengthened at $V_{wall} = -1.1V$, and weaker again at $V_{wall} = -1.35V$. These three typical curves are labeled as red to show this weak-strong-weak plateau modulation. In panel (b) the three typical red curves, with $V_{wall} = -0.85V, -0.9V$ and $-1.05V$, also show this weak-strong-weak plateau modulation. Few conductance resonances were observed here, since this sample has the shortest channel length (100nm). Thus this is not against the argument about the linear conductance resonances in Chapter 3. Panel (a) and (b) show a conductance bump below the first quantized plateau, which is reminiscent of the '0.7' effect. But the magnetic field dependence of this bump, shown in Fig.4.2, suggests a very different characteristic.

Fig.4.2 shows the behavior of these linear conductance traces when an in-plane magnetic field was applied. The magnetic field direction was aligned with the 2DEG plane (in-plane). The reason that a magnetic field perpendicular to the 2DEG was not preferred is due to the fact that a perpendicular magnetic field will bend the electron trajectory in the 2DEG, due to the Lorenz force. This bending can affect the conductance and give rise to the Quantum Hall Effect[17, 2]. On the contrary, an in-plane magnetic field will not affect the electron trajectory, since the Lorenz force in this case is perpendicular to the 2DEG, and the electrons are confined in the 2DEG. Thus the trajectory cannot be bended by the Lorenz force. This makes an in-plane magnetic field mainly 'talks' with the electron spins though the Zeeman coupling, which can help us to investigate the possible spin correlation effects. The linear conductance curves, measured under different magnetic fields, are labeled as different

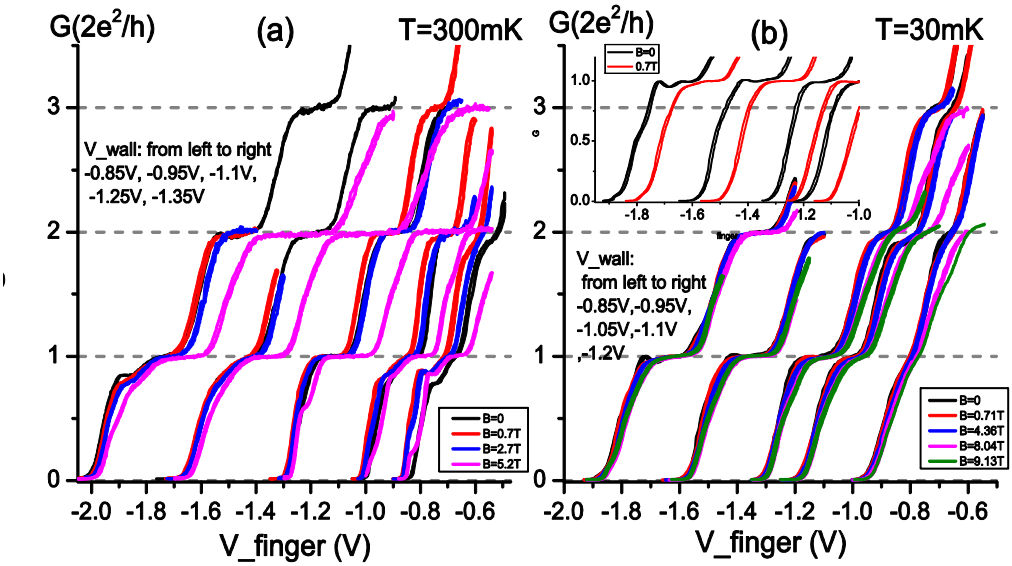


FIGURE 4.2: The linear conductance of the asymmetric QPC under different in-plane magnetic fields for the two different cool downs. Different fields are represented by different colors as shown in the figure. The $V_{wall}$ for different traces are labeled in the figure. The inset in (b) shows the data for B=0T and B=0.7T from (b), with a lateral shift for clarity.

colors as shown in the figure. In panel (a), The left most curve ($V_{wall} = -0.85V$) and the two rightmost ones ($V_{wall} = -1.25V$ and $-1.35V$), show a conductance bump near $0.7 \times 2e^2/h$ at B=0T. When the magnetic field is increased to B=5.2T (the pink curves), these three curves show two bumps below $2e^2/h$. This magnetic field characteristics is quite different from the well known '0.7' effect[16, 19], where the '0.7' bump develops smoothly to the $0.5 \times 2e^2/h$ plateau, with an increasing in-plane magnetic field. This difference of the magnetic field dependence suggests that the conductance bump in panel (a), may have a different origin from the well known '0.7' bump.

Panel (b), measured at a lower temperature $\sim 30mK$, shows even more interesting characteristic. As can be seen, no half plateau is observed in the curves, for an in-plane magnetic field as high as 9T, represented by the green curves. While in Ref[16, 19], the half plateau is well established at B=4T and B=3T, due to the

Zeeman coupling and the lift of the sub-band degeneracy. This suggests that the effective g factor in our system is much smaller, resulting the Zeeman splitting $\Delta E = g\mu_B B$ unresolvable even at B=9T.

The inset in panel (b) shows the B=0T and B=0.7T data, extracted from panel (b), with a lateral shifted for clarity. As can be seen, for the left most curve($V_{wall} = -0.85V$), the bump structure at B=0T disappears when B is increased to 0.7T. This big modification of the conductance bump under a small in-plane magnetic field is completely unexpected, and will be discussed later.

## 4.2 Differential Conductance

Based on the strength of the quantized plateau shown in Fig.4.1, the three typical linear traces in Fig.4.1(a) or (b), labeled as red, can be considered to represent the three (weak-strong-weak plateau) regions. For each red trace, the differential conductance was measured by fixing $V_{wall}$ at the same value with the red linear trace. Thus in total, 6 $dI/dV$ data sets were measured corresponding with the 6 red linear curves in Fig.4.1. They all show similar behaviors (including the magnetic field and temperature dependence that will be discussed later). Thus I will only present the typical $dI/dV$ data set below.

Fig.4.3(a) shows a typical $dI/dV$ data set as a function of bias ($V_{sd}$), at T=30mK. As can be seen, unusual small $dI/dV$ oscillations, which have never been observed in QPCs before, are developed. Some oscillations are highlighted by enclosing them within a dashed red box. We will focus on the systematic study of these $dI/dV$ oscillations in the rest of this chapter.

The measurement set-up for Fig.4.3(a) is the same with the $dI/dV$ measurement described in Chapter 3. The $V_{wall}$ was held fixed at a value (-0.85V) same with the $V_{wall}$ of the leftmost red curve in Fig.4.1(b). Before describing Fig.4.3(b), one needs to point out that for each $dI/dV$ trace, $V_{sd}$ was swept back(faster) and forth(slower)

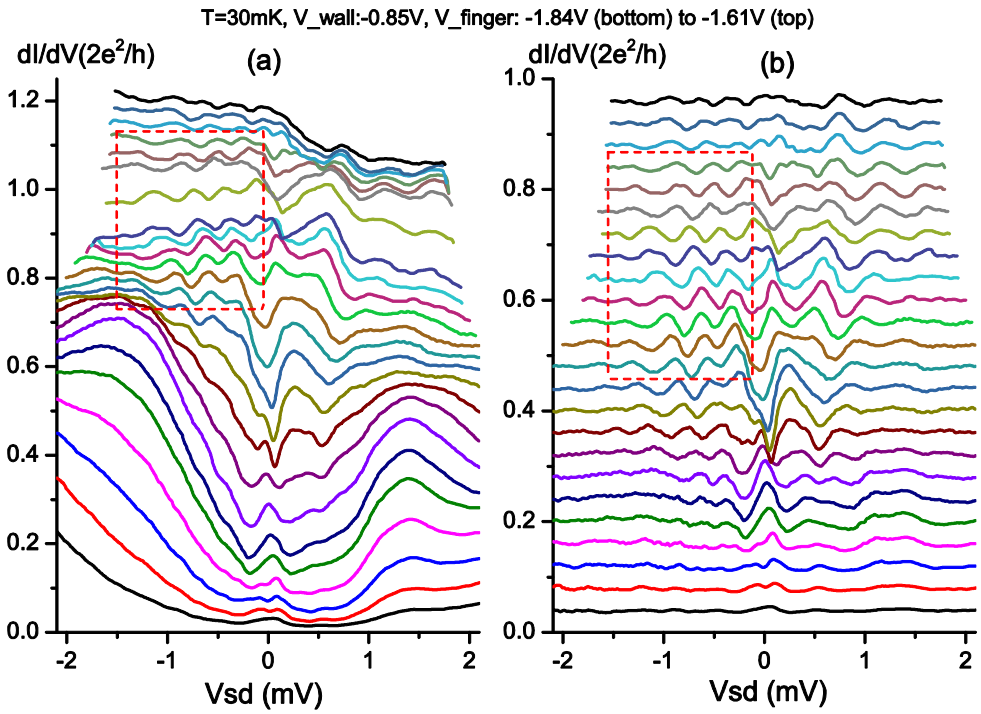


FIGURE 4.3: $dI/dV$ for $V_{wall} = -0.85V$ at 30mK. Different colored curves represent different fixed $V_{finger}$. The $V_{finger}$ is -1.84V for the bottom black curve, and -1.61V for the top black one. (a) is the raw $dI/dV$ data while (b) is obtained by subtracting (a) from its smoothed background, with a vertical offset for clarity. The details of this process is shown in Fig.4.4

between $-2mV$ and $2mV$. The $dI/dV$ data, obtained from the back and forth sweeping, show consistency between each other. The Inset in Fig.4.4 (a) shows the back (the black curve) and forth (the red curve) sweeping for one typical curve to show reproducibility, with a vertical offset for clarity.

To see these oscillations more clearly, the $dI/dV$ curves were first smoothed over a relatively wide $V_{sd}$ range to average out the small oscillations. For example, in Fig.4.4(b), the blue curve, taken from Fig.4.4(a) was smoothed, giving rise to the green one. The green curve in panel (b), after smoothing, shows little oscillations. Then the smoothed green curve, used as a background, was subtracted from the original blue curve, giving rise to the black curve (the subtracted curve) in Fig.4.4(b),

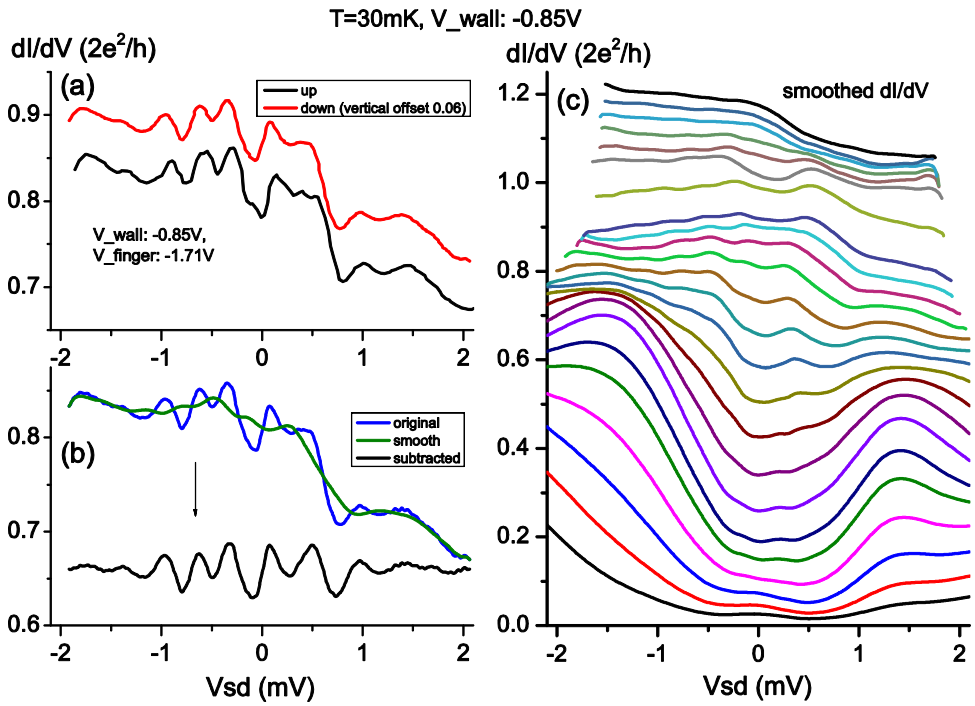


FIGURE 4.4: (a) the back and forth sweeping of $V_{sd}$ for the QPC with $V_{wall} = -0.85V$ and $V_{finger} = -1.71V$, with a vertical offset for clarity. (b) the blue curve is taken from the curve in (a), the green curve is obtained by smoothing the blue curve to smooth out the oscillation structure. The black curve is obtained by subtracting the green curve from the blue one. (c) represents the smoothed $dI/dV$ curves from Fig.4.3(a).

which mainly contains the structure of the oscillations. This process was performed for all the $dI/dV$ curves. Fig.4.4(c) is the smoothed $dI/dV$ curves, obtained by smoothing Fig.4.3(a). As can be seen, there are little (or much weaker) oscillations after smoothing. Then, subtracting this smoothed background (Fig.4.4(c)) from the original traces (Fig.4.3(a)), we obtain Fig.4.3(b), with a vertical offset between different curves, which makes it easier to track and study the oscillations. The smoothing over different ranges of $V_{sd}$ will render different backgrounds and subtracted curves. For example, the size of the oscillation after subtraction will be different if the smoothing is performed over different $V_{sd}$ ranges. The smoothing process is normalized in a way such that all the smoothing is based on the averaging over the

same $V_{sd}$ range.

Fig.4.5 shows another typical $dI/dV$ data set, corresponding with the right most linear curve in Fig.4.1(a), measured in the He3 fridge at T=300mK. Panel (a) is the raw data while panel (b) was obtained by subtracting the smoothed background from panel (a). Only one third of the traces were shown here for clarity.

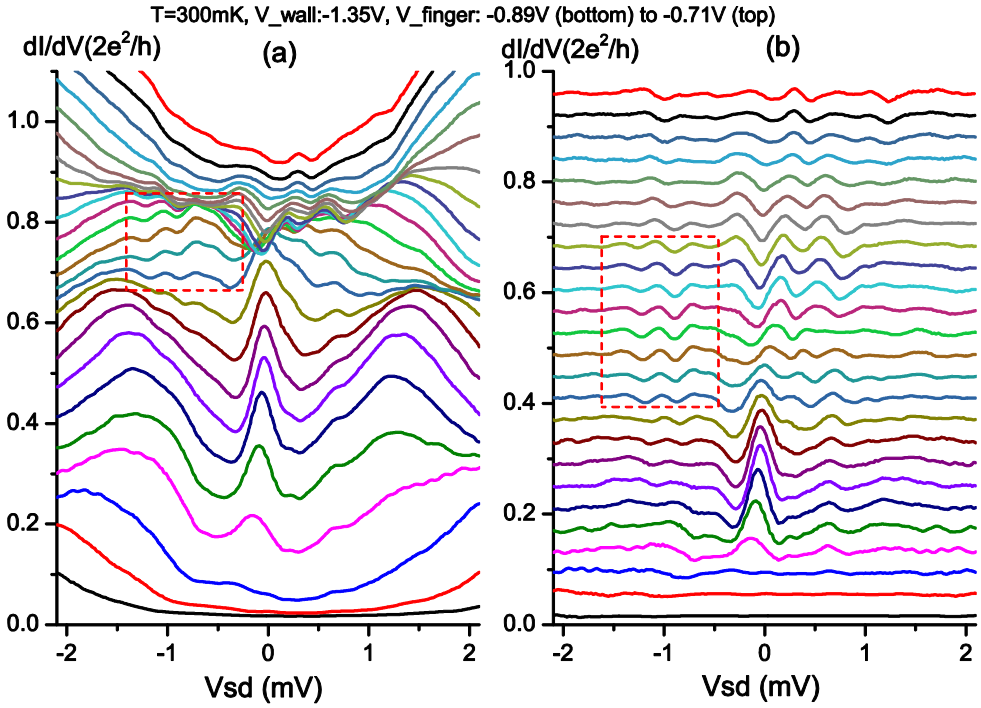


FIGURE 4.5: $dI/dV$ for $V_{wall} = -1.35V$ at T=300mK. The $V_{finger}$ is -0.89V for the bottom black curve, and -0.71V for the top red one. (a) is the raw $dI/dV$ data while (b) was obtained by subtracting (a) from its smoothed background, with a vertical offset for clarity. In total, 25 out of 75 curves are shown here. This $dI/dV$ data set corresponds with the right most red curve in Fig.4.1(a).

As can be seen in Fig.4.3 and Fig.4.5, a typical $dI/dV$ curve has around $5 \sim 7$ major small oscillations. A typical oscillation amplitude at $T = 30mK$ is around $0.04 \times 2e^2/h$. At T=300mK, the oscillation size is roughly halved, by comparing the oscillations in the red box in Fig.4.5(b) with those in Fig.4.3(b). The separation between the neighbor oscillations, at $T = 30mK$, is around $330\mu V$ in terms of $V_{sd}$.

A similar separation is found at $T = 300mK$.

### *4.2.1 Temperature Dependence*

Fig.4.3 and Fig.4.5 show these $dI/dV$ oscillations measured at two different temperatures $30mK$ and $300mK$, but in two different cool-downs. To study the temperature evolution of these oscillations, it is better to measure these oscillations at different temperatures within the same cool down. Thus after obtaining Fig.4.3 at T=30mK, the temperature was heated up to 450mK, and then 800mK, to perform the same measurement.

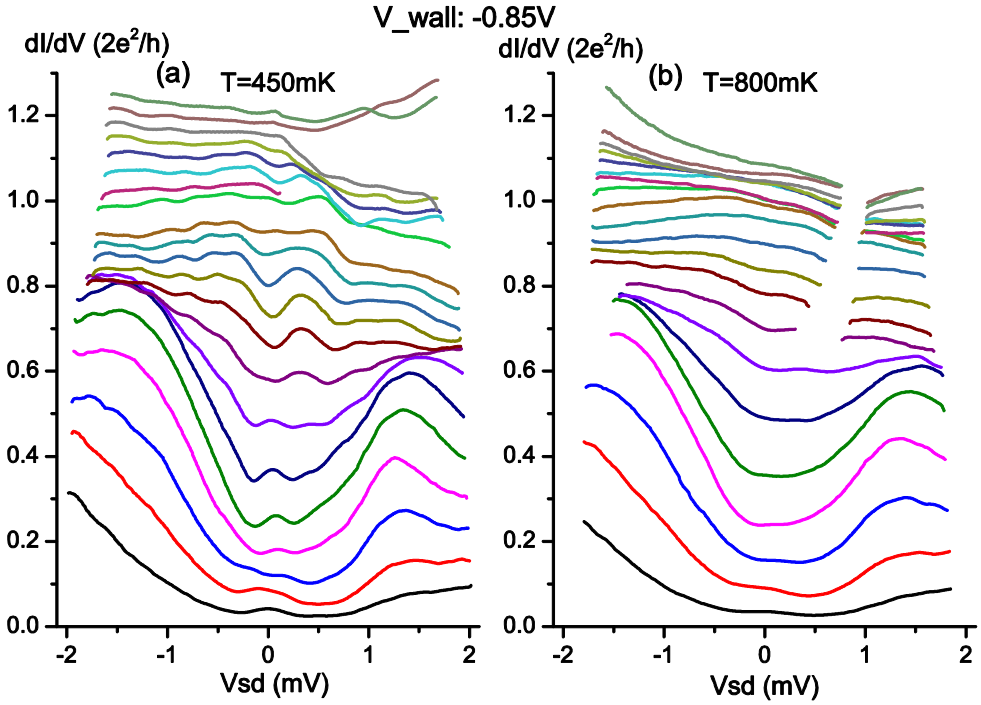


FIGURE 4.6: $dI/dV$ at (a) T=450mK and (b) T=800mK, with fixed $V_{wall} = -0.85V$. $V_{finger}$ is -1.9V for the bottom curve and -1.64V for the top curve in (a), while in (b) $V_{finger}$ is -1.9V (bottom) and -1.6V (top), respectively. The missing points in (b) are due to the malfunction of the equipment

Fig.4.6 shows the $dI/dV$ behavior at 450mK (a) and 800mK (b), for which the base temperature data (T=30mK) is shown in Fig.4.3. The $V_{wall}$ was fixed at a

value same with the left most red trace in Fig.4.3(b). As can be seen, the oscillations become smaller at higher temperature and are almost washed out at T=800mK.

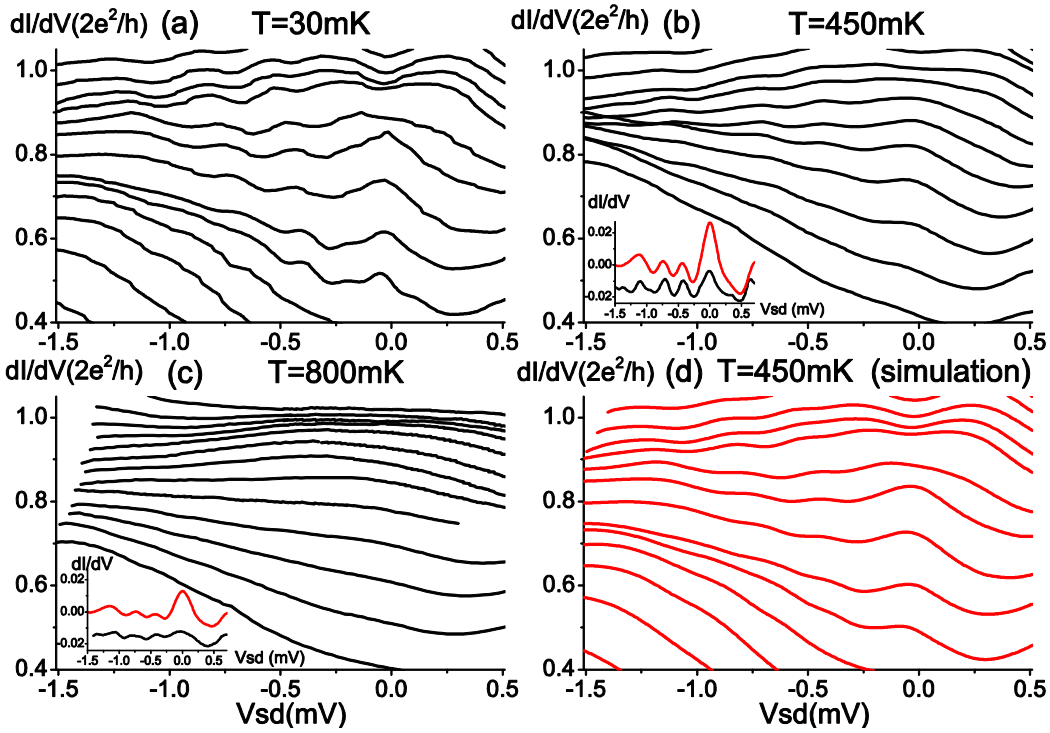


FIGURE 4.7: Temperature evolution of these small $dI/dV$ oscillations. T=30 mK, 450 mK, 800 mK for (a)(b)(c) respectively. (d) is the numerical simulation for T=450 mK. Inset in (b)(c): one typical $dI/dV$ (black) and numerical(red) curve after subtracting the smoothed background for T=450 mK(b) and T=800 mK(d).

Fig.4.7(a)(b)(c) show the temperature evolution for another $dI/dV$ data set corresponding with the middle red curve in Fig.4.3. $V_{wall}$ in panel (a) was held fixed at $-1.05V$, while at higher temperatures(450 mK (b),800 mK (c)), due to the drift, and by comparing the linear conductance traces, $V_{wall}$ was fixed at $-1.10V$ for the case in panel (b) and panel (c).

Fig.4.7(d) shows the numerical simulation of the $dI/dV$ for T=450mK. As can be seen, the simulated oscillation size qualitatively agrees with the real data in panel (b). This simulation is done in the following way. Following the analysis in Chapter 1.2 and Chapter 3.1.4, since the short QPC channel( $\sim 100nm$) is coupled to the two

Fermi sea reservoirs, the QPC transport will be dominated by the Fermi statistics of these two reservoirs. Thus the conductance will be the integral of the product of electron transmission probability ($T(E)$), derivative of Fermi-Dirac function ($\frac{\partial f}{\partial E}$), density of states and the velocity as a function of energy, for both left and right Fermi sea reservoirs. The expression for the differential conductance was obtained and shown in the following equation:

$$\frac{dI}{dV} = \frac{2e^2}{h} \int_{-\infty}^{\infty} \left[\alpha \frac{\partial f(E-\mu_L,kT)}{\partial E} + \beta \frac{\partial f(E-\mu_R,kT)}{\partial E}\right] T(E)dE \tag{4.1}$$

where $\mu_L$ and $\mu_R$ are the quasi-Fermi level for the left and right reservoir, $\alpha$ and $\beta$ represent the portions of bias distributed between the left and right reservoir respectively. Thus $\alpha + \beta = 1$. During the measurement, one reservoir is virtually grounded, leading to $\alpha = 1, \beta = 0$. The simulation shown in Fig.4.7 is based on this assumption. At $T = 30mK$, the width of the derivative of Fermi-Dirac function, $3.5kT \approx 9\mu eV$, is much smaller than the width of the small oscillations ($\sim 330\mu V$), thus to the first order approximation, the $dI/dV$ curves at $T = 30mK$ can be treated as if it was at $T = 0K$. At $T = 0K$, the derivative of the Fermi-Dirac function in Equation 1 becomes a delta function, and

$$\frac{dI}{dV} = \frac{2e^2}{h} \left[\alpha T(\mu_L) + \beta T(\mu_R)\right] \tag{4.2}$$

thus $T(E)$ can be extracted, once $\alpha$ and $\beta$ are assigned. Using the $dI/dV$ curves at $T = 30mK$ as an input to extract $T(E)$, the high temperature evolution can be simulated by plugging in $T(E)$ in Equation 4.1. One typical simulation for $T = 450mK$, using Fig.5(a) as an input, is shown in Fig.5(d) by assuming $\alpha = 1, \beta = 0$. As can be seen, the oscillation sizes qualitatively agree with the measured $dI/dV$ at the same temperature (Fig.4.7(b)). The simulation for $T = 800mK$ (not shown here) also qualitatively agrees with Fig.5(c). Besides this $dI/dV$ data set, the simulation for other sets of $dI/dV$ curves, with the wall voltage corresponding to the leftmost and

rightmost red curves in Fig. 1(d), show consistency with the measured $dI/dV$ oscillations at $T = 450mK, 800mK$. Besides the assumption $\alpha = 1, \beta = 0$, simulations based on $\alpha = 0.9, \beta = 0.1$ and $\alpha = 0.7, \beta = 0.3$ were also implemented and show similar results compared with the $\alpha = 1, \beta = 0$ case.

To better compare the measured oscillations with the simulation for the same temperature, the inset in Fig.4.7(b) shows the $dI/dV$ after subtracting the smoothed background, for one typical trace taken from panel (b) and (d). This smoothing-and-subtracting method is the same with Fig.4.4. The black curve corresponds to one typical curve in panel (b) (real data) while the red curve corresponds to one typical curve in panel (d) (simulation data at the same temperature). The inset in panel (c) is same with the inset in panel (b) except that the temperature here is 800mK. By comparing the real data (black) and the corresponding simulated ones (red) at T=450mK and 800mK in the inset of panel (b)(c), one can see that the oscillation sizes qualitatively agree with the simulation results for the oscillations off zero bias. But the structure near zero bias does not agree with, and is obviously smaller than, the simulation results. This match (or mismatch) for off (or near) zero-bias oscillations is generally observed in all the three $dI/dV$ data sets, using all the simulation parameters (different $\alpha$ values), for both T=450mK and T=800mK. This different behaviors between zero-bias and off zero-bias suggests that the structures at different bias regions may have different energy scales and thus are related to different physics, e.g. the Kondo physics.

Fig.4.8 shows the statistics for the average oscillation size of all $dI/dV$ curves measured at different temperatures. This statistics gives a general trend of how the oscillation sizes decreases as an increase of temperatures. As can be seen, the oscillations are almost washed out at $T = 800mK$. The corresponding thermal energy scales, are $2.6\mu eV$, $39\mu eV$, and $69\mu eV$, respectively. The average oscillation size is calculated as the following.

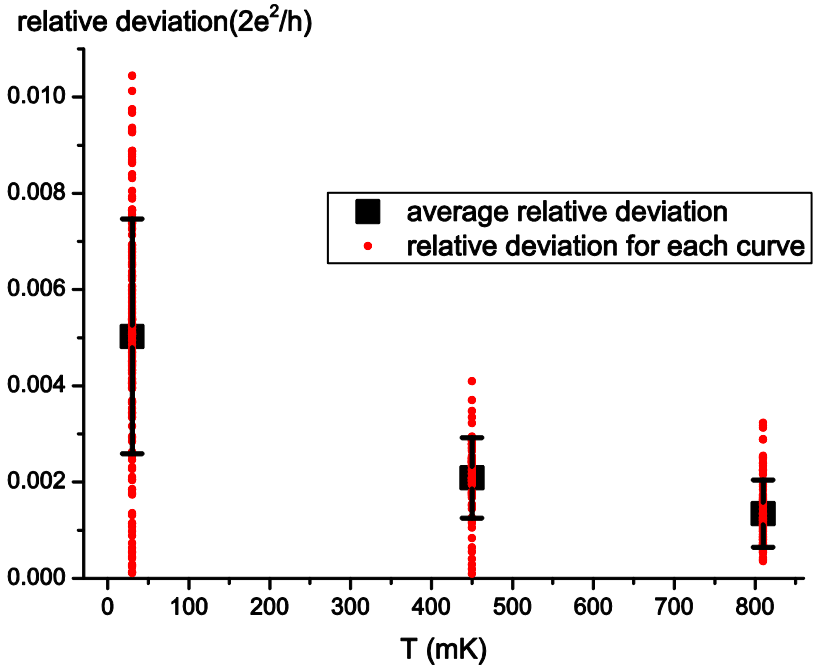


FIGURE 4.8: Statistics for the average oscillation amplitude for different gate voltages at different temperatures.

Taking the blue curve in Fig.4.4(b) as an example, after subtracting the smoothed background (green), the average oscillation size was estimated by calculating the average absolute value for all data points of this subtracted curve (the black curve). This average oscillation size for this particular $dI/dV$ curve is plotted in Fig.4.8 as a red dot with its temperature used as the x value. Thus at each temperature, taking 30mK as an example, the total number of red dots represents the total number of $dI/dV$ curves with different fixed $V_{wall}$ and $V_{finger}$. The black dot in Fig.4.8 represents the mean value of all the red dots at this temperature, also with an error bar. The reason that some curves (red dots) have very small average oscillation size at 30mK, is due to the fact that the oscillation itself is small for those $dI/dV$ curves particularly near the QPC pinch-off threshold. Another method for calculating the average oscillation size, based on the root-mean-square, instead of the average abso-

lute value, was also implemented, and shows similar trends.

### *4.2.2 Magnetic Field Dependence: Low Field*

Now we turn into the study of how these $dI/dV$ oscillations develop when an in-plane magnetic field is applied. We first study the low field behavior, and then switch to the high field case.

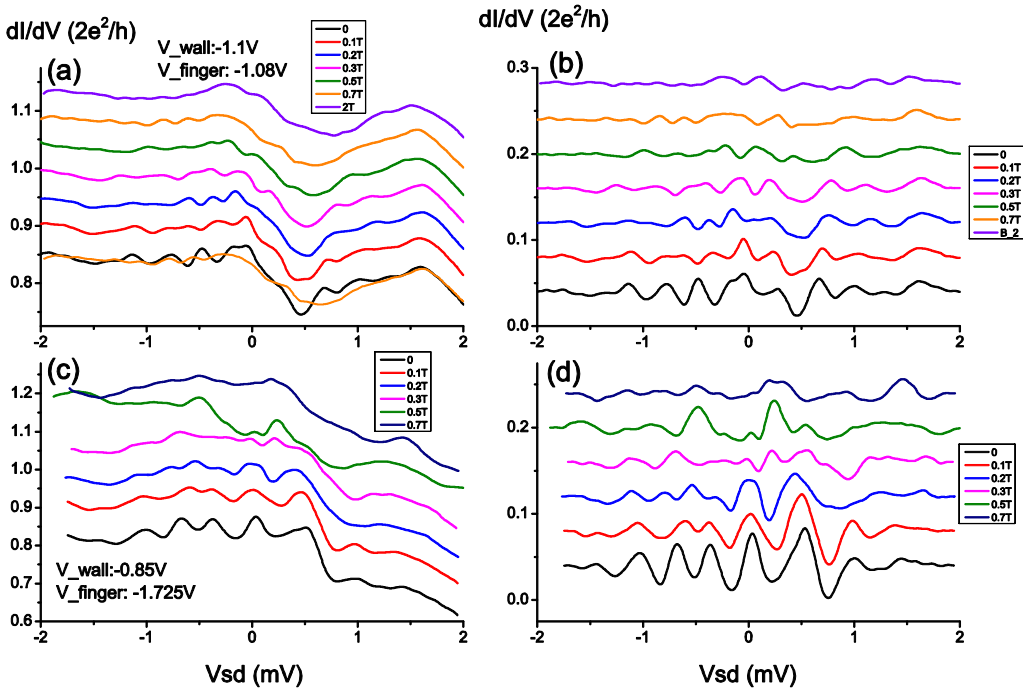


FIGURE 4.9: (a) The in-plane magnetic field dependance for a typical $dI/dV$ curve with $V_{wall} = -1.1V$, $V_{finger} = -1.08V$, at T=30mK, with a vertical offset for clarity. The orange curves (B=0.7T) are shown with (or without) offset on the top (or bottom). (b) is obtained by subtracting the smoothed background from (a). (c) is the in-plane field dependence for $V_{wall} = -0.85V$, $V_{finger} = -1.725V$, while (d) represents the subtracted curves corresponding with (c).

Fig.4.9 shows the in-plane magnetic field dependance of two typical $dI/dV$ traces. Panel (a) and (c) represent the original data (with vertical offset) while panel (b) and (d) correspond with panel (a) and panel (c), respectively, with the smoothed background subtracted. As can be seen, at the low in-plane magnetic field($\sim 0.3T$),

the oscillations are already significantly suppressed. This surprising in-plane magnetic field behavior is systematically characterized and will be discussed in details later.

Fig.4.9(c)(d) represent another set of low magnetic field dependence of one $dI/dV$ traces at a different fixed gate voltage. Nine $dI/dV$ data sets, like the two shown in the figure, are measured for different in-plane magnetic fields. These nine traces were chosen in the following way: for each red curve in Fig.4.1(b), the magnetic field dependance of three $dI/dV$ traces corresponding with three different $V_{finger}$s, were measured. Thus the nine data sets span over a large gate parameter range, and they all show the similar characteristics with Fig.4.9. Thus what we observe here is a general behavior for this sample: the oscillations get suppressed under a small in-plane magnetic field $\sim 0.7T$

The orange curve in Fig.4.9, which passes through the back curve(B=0T), is the same with the other orange curve in (a)(both at B=0.7 T), but with no vertical offset. As can be seen, without the offset, the low field $dI/dV$ curves passes through the oscillations of the B=0 curve. This behavior is also true for all the other $dI/dV$ magnetic field dependence we have measured, and will be discussed later. If we were to assume a typical g-factor of $-0.44$, the Zeeman energy scale would be $51\mu eV/T$. We want to emphasize that the sensitivity to such a small in-plane B field ($\sim 0.3T$) is highly unusual and completely unexpected!

The magnetic field dependence of the nine $dI/dV$ data sets were analyzed to get some statistics. Fig.4.10(a) shows the statistics for these 9 curves, using the same method discussed in Fig.4.8. Taking B=0T, as an example, The average oscillation size for each of the nine curves are represented by the nine red dots on the B=0 line. The black dot represents the mean value of these nine red dots. The fact that the value of some red dots at lower fields is smaller than some red dots at higher fields, does not necessary mean that the oscillation size increases with an increasing

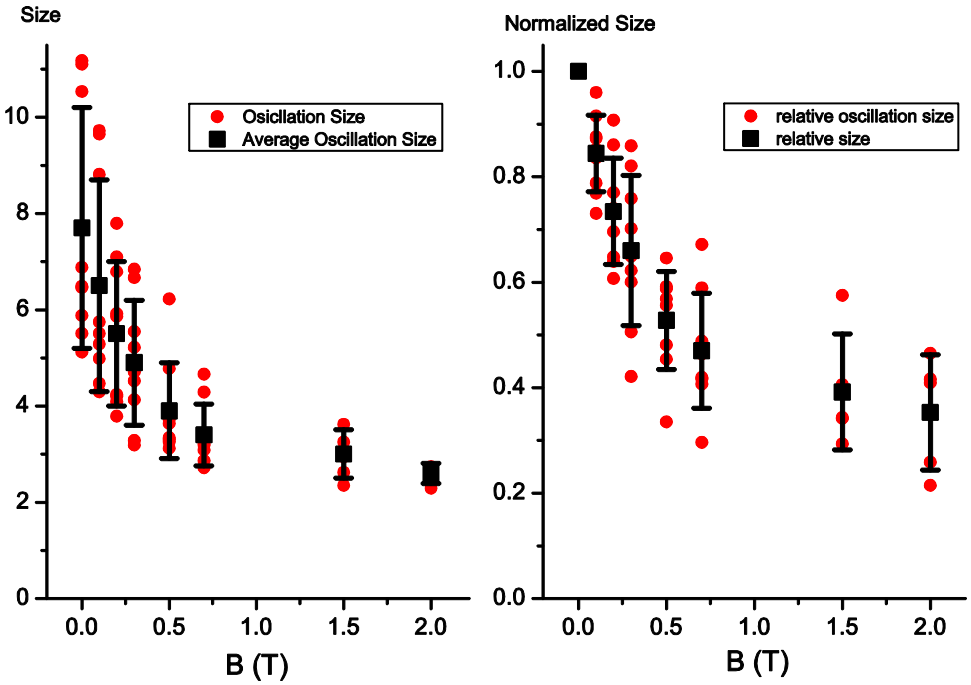


FIGURE 4.10: (a): statistics for the average oscillation amplitude for different gate voltages at different in-plane magnetic fields. (b) the normalized oscillation size

magnetic field. It is just because that these dots have different gate voltages (belong to different curves) and thus have different reference. To normalize the reference, for each $dI/dV$ curve, the oscillation size at B=0 is normalized to 1, and the sizes of the $dI/dV$ traces (with the same gate voltage) at other B fields are all relative to this B=0 size. The normalized relative oscillation size in shown in Fig.4.10(b). The reason that the oscillation amplitude does not decay all the way to 0 is because of the non-zero contributions in the curves which are not related to the small oscillations, in other words, the subtracted curves do not only contain the oscillation information, but also other contributions, e.g. noise.

Fig.4.10 gives a general trend of how the average oscillation size of each curve evolves over an in-plane magnetic field. As can be seen, at $B = 0.7T$ the mean relative oscillation size (red dot) of these nine $dI/dV$ curves, which are chosen over

a relatively wide gate voltage parameter range, is roughly reduced to $36\%(1/e)$ of its size at $B = 0T$.

### *4.2.3 Magnetic Field Dependence: High Field*

Before I discuss the physics behind these $dI/dV$ oscillations, the high in-plane magnetic field dependence of the $dI/dV$ traces will be presented to finish all the experimental characterization. Since the oscillations get 'killed' at low field, in the high field, the physics may be different from the physics related to the small $dI/dV$ oscillations.

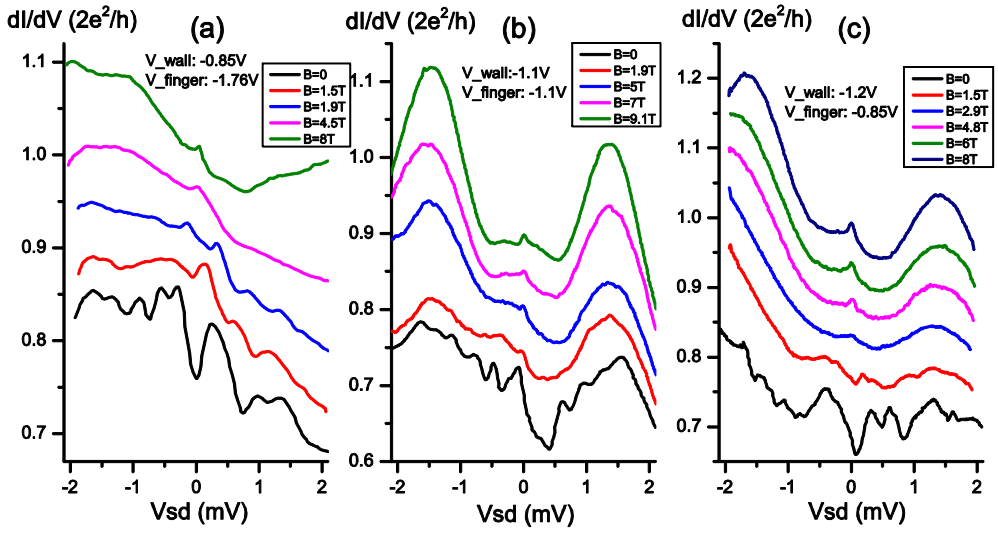


FIGURE 4.11: The high magnetic field dependence for three $dI/dV$ curves at T=30mK. The gate voltages for (a)(b)(c) are labeled in the figure. Vertical offset for clarity.

Fig.4.11 shows the high magnetic field dependence for three $dI/dV$ sets measured at T=30mK. The other six sets show the similar behavior with the three shown in this figure. As can be seen, when the magnetic field is high, strikingly, a very narrow, small and sharp zero-bias-peak starts to show up. Keep in mind that this zero-bias-peak is not present for those curve under zero or low magnetic fields. The behavior of this zero-bias-peak is quite different from the well known zero-bias-

anomaly (ZBA)[19]. In Ref[19], the zero bias peak is wider, bigger and less sharp compare to this one. More importantly, the ZBA is present at B=0, and then split at B=2T[19]. But in our case, the small zero-bias-peak is not present at B=0T. On the contrary, it shows up at high B field and dose not split for B up to 9.1T. It seems that this zero-bias-peak get strengthen (or sharper) when the in-plane B field is increased. This is also different from the ZBA characteristics in Ref[51], where the ZBA is present at B=0. The ZBA in Ref[51] does not split, but becomes weaker and is finally destroyed at B=7T. Besides ZBA, this zero-bias-peak cannot be explained by the Kondo effect either, where the Kondo effects lead to a zero-bias-peak at B=0.

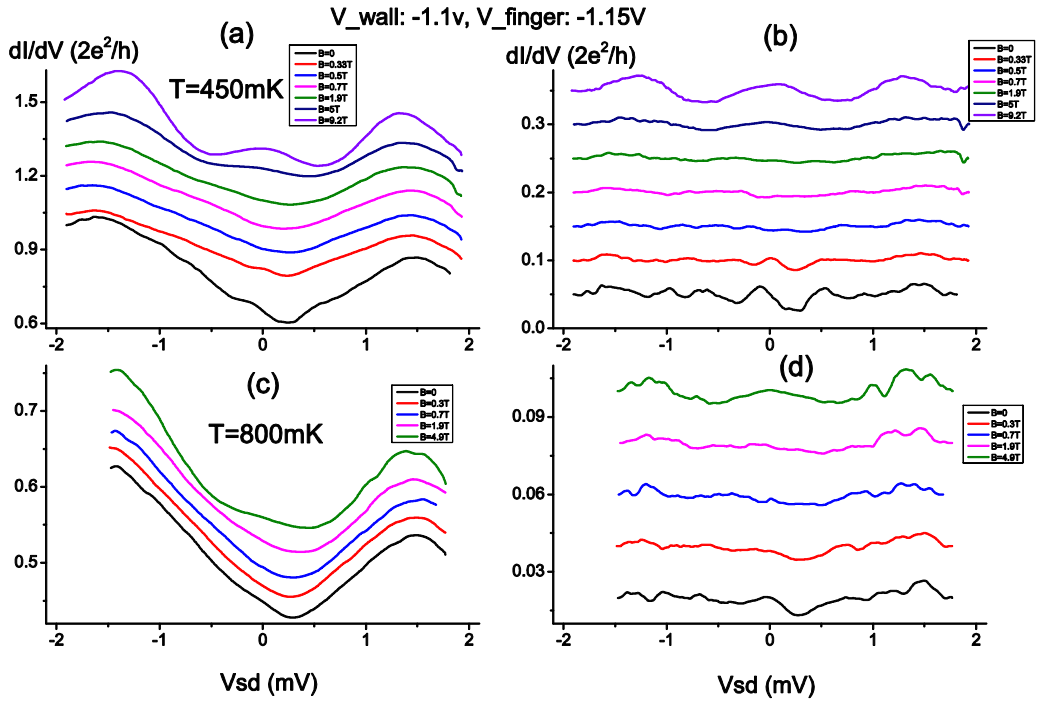


FIGURE 4.12: The high magnetic field dependence for one $dI/dV$ curve, corresponding with Fig.4.11(b), at T=450mK (a) and T=800mK (c), Vertical offset for clarity. $V_wall = -1.1V$, $V_{finger} = -1.15V$. (b) and (d) are obtained from (a) and (c), by subtracting the background respectively.

If the temperature was ramped up to 450mK and 800mK, as shown in Fig.4.12, this narrow zero-bias-peak is gone. This is probably due to the thermal smearing

of the Fermi distribution. The zero-bias-peak width is only $\sim 100\mu eV$ at T=30mK. At T=450mK, the width of the derivative of Fermi function is $3.5k_BT \approx 140\mu eV$, averaging the conductance over this bias range will smooth out the small narrow zero-bias-peak with a peak width $\sim 100\mu eV$.

Panel (b) and (d) in Fig.4.12 are obtained from panel (a) and (c), by subtracting the smoothed background. As can be seen, at B=0T, the small $dI/dV$ oscillations are still observable, then get quickly suppressed at B=0.5T, this behavior is consistent with the magnetic field dependence of the oscillations at T=30mK.

### *4.2.4 Discussion: Are They Within the Single Particle Picture?*

In the above, we have provided a fairly complete characterization of the oscillations. At present, there does not exist any theory, based on which we can interpret the unusual $dI/dV$ oscillations. Below we will analyze several possibilities that may arise within the simple single particle scenario. As will be seen, the size of the oscillations and its magnetic field dependence behavior do not agree with any of these models. Thus by exhausting all these single particle pictures, we believe our observation is related to electron-electron interaction. In the following paragraph, we will first rule out the contribution from the 2DEG reservoir, thus the oscillations are from the QPC channel. Then we will discuss the possible excitations to the quasi-bound states, the modulation of energy bands due to the magnetic field, Aharonov-Bohm effects and weak or anti-weak localizations, individually, with one paragraph for each argument.

First, we can rule out any artifacts from either the indium contacts, or from the 2DEG regions leading into the QPC. Thus, we can ascribe the observed novel behaviors to the 1D QPC channel with full confidence. Let us first examine the issue of contact resistance. Typical good quality indium contacts to the 2DEG is below $1\Omega$ at low temperature. This magnitude is far smaller the observe oscillation amplitude, which is as large as $200\Omega$. Therefore, artifacts from the indium contacts

can be ruled out. As for the 2DEG regions, which behave as excellent metallic conductors, the only possibility for any variation in the resistance (or conductance) in this temperature range ($30mK - 1K$) comes from quantum interference effects, such as Aharonov-Bohm interference, or weak/anti-weak localization. Given the long $l_\phi$, we expect such effects to be of order $G_0 = 2e^2/h$, compared to the 2DEG conductance of $G_{2D} \approx 60G_0$ (equivalent to $\sim 220\Omega$). A change of order $G_0$ will yield a corresponding resistance change of $\sim 6\%$, or $13\Omega$, far below the observed modulation of $200\Omega$. Therefore, the 2DEG regions cannot account for our observations.

One possible origin causing these oscillations may be the excitations to the longitudinal quasi-bound states formed in the channel, associated with the channel length. If this was the case, the effective wave vector and channel length (100nm) for the Nth quasi-bound states should satisfy $k_N \cdot L = N\pi$, similar with the relation of a $Fabry - Pérot$ interferometer. Thus even the smallest energy level spacing, which is between N=1 and N=2, is estimated to be $\Delta E = \Delta\frac{(\hbar k)^2}{2m^*} = 1.7meV$. This energy level spacing is 5 times greater than the spacing between the neighbor oscillations, which is around $330\mu V$ in $V_{sd}$. Besides this level spacing, a small in-plane magnetic field $\sim 0.3T$ is expected to do little to the electron transport in this quasi-bound state excitation picture. But the $dI/dV$ oscillations were significantly modified (suppressed) under such small in-plane magnetic field. These two discrepancies suggest that these oscillations can not be due to the excitations to higher single particle quantum levels.

Now we estimate how the magnetic field modifies the potential profile of the QPC in the 2DEG. The profile is assumed to be a parabola shape: $\frac{1}{2}m\omega^2x^2$ along the direction perpendicular to the channel (out-of-plane). The $\omega$ was estimated to be $3.14 * 10^{12}/s$,[59] using the magnetic depopulation method.[78, 79] Applying a magnetic field perpendicular to the 2DEG will hybridize this parabola with Landau

levels to a new parabola with a new $\omega$. Since the in-plane magnetic field was aligned with the 2DEG within 7°, thus the modification of $\omega$ due to this out-of-plane magnetic field hybridization at $B = 0.3T$ is estimated to be less than $0.2\% \cdot \omega$. Such a small modification of the potential profile has little effect on the electron transport, as the effective $\omega$ increases quadratically with B. Thus this single particle picture can not give rise to the significant modulation of the small oscillations either.

Another way to interpret these oscillations is to relate them with the Aharonov-Bohm effect. But the estimated Aharonov-Bohm phase shift at $B = 0.3T$, due to the out-of-plane magnetic field component, is $\Delta\varphi = \frac{e\Phi_B}{\hbar} \approx 0.05rad$, which is way too small to affect the transport. In this estimation, to calculate $\Phi_B = B_\perp \cdot A$, where A is the effective area of the QPC channel, the channel length is assumed to be the same with the lithographic length, 100nm. And the effective channel width is assumed to be 10% of the estimated channel width, 80nm in the single channel limit,[59] due to the fact that the electron wave function does not sample across the whole channel width in a ballistic devices, in contrast to a diffusive one.[80]

An alternative argument to rule out quantum interference/Aharonov-Bohm type effects, including weak localization and anti-weak localization, is based on the phase coherence length, $l_\phi$. At low temperatures and low energies, $l_\phi$ typically exceeds $20\mu m$ below $50mK$ for high mobility ($\sim 10^6 cm^2/Vs$) devices [81]. The temperature evolution of $l_\phi$ typically obeys power law, behaving as $T^{-\frac{1}{3}}$ or $T^{-\frac{1}{2}}$, depending on whether it is limited by small energy transfer or large energy transfer. Even at $450mK$, $l_\phi$ is expected to exceed $5\mu m$, still far longer than the QPC channel length of $\sim 100nm$. Therefore, there should be little influence on transfer in the linear regime (low energies).Moreover, the $dI/dV$ oscillations occur at a source drain bias voltage of $\sim 330\mu eV$ and higher, far exceeding the thermal energy at $800mK$ and below. Therefore, the relevant $l_\phi$ at such high energies should be completely insensitive to

temperature in the range of our study. Besides this, for weak/anti-weak localization, the conductance is either increased or decreased. But for our case, applying a small in-plane magnetic field results in the dI/dV traces go through the 0 field traces, as shown in Fig.4.9(a), which contradicts the picture of weak/anti-weak localization.

Since an in-plane magnetic field mainly interacts with electron spins, the magnetic field dependence suggests that the small oscillations (and also the linear conductance bump in the inset of Fig.4.2(b)) are related to electron spin correlation. Based on the estimated 1D electron density in the single channel limit,[59] the rough estimation of electron number inside the QPC channel is around $3 \sim 6$ which is on the same order of magnitude comparing with the number of oscillations for a typical $dI/dV$ curve. By speculation, it will be interesting to relate such oscillations to the formation of localized charge state inside the QPC channel due to correlation effects, possible of relevance to the exotic zigzag type of Wigner-crystal-like states. [9]

These considerations give substantial confidence that our findings are associated with electronic and spin correlation effects in the 1D channel.

# 5

# Conclusion

To conclude, we have systematically studied the electron transport property of asymmetric quantum point contacts(QPCs). The linear conductance of these asymmetric QPCs, shows resonances and the modulation of the quantized conductance plateaus. Using symmetric QPCs as a control group, dirt effects can be ruled out for the origins of these two features, with great confidence. Thus these two features are the intrinsic properties of our asymmetric QPCs. As the asymmetric QPC channel length increases, the number of linear conductance resonances also increases. Based on the theoretical calculations performed by other groups[49, 67, 55, 8], we ascribe the resonances and the channel length dependence to be the formation of quasi-bound states, which are further due to the possible formation of the electron-correlation-induced potential barriers in the QPC channel. This potential barrier helps to localize (or quasi-localize) the electrons in the channel.

The differential conductance of the long channel (500 nm or longer) asymmetric QPCs shows zero-bias-anomaly (ZBA). The appearance of these ZBA corresponds with every other linear conductance resonances, obeying the near even-odd law. This near even-odd effect can also be explained within the electron-correlation-induced-

barrier picture, in a manner similar with the even-odd law of the Kondo effect in quantum dots.

The differential conductance of a few long channel asymmetric QPC shows a triple-peak structure near zero bias. Following the near even-odd law, the filling number for this curve is identified to be even, suggesting the forming of a spin triplet state at zero magnetic field. This spin-1 Kondo-like effect suggests the presence of possible ferromagnetic spin interactions.

For a short channel asymmetric QPC, differential conductance shows small oscillations as a function of bias voltage. These small oscillations are significantly suppressed by applying a small in-plane magnetic field ($\sim 0.7T$). The $dI/dV$ oscillations get washed out when the temperature is increased to $\sim 800mK$. Numerical simulations, based on a simple model that the short QPC channel is coupled to the two Fermi leads, is performed to simulate the temperature evolution of these oscillations. The simulation, based on the temperature smearing of the Fermi distribution is able to capture the observed reduction in the amplitude for the unusual oscillations occurring off zero-bias, as the temperature increases. While within the same simulation, the temperature evolution of the structure near zero-bias shows significant discrepancy from the experiment data. This suggests that different physics may be related to the structure near zero-bias and the oscillations off zero-bias. The whole characteristics of these oscillations can not be explained by any simple single particle picture. Therefore, based on the extreme sensitivity of these oscillations to an small in-plane magnetic field, we ascribe the origin of these oscillations to novel electron and spin correlations.

At high in-plane magnetic field, the differential conductance of this short channel QPC shows a small sharp zero-bias peak. This zero-bias peak, which does not show up at zero magnetic field, survives even at B=9T, and gets washed out at $T \sim 450mK$. These characteristics are quite different from the zero-bias-peak in quantum

dots which is related to Kondo effect[1], and also different from the well known Zero-bias-anomaly in QPCs[19]. The linear conductance of this short channel asymmetric QPC shows a bump near $0.7 \times 2e^2/h$. However, this bump gets destroyed in a small in-plane magnetic field ($\sim 0.7T$). This behavior is also quite different from the well known '0.7' effect in QPCs[16].

In this thesis, I have described our findings in ballistic, asymmetric QPCs in the single-channel limit (or in the vicinity limit), which are unique and unobserved in any known semiconductor nanostructure system. These discoveries suggest that unusual spin-related electron correlation effects may be at play. Further in depth investigation will be needed to shed further light on their origins, and answer the question of whether the features we have found are caused by the long-sought-after Wigner crystal-like states. For example, the next step may be adding a top gate to tune the electron density, or trying different crystal. If possible, imaging of the electron charge in QPCs, using scanning gate microscopy[82], may show direct evidence of the Wigner crystal-like states.

# Appendix A

## Quantum Point Contacts on GaAs/AlGaAs Cleaved-Edge-Overgrowth Surface (001)

In this appendix, I will discuss another project, which aimed to study the fractional charge and fractional statistics in the Fractional Quantum Hall regime. The challenging part of this project is the fabrication of QPC samples, which is on the (011) cleaved surface of GaAs/AlGaAs crystal, comparing with the traditional fabrication which is on the (100) surface. I will first introduce the motivation of this project. Then I will describe the fabrication techniques and also some preliminary data: the observation of quantized plateaus of a QPC device, fabricated on the surface of the cleaved edge.

### A.1 Introduction

The Fractional Quantum Hall Effect(FQHE)[2] is an interesting system which shows rich many-body physics[83, 84, 85, 86, 87, 88]. The elementary excitation of the edge state in FQHE is believed to carry a fractional charge[89]. The edge states, due to its chiral Luttinger-liquid nature, shows power-law behavior in terms of edge tunneling

I-V characteristics. The exponent of this power relation is believed to reflect the underlying topological order of the Fractional Quantum Hall fluids. Topological order is a new type of order to identify different phases with no symmetry broken.

In a many-body system, the exchange of two particles usually gives rise to a phase change of the system's wave function, either $\pi$ (Fermi statistics) or 0 (Bose statistics). But in FQHE, the quasi-particles (or the elementary excitations) are described by neither of these two statistics. The statistics that these quasi-particles obey are called fractional statistics, where exchanging two quasi-particles gives rise to a phase change which is a fraction of $\pi$. The fractional charge and statistics can be studied experimentally based on quantum Hall interferometers[90, 91, 92, 93, 94, 95, 96], or on the tunneling current shot noise [97, 98, 99, 100, 101].

These experimental results only partially agree with the theoretical predictions. The reason of this discrepancy is mostly due to the fact that the devices were fabricated on the top of the (100) surface of GaAs/AlGaAs crystal, in a manner similar with the fabrication steps introduced in Chapter 2. The drawback of these devices, for studying the fractional charge and the fractional statistics, is that the potential profile, created by the electrode gates, is smooth due to the long-range Coulomb interaction. Thus under a strong perpendicular magnetic field, the Landau filling factor (or the fractional charge state) varies smoothly near the edge of the potential profile[102, 103]. Therefore, the tunneling is not a process of a single fractional charge tunneling, but a mixture of several different fractional charges (corresponding to different filling factors) tunneling together, which makes it almost impossible to differentiate the contributions from different fractional charges. To study the single fractional charge tunneling process, a sharp potential profile is needed, where the filling factor (fractional charge) will have a sudden change and be well defined.

The cleaved edge overgrowth (CEO) GaAs/AlGaAs hetero-structures[104, 105, 106, 107, 108, 102], show unique properties, in terms of this sharp potential pro-

file. The potential profile in the CEO crystal, defined by the band structure (band engineering), is sharp, comparing with the traditional devices on the (100) surface where the gate defined potential profile is smooth. Therefore, the CEO crystal is a very promising candidate to study the edge tunneling process of the fractional charge/statistics.

## A.2 Device Fabrication on the Cleaved-edge Surface

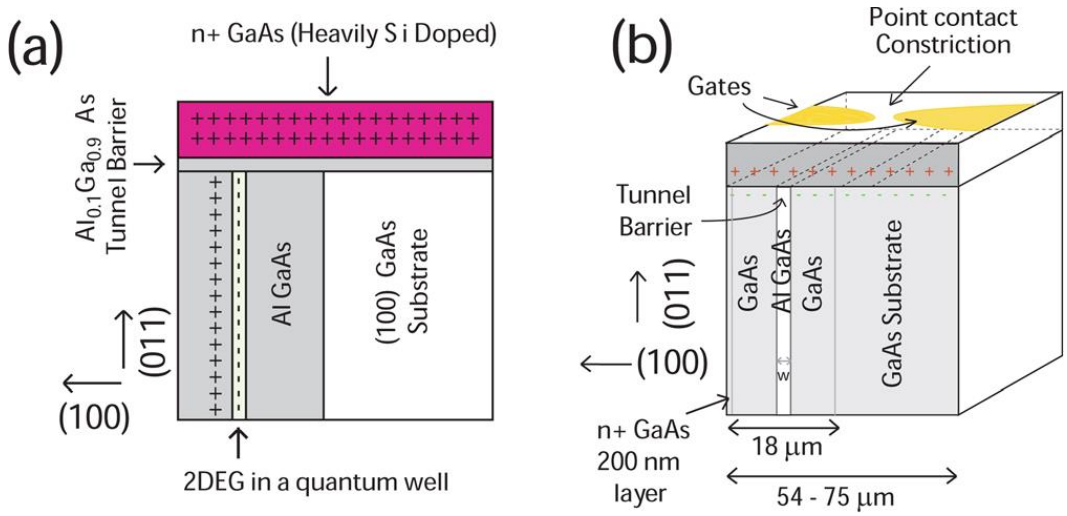


FIGURE A.1: (a) A schematic of the CEO crystal structure used in Ref.[107, 108] for electron tunneling measurement between the highly doped n+ GaAs metal (top side in the figure ) and the 2DEG edge. (b) a schematic of the QPC device fabricated on the CEO surface. This figure is taken from Ref.[109]

Fig.A.1, taken from Ref.[109], shows the schematics of a typical CEO structure and a nano-device on the CEO surface. Panel (a) is the system that Chang *et al* and Hilke *et al* had tried to work on[107, 108]. The drawback of this system is the high doping n+GaAs metal, which causes a sizable increase of the electron density in the edge state of the 2DEG. This increase is undesirable. Therefore in this project, we will try to work on a system similar with the one shown in panel (b), which shows a QPC device fabricated on the CEO surface. The two split gates (yellow), fabricated by the electron beam lithography, define the nanostructure in the 2DEG

underneath, where the potential profile was rendered sharp by the GaAs/AlGaAs band discontinuity in the (100) direction. By lithographically placing a QPC such that the edge of a conducting channel, i.e. the boundary between a conducting and a depletion region, crosses the sharp band discontinuity, one may achieve a truly sharp edge profile.

The CEO crystal was grown by Pfeiffer's group in Princeton, where they first did the initial MBE growth of GaAs/AlGaAs in the (100) direction. Then the crystal was cleaved, and AlGaAs was grown on the cleaved edge, in situ on the (011) plane (Fig.A.1). After the growth, we perform the E-beam lithography to patten gates on this cleaved edge surface. Thus a nano-device, utilizes the sharp band structure of the CEO crystal, can be fabricated.

The difficulty of this fabrication mainly comes from the thickness of the CEO crystal, which is only $\sim 60\mu m$ thick. Such a thin thickness makes the crystal extremely delicate (very easy to be cleaved or damaged). Any routine step from the conventional fabrication, described in Chapter 2, can become difficult. Aside from this fragility, another extremely difficult step is that the gate position is required to be exactly on the quantum well-like sharp potential region, which is $9\mu m$ away from the edge, with a tolerance less than $0.5\mu m$. Otherwise, the sharp potential region will not be in the nano-device region defined by the gates, and the system will not be different from any other conventional system with a smooth potential profile.

### *A.2.1 Nano-device Fabrication Steps on the CEO Surface*

This fabrication procedure was first proposed by Chang[109]. I further developed and optimized some steps, which increases the yield to almost 100%. Below I will show how this challenging fabrication was done, step by step.

The first big step is to clean off the Ga on the backside of the CEO crystal, anneal electric contacts on the (001) surface, and then use stycast to clue the fragile

CEO crystal onto a 600 $\mu m$ thick GaAs substrate. If this can be done successfully, then it will reduce the probability for damaging the crystal significantly in the rest of the fabrication steps, since one can try to avoid touching the CEO crystal by just holding the thick GaAs substrate.

To perform this big step, one needs to follow the following steps:

1. Gently move the CEO crystal around, inside the plastic box to rub off liquid Ga as much as possible. (The liquid Ga is on the backside of the (100) plane, and was used in the initial growth process to glue the crystal to a hold, and to ensure uniformity in the crystal temperature during growth.)

2. Use a filter paper to slide underneath the crystal, and remove it from the box.

3. Melt white wax by putting it on a hot plate at $T \sim 100^oC$. After the melting, quickly glue the CEO crystal upside down on the melted white wax on a glass plate. Then wait for the white wax to be re-solidified. Thus the CEO crystal will be fixed on the glass plate.

4. Use splintered wood stick to remove Ga on the back of the CEO, which is fixed by the white wax. Examine under the Nikon microscope to make sure the highest point of Ga is less than $\sim 20\mu m$ on the backside. (This backside can be bumpy and not flat, if Ga reacts with the crystal during growth.)

5. Dissolve the white wax in acetone for 45 minutes to 1 hour. This will release the CEO, which will be blown dry using an airgun.

6. Use PMMA 495 4% to glue the CEO onto a glass slide right side up, keep the CEO edge over the edge of the glass slide to avoid getting any PMMA on this (110) cleaved surface.

7. Put 2 pure indium dots on the (011) and (100) surfaces, respectively.

8. Anneal at $450 - 500^oC$ for 4 minutes, then test the resistance with a digital voltage meter(DVM).

9. Using PMMA 495 4% to glue a 600 $\mu m$ GaAs substrate $\sim 3.5mmx5mm$ onto a glass slide. Wait it dry, and make sure no PMMA wicking up between the substrate and the alignment slide.

10. Use a tiny amount of stycast to glue the CEO on the GaAs substrate. Avoid stycast from being squeezed onto the (110) edge. Also make sure that the CEO surface is aligned with the substrate. Wait for $\sim$ 24 hours to let it dry. (The drying process can be speed up substantially if one were to heat the sample to $\sim 80^oC$

After finishing the big first step, the second big step is to etch the (100) surface to define electrical contacts on the (100) surface, while the (011) surface needs to be protected during this etching. Then evaporate Cr/Au gate on the (100) surface by covering the annealed electrical contacts with PMMA. The evaporated gate is used later to make a connection with one gate on the CEO surface. This second big step contains the following steps:

1. Glue the substrate vertically onto a sample holder. Use a dropper to drop PMMA onto the CEO edge (with substrate). Wait for it to spread evenly, and check no spill over to (100) side. This PMMA layer is used later to protect all the annealed leads, and sharp corners from the (100) surface over to the (011) surface.

2. Bake at $\sim 160^oC$ on a hot plate for 20 minutes to ensure good adhesion.

3. Put the CEO upside down to perform an inverted etching in the solution with $H_3PO_4 : H_2O_2 : H_2O = 4 : 4 : 32$. The etch rate is nominally $6 - 12nm/min$.

Etch 25 s, 25 s, 5 s, 5 s, (10 s). separately. Test the resistance between the leads with DVM after each etch, with room lights off.

4. Paint PMMA on the (100) surface to cover the leads on this surface. Use $O_2$ plasma to etch for 45 s at a power rate 50- 60 W, and a pressure 100 mtorr, to clean up the residues left during the $H_3PO_4$ etching.

5. Evaporate Cr/Au upside down on the (100) surface and then lift off. Need to cover all unetched portions before evaporation.

The third big step is to perform the electron-beam lithography on CEO surface to pattern nano-device gates. And then bond metal wires from the gates to a 14-pin socket. The steps are listed below:

1. Glue the substrate with CEO vertically on a sample holder.

2. Drop one drop of PMMA on the CEO surface, and then immediately spin it up to let the PMMA get evenly spread over the CEO surface.

3. Due to the thin thickness of the CEO surface($60\mu m$), after spinning, the PMMA thickness on the CEO surface can not be uniform. Count the number of colorful fringes, due to the room light interference, to tell the thickness difference between the edge and the gate position on the surface. If the difference is more than 5 fringes, it is impossible to perform an e-beam lithography. Then the PMMA needs to be dissolved, and repeat this step.

4. Based on the PMMA thickness difference, calculate to assign the right dosage of the electron beam for each part of the gate pattern.

5. Use SEM to locate the right position of the CEO surface, under the lowest beam current($\sim 2pA$). Perform the e-beam writing.

6. Develop, etch with $O_2$ plasma, evaporate Cr/Au, and lift off.

7. Use a tiny bit of indium to bridge the gap between the gate on the GaAs substrate and the gate on the CEO surface.

8. Use gold wires and indium to connect the gates to a 14-pin dig plug.

If all these steps work, then the fabrication is done. The sample can first be cooled down in liquid $N_2$ to do a preliminary check, and then cooled down at 4.2K, 0.3K and even 0.03K to perform a measurement.

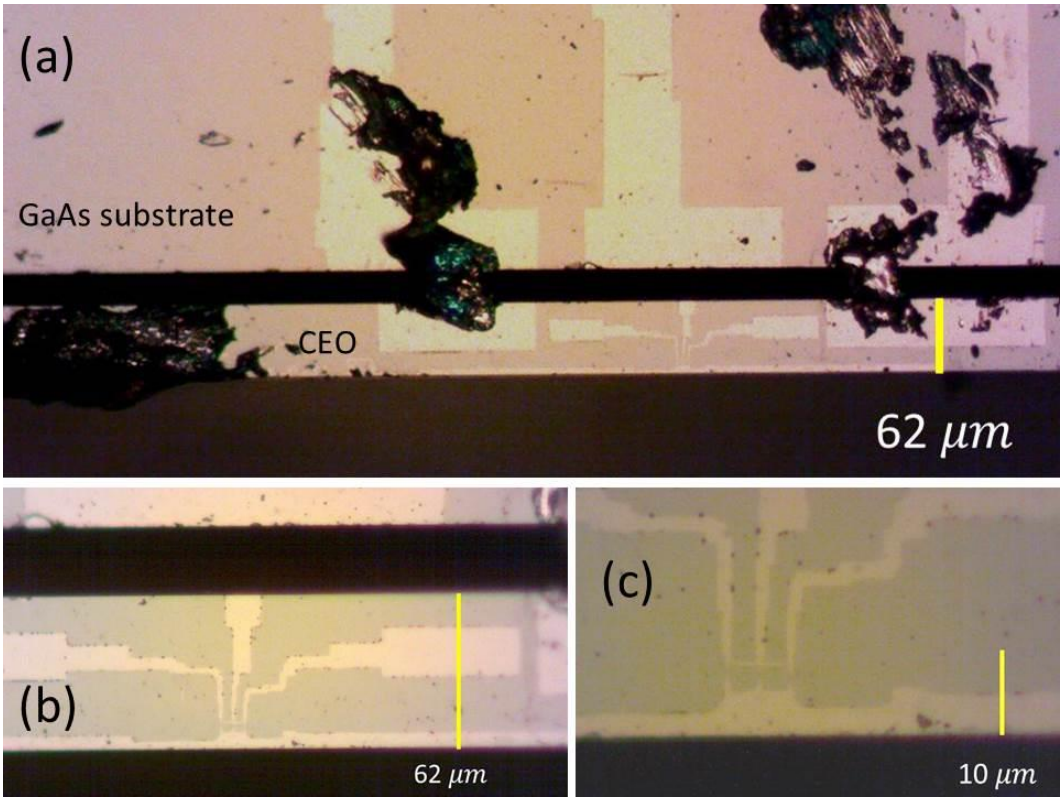


FIGURE A.2: Optical Image of a Quantum Nano-structure Device on the CEO Surface. The yellow bar labels the length scale.

Fig.A.2 is the optical microscope image of one device fabricated on the CEO surface. The CEO part and the GaAs substrate part are labeled in panel (a). The

yellow shiny region is Cr/Au gate. Panel (b) is the enlarged image of part of panel (a), while panel (c) is the enlarged image of part of panel (b).

## A.3 Observation of the Quantized Conductance Plateau in CEO

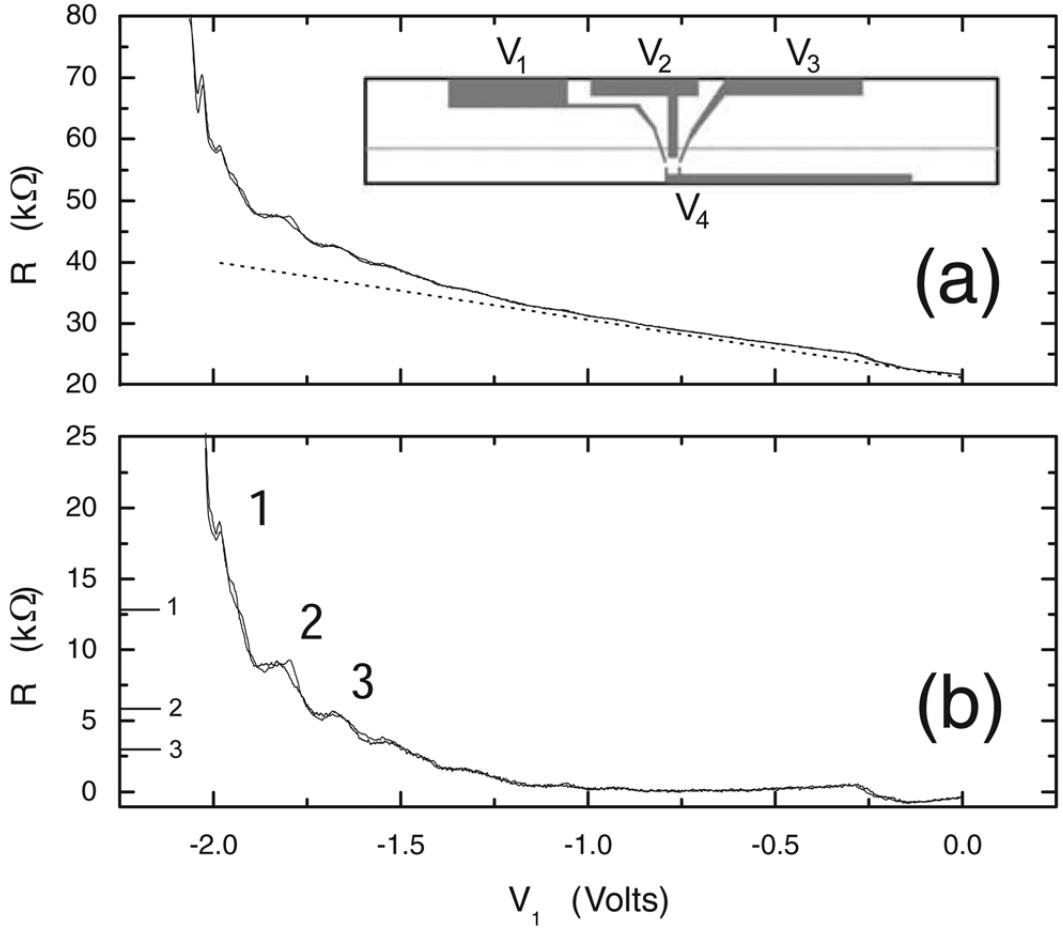


FIGURE A.3: (a) The linear conductance of this QPC as a function of $V_1$. (b) is obtained after subtracting a linear background from (a), suggesting the quantized resistance. The plateau indexes are labeled to compare with the accurate value $h/(N \times 2e^2)$. Inset in (a) shows the schematic of the gate geometry of this device. This figure is taken from Ref.[109].

I have fabricated $\sim 10$ devices successfully, on the CEO crystal surface. But the conductance turns out to be poor, which is way below what was expected. This is probably because that during the MBE growth, somehow some defects were in-

troduced. When the samples were cooled down, those defects trapped most of the carriers. For the best sample, the carrier density is measured to be $0.6 \times 10^{11}/cm^2$, and the mobility is estimated to be between 90k and 370k $cm^2/Vs$. Despite all these non-idealities, the quantized conductance (or resistance) of QPCs fabricated on the CEO surface can still be observed, as shown in Fig.A.3. This figure is taken from Ref[109]. Panel (a) shows the raw resistance data, while panel (b) shows the resistance of the QPC as a function of $V_1$ gate (depicted in the inset), after subtracting a linear background, which is labeled by the dashed line in panel (a). This linear background comes from the 2DEG. As can be seen in panel (b), quantized resistance plateaus are well established, which come within $\sim 40\%$ of the correct values labeled on the y axis.

Now we have succeeded in demonstrating the feasibility of fabricating sub-micron devices on the cleaved-edge, further progress will depend crucially on Professor Loren Pfeiffer's growth of better quality crystals. We are eager to move this project forward in the near future.

# Bibliography


[1] D. Goldhaber-Gordon, H. Shtrikman, D. Mahalu, D. Abusch-Magder, U. Meirav, and M. A. Kastner. Kondo effect in a single-electron transistor. *Nature*, 391:156, Jan 1998.

[2] D. C. Tsui, H. L. Stormer, and A. C. Gossard. Two-dimensional magnetotransport in the extreme quantum limit. *Phys. Rev. Lett.*, 48:1559–1562, May 1982.

[3] E. Wigner. On the interaction of electrons in metals. *Phys. Rev.*, 46:1002–1011, Dec 1934.

[4] H. J. Schulz. Wigner crystal in one dimension. *Phys. Rev. Lett.*, 71:1864–1867, Sep 1993.

[5] Julia S Meyer and K A Matveev. Wigner crystal physics in quantum wires. *Journal of Physics: Condensed Matter*, 21(2):023203, 2009.

[6] Boris Spivak and Fei Zhou. Ferromagnetic correlations in quasi-one-dimensional conducting channels. *Phys. Rev. B*, 61:16730–16735, Jun 2000.

[7] K. A. Matveev. Conductance of a quantum wire at low electron density. *Phys. Rev. B*, 70:245319, Dec 2004.

[8] A. D. Güçlü, C. J. Umrigar, Hong Jiang, and Harold U. Baranger. Localization in an inhomogeneous quantum wire. *Phys. Rev. B*, 80:201302, Nov 2009.

[9] Abhijit C. Mehta, C. J. Umrigar, Julia S. Meyer, and Harold U. Baranger. Zigzag phase transition in quantum wires. *Phys. Rev. Lett.*, 110:246802, Jun 2013.

[10] Elliott Lieb and Daniel Mattis. Theory of ferromagnetism and the ordering of electronic energy levels. *Phys. Rev.*, 125:164–172, Jan 1962.

[11] John H. Davies. *The Physics of Low-dimensional Semiconductors: An Introduction*. Cambridge University Press, 1997.

[12] B. J. van Wees, H. van Houten, C. W. J. Beenakker, J. G. Williamson, L. P. Kouwenhoven, D. van der Marel, and C. T. Foxon. Quantized conductance of point contacts in a two-dimensional electron gas. *Phys. Rev. Lett.*, 60:848–850, Feb 1988.

[13] D A Wharam, T J Thornton, R Newbury, M Pepper, H Ahmed, J E F Frost, D G Hasko, D C Peacock, D A Ritchie, and G A C Jones. One-dimensional transport and the quantisation of the ballistic resistance. *Journal of Physics C: Solid State Physics*, 21(8):L209, 1988.

[14] John A. Nixon, John H. Davies, and Harold U. Baranger. Breakdown of quantized conductance in point contacts calculated using realistic potentials. *Phys. Rev. B*, 43:12638–12641, May 1991.

[15] A P Micolich. What lurks below the last plateau: experimental studies of the 0.7 2 e 2 / h conductance anomaly in one-dimensional systems. *Journal of Physics: Condensed Matter*, 23(44):443201, 2011.

[16] K. J. Thomas, J. T. Nicholls, M. Y. Simmons, M. Pepper, D. R. Mace, and D. A. Ritchie. Possible spin polarization in a one-dimensional electron gas. *Phys. Rev. Lett.*, 77:135–138, Jul 1996.

[17] K. v. Klitzing, G. Dorda, and M. Pepper. New method for high-accuracy determination of the fine-structure constant based on quantized hall resistance. *Phys. Rev. Lett.*, 45:494–497, Aug 1980.

[18] Georg Seelig and K. A. Matveev. Electron-phonon scattering in quantum point contacts. *Phys. Rev. Lett.*, 90:176804, May 2003.

[19] S. M. Cronenwett, H. J. Lynch, D. Goldhaber-Gordon, L. P. Kouwenhoven, C. M. Marcus, K. Hirose, N. S. Wingreen, and V. Umansky. Low-temperature fate of the 0.7 structure in a point contact: A kondo-like correlated state in an open system. *Phys. Rev. Lett.*, 88:226805, May 2002.

[20] L Kouwenhoven and L Glazman. Revival of the kondo effect. *Physics World*, page 33, Jan 2001.

[21] A M Chang and J C Chen. The kondo effect in coupled-quantum dots. *Reports on Progress in Physics*, 72(9):096501, 2009.

[22] F. Sfigakis, K. Das Gupta, S. Sarkozy, I. Farrer, D.A. Ritchie, M. Pepper, and G.A.C. Jones. Benefits of using undoped gaas/algaas heterostructures: A case study of the zero-bias bias anomaly in quantum wires. *Physica E: Low-dimensional Systems and Nanostructures*, 42(4):1200 – 1204, 2010. 18th International Conference on Electron Properties of Two-Dimensional Systems.

[23] O. Klochan, A. P. Micolich, A. R. Hamilton, K. Trunov, D. Reuter, and A. D. Wieck. Observation of the kondo effect in a spin-3/2 hole quantum dot. *Phys. Rev. Lett.*, 107:076805, Aug 2011.

[24] S. Sarkozy, F. Sfigakis, K. Das Gupta, I. Farrer, D. A. Ritchie, G. A. C. Jones, and M. Pepper. Zero-bias anomaly in quantum wires. *Phys. Rev. B*, 79:161307, Apr 2009.

[25] Y. Ren, W. W. Yu, S. M. Frolov, J. A. Folk, and W. Wegscheider. Zero-bias anomaly of quantum point contacts in the low-conductance limit. *Phys. Rev. B*, 82:045313, Jul 2010.

[26] K. M. Liu, V. Umansky, and S. Y. Hsu. Effect of scattering on zero-bias anomaly and conductance reduction in quasi-one-dimensional quantum wires. *Phys. Rev. B*, 81:235316, Jun 2010.

[27] T.-M. Chen, A. C. Graham, M. Pepper, I. Farrer, and D. A. Ritchie. Non-kondo zero-bias anomaly in quantum wires. *Phys. Rev. B*, 79:153303, Apr 2009.

[28] F. Sfigakis, C. J. B. Ford, M. Pepper, M. Kataoka, D. A. Ritchie, and M. Y. Simmons. Kondo effect from a tunable bound state within a quantum wire. *Phys. Rev. Lett.*, 100:026807, Jan 2008.

[29] P. E. Lindelof. Effect on conductance of an isomer state in a quantum point contact. *Proc. SPIE*, 4415:77–85, 2001.

[30] Yigal Meir, Kenji Hirose, and Ned S. Wingreen. Kondo model for the 0.7 anomaly in transport through a quantum point contact. *Phys. Rev. Lett.*, 89:196802, Oct 2002.

[31] T. Rejec and Y. Meir. Magnetic impurity formation in quantum point contacts. *Nature*, 442:900, Aug 2006.

[32] A. Kristensen, H. Bruus, A. E. Hansen, J. B. Jensen, P. E. Lindelof, C. J. Marckmann, J. Nygård, C. B. Sørensen, F. Beuscher, A. Forchel, and M. Michel. Bias and temperature dependence of the 0.7 conductance anomaly in quantum point contacts. *Phys. Rev. B*, 62:10950–10957, Oct 2000.

[33] Henrik Bruus, Vadim V Cheianov, and Karsten Flensberg. The anomalous 0.5 and 0.7 conductance plateaus in quantum point contacts. *Physica E: Low-dimensional Systems and Nanostructures*, 10(13):97 – 102, 2001. Proceedings of the First International Conference on the Physics and Applications of Spin-Related Phenomena in Semiconductors.

[34] D. J. Reilly, T. M. Buehler, J. L. O'Brien, A. R. Hamilton, A. S. Dzurak, R. G. Clark, B. E. Kane, L. N. Pfeiffer, and K. W. West. Density-dependent spin

polarization in ultra-low-disorder quantum wires. *Phys. Rev. Lett.*, 89:246801, Nov 2002.

[35] D. J. Reilly. Phenomenological model for the 0.7 conductance feature in quantum wires. *Phys. Rev. B*, 72:033309, Jul 2005.

[36] Andreas Lassl, Peter Schlagheck, and Klaus Richter. Effects of short-range interactions on transport through quantum point contacts: A numerical approach. *Phys. Rev. B*, 75:045346, Jan 2007.

[37] V. V. Flambaum and M. Yu. Kuchiev. Possible mechanism of the fractional-conductance quantization in a one-dimensional constriction. *Phys. Rev. B*, 61:R7869–R7872, Mar 2000.

[38] T. Rejec, A. Ramšak, and J. H. Jefferson. Spin-dependent resonances in the conduction edge of quantum wires. *Phys. Rev. B*, 62:12985–12989, Nov 2000.

[39] O. P. Sushkov. Conductance anomalies in a one-dimensional quantum contact. *Phys. Rev. B*, 64:155319, Sep 2001.

[40] A. D. Klironomos, J. S. Meyer, and K. A. Matveev. Spontaneous spin polarization in quantum wires. *EPL (Europhysics Letters)*, 74(4):679, 2006.

[41] A. D. Klironomos, J. S. Meyer, T. Hikihara, and K. A. Matveev. Spin coupling in zigzag wigner crystals. *Phys. Rev. B*, 76:075302, Aug 2007.

[42] K. A. Matveev. Conductance of a quantum wire in the wigner-crystal regime. *Phys. Rev. Lett.*, 92:106801, Mar 2004.

[43] Phillip M. Wu, Peng Li, Hao Zhang, and A. M. Chang. Evidence for the formation of quasibound states in an asymmetrical quantum point contact. *Phys. Rev. B*, 85:085305, Feb 2012.

[44] Hao Zhang, Phillip M. Wu, and Albert M. Chang. Quasibound states and evidence for a spin-1 kondo effect in asymmetric quantum point contacts. *Phys. Rev. B*, 88:075311, Aug 2013.

[45] Frank Pobell. *Matter and Methods at Low Temperatures*. Springer, 2007.

[46] Guy K. White and Philip Meeson. *Experimental Techniques in Low-Temperature Physics*. Oxford University Press, 2002.

[47] J. W. Ekin. *Experimental techniques for low-temperature measurements : cryostat design, material properties, and superconductor critical-current testing*. Oxford University Press, 2006.

[48] E. Welander, I. I. Yakimenko, and K.-F. Berggren. Localization of electrons and formation of two-dimensional wigner spin lattices in a special cylindrical semiconductor stripe. *Phys. Rev. B*, 82:073307, Aug 2010.

[49] I I Yakimenko, V S Tsykunov, and K-F Berggren. Bound states, electron localization and spin correlations in low-dimensional gaas/algaas quantum constrictions. *Journal of Physics: Condensed Matter*, 25(7):072201, 2013.

[50] W. K. Hew, K. J. Thomas, M. Pepper, I. Farrer, D. Anderson, G. A. C. Jones, and D. A. Ritchie. Incipient formation of an electron lattice in a weakly confined quantum wire. *Phys. Rev. Lett.*, 102:056804, Feb 2009.

[51] W. K. Hew, K. J. Thomas, M. Pepper, I. Farrer, D. Anderson, G. A. C. Jones, and D. A. Ritchie. Spin-incoherent transport in quantum wires. *Phys. Rev. Lett.*, 101:036801, Jul 2008.

[52] W.K. Hew, K.J. Thomas, M. Pepper, I. Farrer, D. Anderson, G.A.C. Jones, and D.A. Ritchie. Double-row transport in quantum wires of shallow confinement. *Physica E: Low-dimensional Systems and Nanostructures*, 42(4):1118 – 1121, 2010. 18th International Conference on Electron Properties of Two-Dimensional Systems.

[53] L. W. Smith, W. K. Hew, K. J. Thomas, M. Pepper, I. Farrer, D. Anderson, G. A. C. Jones, and D. A. Ritchie. Row coupling in an interacting quasi-one-dimensional quantum wire investigated using transport measurements. *Phys. Rev. B*, 80:041306, Jul 2009.

[54] L.W. Smith, W.K. Hew, K.J. Thomas, M. Pepper, I. Farrer, D. Anderson, G.A.C. Jones, and D.A. Ritchie. Coupled double-row formation in a quasi-1d wire. *Physica E: Low-dimensional Systems and Nanostructures*, 42(4):1114 – 1117, 2010. 18th International Conference on Electron Properties of Two-Dimensional Systems.

[55] Taegeun Song and Kang-Hun Ahn. Ferromagnetically coupled magnetic impurities in a quantum point contact. *Phys. Rev. Lett.*, 106:057203, Feb 2011.

[56] C. C. Grimes and G. Adams. Evidence for a liquid-to-crystal phase transition in a classical, two-dimensional sheet of electrons. *Phys. Rev. Lett.*, 42:795–798, Mar 1979.

[57] N. D. Mermin and H. Wagner. Absence of ferromagnetism or antiferromagnetism in one- or two-dimensional isotropic heisenberg models. *Phys. Rev. Lett.*, 17:1133–1136, Nov 1966.

[58] P. C. Hohenberg. Existence of long-range order in one and two dimensions. *Phys. Rev.*, 158:383–386, Jun 1967.

[59] Phillip M. Wu. Electron correlations and spin in asymmetric gaas quantum point contacts and signatures of structural transitions in hall effect of fese. 2010.

[60] P.L. McEuen, B.W. Alphenaar, R.G. Wheeler, and R.N. Sacks. Resonant transport effects due to an impurity in a narrow constriction. *Surface Science*, 229(13):312 – 315, 1990.

[61] Charles Kittel. *Introduction to Solid State Physics*. Wiley, 2004.

[62] Neil W. Ashcroft and N. David Mermin. *Solid State Physics*. Thomson Learning, 1976.

[63] George Kirczenow. Resonant conduction in ballistic quantum channels. *Phys. Rev. B*, 39:10452–10455, May 1989.

[64] D. van der Marel and E. G. Haanappel. Model calculations of the quantum ballistic transport in two-dimensional constriction-type microstructures. *Phys. Rev. B*, 39:7811–7820, Apr 1989.

[65] Aaron Szafer and A. Douglas Stone. Theory of quantum conduction through a constriction. *Phys. Rev. Lett.*, 62:300–303, Jan 1989.

[66] M. Buttiker. Quantized transmission of a saddle-point constriction. *Phys. Rev. B*, 41:7906–7909, Apr 1990.

[67] R. Akis and D.K. Ferry. Spin density functional theory simulations of quantum point contacts: An investigation of spin filtering effects. *Technical Proceedings of the 2005 NSTI Nanotechnology Conference and Trade Show*, 3(4):240, 2005.

[68] V Senz, T Heinzel, T Ihn, S Lindemann, R Held, K Ensslin, W Wegscheider, and M Bichler. Analysis of the temperature-dependent quantum point contact conductance in relation to the metal-insulator transition in two dimensions. *Journal of Physics: Condensed Matter*, 13(17):3831, 2001.

[69] Leo Kouwenhoven and Charles Marcus. Quantum dots. *Physics World*, 11:35, Jun 1998.

[70] M.A. Kastner and D. Goldhaber-Gordon. Kondo physics with single electron transistors. *Solid State Communications*, 119(45):245 – 252, 2001.

[71] Jun Kondo. Resistance minimum in dilute magnetic alloys. *Progress of Theoretical Physics*, 32(37):12, 1964.

[72] P. W. Anderson. Localized magnetic states in metals. *Phys. Rev.*, 124:41–53, Oct 1961.

[73] M. A. Reed, J. N. Randall, R. J. Aggarwal, R. J. Matyi, T. M. Moore, and A. E. Wetsel. Observation of discrete electronic states in a zero-dimensional semiconductor nanostructure. *Phys. Rev. Lett.*, 60:535–537, Feb 1988.

[74] A. Kogan, G. Granger, M. A. Kastner, D. Goldhaber-Gordon, and Hadas Shtrikman. Singlettriplet transition in a single-electron transistor at zero magnetic field. *Phys. Rev. B*, 67:113309, Mar 2003.

[75] C. H. L. Quay, John Cumings, S. J. Gamble, R. de Picciotto, H. Kataura, and D. Goldhaber-Gordon. Magnetic field dependence of the spin-1/2 and spin-1 kondo effects in a quantum dot. *Phys. Rev. B*, 76:245311, Dec 2007.

[76] Nicolas Roch, Serge Florens, Vincent Bouchiat, Wolfgang Wernsdorfer, and Franck Balestro. Quantum phase transition in a single-molecule quantum dot. *Nature*, 453:633, May 2008.

[77] M. J. Iqbal, Roi Levy, E. J. Koop, J. B. Dekker, J. P. de Jong, J. H. M. van der Velde, D. Reuter, A. D. Wieck, Ramon Aguado, Yigal Meir, and C. H. van der Wal. Odd and even kondo effects from emergent localization in quantum point contacts. *Nature*, 501:79, Aug 2013.

[78] B. J. van Wees, L. P. Kouwenhoven, H. van Houten, C. W. J. Beenakker, J. E. Mooij, C. T. Foxon, and J. J. Harris. Quantized conductance of magnetoelectric subbands in ballistic point contacts. *Phys. Rev. B*, 38:3625–3627, Aug 1988.

[79] K. F. Berggren, T. J. Thornton, D. J. Newson, and M. Pepper. Magnetic depopulation of 1d subbands in a narrow 2d electron gas in a gaas:algaas heterojunction. *Phys. Rev. Lett.*, 57:1769–1772, Oct 1986.

[80] G. Timp, A. M. Chang, J. E. Cunningham, T. Y. Chang, P. Mankiewich, R. Behringer, and R. E. Howard. Observation of the aharonov-bohm effect for wt¿1. *Phys. Rev. Lett.*, 58:2814–2817, Jun 1987.

[81] A. M. Chang, H. U. Baranger, L. N. Pfeiffer, and K. W. West. Weak localization in chaotic versus nonchaotic cavities: A striking difference in the line shape. *Phys. Rev. Lett.*, 73:2111–2114, Oct 1994.

[82] M. A. Topinka, B. J. LeRoy, S. E. J. Shaw, E. J. Heller, R. M. Westervelt, K. D. Maranowski, and A. C. Gossard. Imaging coherent electron flow from a quantum point contact. *Science*, 289(5488):2323–2326, 2000.

[83] XIAO-GANG WEN. Theory of the edge states in fractional quantum hall effects. *International Journal of Modern Physics B*, 06(10):1711–1762, 1992.

[84] Xiao-Gang Wen. Topological orders and edge excitations in fractional quantum hall states. *Advances in Physics*, 44(5):405–473, 1995.

[85] C. L. Kane and Matthew P. A. Fisher. Resonant tunneling in an interacting one-dimensional electron gas. *Phys. Rev. B*, 46:7268–7271, Sep 1992.

[86] C. L. Kane, Matthew P. A. Fisher, and J. Polchinski. Randomness at the edge: Theory of quantum hall transport at filling =2/3. *Phys. Rev. Lett.*, 72:4129–4132, Jun 1994.

[87] C. L. Kane and Matthew P. A. Fisher. Impurity scattering and transport of fractional quantum hall edge states. *Phys. Rev. B*, 51:13449–13466, May 1995.

[88] P. Fendley, A. W. W. Ludwig, and H. Saleur. Exact nonequilibrium transport through point contacts in quantum wires and fractional quantum hall devices. *Phys. Rev. B*, 52:8934–8950, Sep 1995.

[89] R. B. Laughlin. Anomalous quantum hall effect: An incompressible quantum fluid with fractionally charged excitations. *Phys. Rev. Lett.*, 50:1395–1398, May 1983.

[90] Parsa Bonderson, Alexei Kitaev, and Kirill Shtengel. Detecting non-abelian statistics in the nu=5/2 fractional quantum hall state. *Phys. Rev. Lett.*, 96:016803, Jan 2006.

[91] Ady Stern and Bertrand I. Halperin. Proposed experiments to probe the non-abelian nu=5/2 quantum hall state. *Phys. Rev. Lett.*, 96:016802, Jan 2006.

[92] B. Rosenow and B. I. Halperin. Influence of interactions on flux and back-gate period of quantum hall interferometers. *Phys. Rev. Lett.*, 98:106801, Mar 2007.

[93] V. J. Goldman and B. Su. Resonant tunneling in the quantum hall regime: Measurement of fractional charge. *Science*, 267(5200):1010–1012, 1995.

[94] F. E. Camino, Wei Zhou, and V. J. Goldman. Realization of a laughlin quasiparticle interferometer: Observation of fractional statistics. *Phys. Rev. B*, 72:075342, Aug 2005.

[95] Iuliana P. Radu, J. B. Miller, C. M. Marcus, M. A. Kastner, L. N. Pfeiffer, and K. W. West. Quasi-particle properties from tunneling in the v = 5/2 fractional quantum hall state. *Science*, 320(5878):899–902, 2008.

[96] R. L. Willett, L. N. Pfeiffer, and K. W. West. Measurement of filling factor 5/2 quasiparticle interference with observation of charge e/4 and e/2 period oscillations. *Proceedings of the National Academy of Sciences*, 106(22):8853–8858, 2009.

[97] C. L. Kane and Matthew P. A. Fisher. Nonequilibrium noise and fractional charge in the quantum hall effect. *Phys. Rev. Lett.*, 72:724–727, Jan 1994.

[98] C. de C. Chamon, D. E. Freed, and X. G. Wen. Tunneling and quantum noise in one-dimensional luttinger liquids. *Phys. Rev. B*, 51:2363–2379, Jan 1995.

[99] P. Fendley, A. W. W. Ludwig, and H. Saleur. Exact nonequilibrium dc shot noise in luttinger liquids and fractional quantum hall devices. *Phys. Rev. Lett.*, 75:2196–2199, Sep 1995.

[100] R. de Picciotto1, M. Reznikov1, M. Heiblum1, V. Umansky, G. Bunin1, and D. Mahalu. Direct observation of a fractional charge. *Nature*, 389:162–164, Sep 1997.

[101] L. Saminadayar, D. C. Glattli, Y. Jin, and B. Etienne. Observation of the e/3 fractionally charged laughlin quasiparticle. *Phys. Rev. Lett.*, 79:2526–2529, Sep 1997.

[102] A. M. Chang. Chiral luttinger liquids at the fractional quantum hall edge. *Rev. Mod. Phys.*, 75:1449–1505, Nov 2003.

[103] C. de C. Chamon and X. G. Wen. Sharp and smooth boundaries of quantum hall liquids. *Phys. Rev. B*, 49:8227–8241, Mar 1994.

[104] Loren Pfeiffer, K. W. West, H. L. Stormer, J. P. Eisenstein, K. W. Baldwin, D. Gershoni, and J. Spector. Formation of a high quality twodimensional electron gas on cleaved gaas. *Applied Physics Letters*, 56(17):1697–1699, 1990.

[105] A. Yacoby, H. L. Stormer, Ned S. Wingreen, L. N. Pfeiffer, K. W. Baldwin, and K. W. West. Nonuniversal conductance quantization in quantum wires. *Phys. Rev. Lett.*, 77:4612–4615, Nov 1996.

[106] W. Wegscheider, G. Schedelbeck, G. Abstreiter, M. Rother, and M. Bichler. Atomically precise gaas/algaas quantum dots fabricated by twofold cleaved edge overgrowth. *Phys. Rev. Lett.*, 79:1917–1920, Sep 1997.

[107] A. M. Chang, L. N. Pfeiffer, and K. W. West. Observation of chiral luttinger behavior in electron tunneling into fractional quantum hall edges. *Phys. Rev. Lett.*, 77:2538–2541, Sep 1996.

[108] M. Hilke, D. C. Tsui, M. Grayson, L. N. Pfeiffer, and K. W. West. Fermi liquid to luttinger liquid transition at the edge of a two-dimensional electron gas. *Phys. Rev. Lett.*, 87:186806, Oct 2001.

[109] A. M. Chang, Hao Zhang, L. N. Pfeiffer, and K. W. West. Fabrication of submicron devices on the (011) cleave surface of a cleaved-edge-overgrowth gaas/algaas crystal. *Applied Physics Letters*, 100(12):–, 2012.

# Biography

## Hao Zhang

### Personal

- Born on June 20th, 1987 in Handan, Hebei, China

### Education

- Aug. 2010 $\sim$ May 2014: PhD in Physics, Duke University, Durham, NC, U.S.
- Aug. 2010 $\sim$ May 2014: Master of Science in Electrical and Computer Engineer, Duke University, Durham, NC, U.S.
- Sept. 2006 $\sim$ Jul. 2010: B.S. in Physics, Peking (Beijing) University, Beijing, China
- Sept. 2006 $\sim$ Jul. 2010: Economics Minor, Peking (Beijing) University, Beijing, China

### Publications

- Hao Zhang, Phillip Wu and Albert Chang, "*Quasibound States and Evidence for a Spin 1 Kondo Effect in Asymmetric Quantum Point Contacts*", **Phys. Rev. B** 88, 075311 (2013).
- Albert Chang, Hao Zhang, Loren Pfeiffer and K. W. West, "*Fabrication of submicron devices on the (011) cleave surface of a cleaved-edge-overgrowth GaAs/AlGaAs crystal*", **App. Phys. Lett.** 100, 123106(2012).

- Phillip Wu, Peng Li, Hao Zhang and Albert Chang, "*Evidence for the formation of quasibound states in an asymmetric quantum point contact*", **Phys. Rev. B** 85, 085305(2012).

## Papers in Preparation

- Hao Zhang, Phillip Wu and Albert Chang, "Novel non-linear conductance oscillations in asymmetric quantum point contacts", (2014).